INVESTIGATION OF THE FRICTION FACTOR BEHAVIOR FOR FLAT PLATE TESTS OF SMOOTH AND ROUGHENED SURFACES WITH SUPPLY PRESSURES UP TO 84 BARS

A Thesis

by

BASSEM ALI KHEIREDDIN

Submitted to the Office of Graduate Studies of
Texas A&M University
in partial fulfillment of the requirements for the degree of

MASTER OF SCIENCE

August 2009

Major Subject: Mechanical Engineering

INVESTIGATION OF THE FRICTION FACTOR BEHAVIOR FOR FLAT PLATE TESTS OF SMOOTH AND ROUGHENED SURFACES WITH SUPPLY PRESSURES UP TO 84 BARS

A Thesis

by

BASSEM ALI KHEIREDDIN

Submitted to the Office of Graduate Studies of
Texas A&M University
in partial fulfillment of the requirements for the degree of

MASTER OF SCIENCE

Approved by:

Chair of Committee, Dara Childs
Committee Members, Gerald Morrison
Hamn-Ching Chen
Head of Department, Dennis O'Neal

August 2009

Major Subject: Mechanical Engineering

ABSTRACT

Investigation of the Friction Factor Behavior for Flat Plate Tests of Smooth and Roughened Surfaces With Supply Pressures up to 84 Bars. (August 2009)

Bassem Ali Kheireddin, B.S., University of Texas-Pan American

Chair of Advisory Committee: Dr. Dara Childs

Annular gas seal clearances were simulated with closely spaced parallel plates using a Flat-Plate tester. The device is designed to measure the pressure gradient along the test specimen. The main function of the Flat-Plate tester is to provide friction factor data and measure dynamic pressure oscillations. A detailed description of the test facility is described, and a theory for determining the friction factor is reviewed. Three clearances were investigated: 0.635, 0.381, and 0.254 mm. Tests were conducted at three different inlet pressures (84, 70, and 55 bars), producing Reynolds numbers range from 50,000 to 700,000. Three surface configurations were tested including smooth-on-smooth, smooth-on-hole, and hole-on-hole. The Hole-pattern plates are identical with the exception of the hole depth. The results indicate that, for the smooth-on-smooth and smooth-on-hole configurations, the friction factor remains constant or increases slightly with increasing Reynolds numbers. Moreover, the friction factor increases as the clearance between the plates increases. However, the results from the hole-on-

hole configurations are quite different. A “friction-factor jump” phenomenon was observed, and the Helmholtz frequency was detected on the frequency spectra.

DEDICATION

This thesis is dedicated to my parents, Ali and Hana, for their unconditional love and support throughout the course of this thesis. To my aunt, Baria, whose endless support helped shape the person I have become.

ACKNOWLEDGMENTS

The author would like to acknowledge the contribution and extensive knowledge of Dr. Dara Childs, whose patience and guidance were invaluable. Many thanks also go to Dr. Gerald Morrison and Mr. Stephen Phillips whose insight and creative ideas were extremely helpful. I would also like to extend my thanks to the sponsoring companies for their support on both the financial and intellectual level. Finally, I would like to thank Chris Kulhanek for his help in assembling and operating the test apparatus.

TABLE OF CONTENTS

Page

LIST OF FIGURES

Page

Page

Page

Page

Page

Page

LIST OF TABLES

Page

NOMENCLATURE

A Cross sectional area [L^2]

A_s Surface area [L^2]

C, c Direct and cross-coupled damping coefficients [FT/L]

c Speed of sound [L/T]

C_p Clearance between plates [L]

Cr Radial clearance [L]

d Hole depth [L]

dx Length of control volume [L]

D Duct diameter [L]

D_h Hydraulic diameter [L]

f, f_f Friction factor [-]

f_{res} Resonant frequency [T^{-1}]

F Force [F]

H Channel height [L]

K, k Direct and cross-coupled stiffness coefficients [F/L]

L Duct length [L]

L_{max} Length at which choking occurs [L]

L_p Hole-pattern length [L]

M Mach number

$\dot{m}$ Mass flow rate [M/T]

Ø Hole diameter [L]

P Pressure [F/L^2]

P_{in} Inlet pressure [F/L^2]

ΔP Pressure gradient [F/L^2]

R Air gas constant [FL/MT]

Re, R_n Reynolds Number

ρ Air density [M/L^3]

T Temperature [K]

T_t Stagnation temperature [K]

τ_f Shear stress due to wall friction [F/L^2]

V Fluid velocity [L/T]

W Channel width [L]

X Horizontal coordinate

Y Vertical coordinate

ACRONYMS and TERMS

Eq. (Equation)

HP (Hole-pattern)

Forward process (Page 32)

Reverse process (Page 38)

INTRODUCTION

Annular Honeycomb and Hole-pattern seals are used on a regular basis in high pressure compressors and other turbomachinery applications. They employ a smooth rotor and a roughened stator. For small motions of the rotor about a centered position, the rotor-to-seal interaction force is described by the following equations :

$$-\begin{Bmatrix} F_X \\ F_Y \end{Bmatrix} = \begin{bmatrix} K & k \\ -k & K \end{bmatrix} \begin{Bmatrix} X \\ Y \end{Bmatrix} + \begin{bmatrix} C & c \\ -c & C \end{bmatrix} \begin{Bmatrix} \dot{X} \\ \dot{Y} \end{Bmatrix} \tag{1}$$

where X and Y are the displacements of the rotor relative to the seal, and F_X and F_Y are the components of the reaction forces acting on the rotor in the X and Y directions, respectively. K is the direct stiffness, k is the cross-coupled stiffness, C is the direct damping and c is the cross-coupled damping. K, k, C and c are referred to as the rotordynamic coefficients [1]. The direct stiffness represents a centering force opposed to the rotor's displacement, a behavior known as the "Lomakin" effect. The cross-coupled stiffness represents a tangential force that can destabilize the rotor. The bulk-flow theory is the most widely used method to evaluate the rotordynamic coefficients of annular seals. Originally developed by Hirs [2], this theory uses averaged pressure, averaged flow velocity and an empirical friction factor data correlation to

---

This thesis follows the style of *ASME Journal of Tribology.*

help determine the coefficients. Not only is the friction factor data employed to evaluate rotordynamic coefficients, it also helps determine which surface reduces leakage the most. From this standpoint, the flow of fluids becomes of considerable importance in the design of annular seals.

The main function of a seal is to reduce leakage. The most popular seal used is the Labyrinth seal because of its relatively cheap cost. However, instabilities have been attributed to labyrinth seals in steam turbines and high pressure injection compressors. Instabilities like this have necessitated the need for advancing a new seal technology. In 1982, Von Pragenau introduced the concept of liquid damper seals [3]. He maintained that the use of intentionally roughened stators with smooth rotors yields a lower circumferential velocity. Consequently, the cross-coupled stiffness is reduced, which translates into an enhancement in the rotordynamic stability. An example of this enhancement is cited by the work of Childs and Moyer [4] on the vibration characteristics of the HPOTP (High-Pressure Oxygen Turbopump) of the SSME (Space Shuttle Main Engine). The use of a honeycomb seal (figure 1) had a significant effect on reducing synchronous vibrations. Zeidan [5] also reported that replacing the labyrinth seal with a honeycomb seal contributed to the stability of two centrifugal compressors.

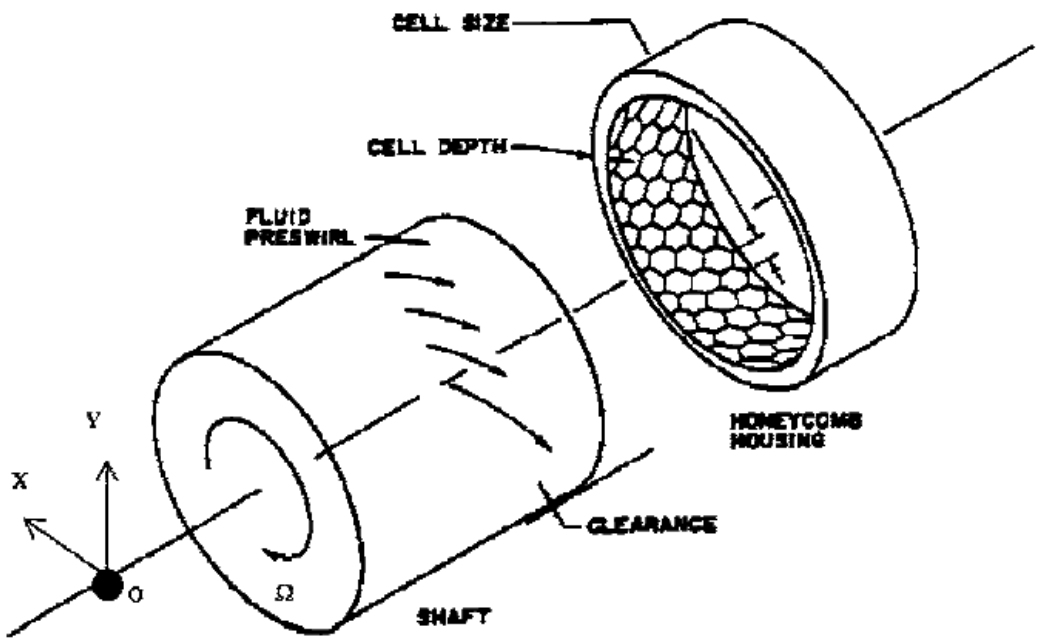

Figure 1. Honeycomb Seal- Soulas [6]

The previous examples discussed the effects of using honeycomb seals on the rotordynamic stability. The work of Childs et al. [7] compared the leakage characteristics of labyrinth, smooth and honeycomb surfaces. Their results show that the honeycomb seal provides the minimum leakage out of all three surfaces. Honeycomb seals, however, are expensive to manufacture and the need of an alternative cost effective damper seal became evident. Hole-pattern seals (figure 2) have shown similar characteristics to honeycomb seals and are less expensive to manufacture. Childs and Yu [7] have reported test results on Hole-pattern seals and compared them to those of honeycomb seals. They found that the Hole-pattern seals displayed similar characteristics to their honeycomb counterparts.

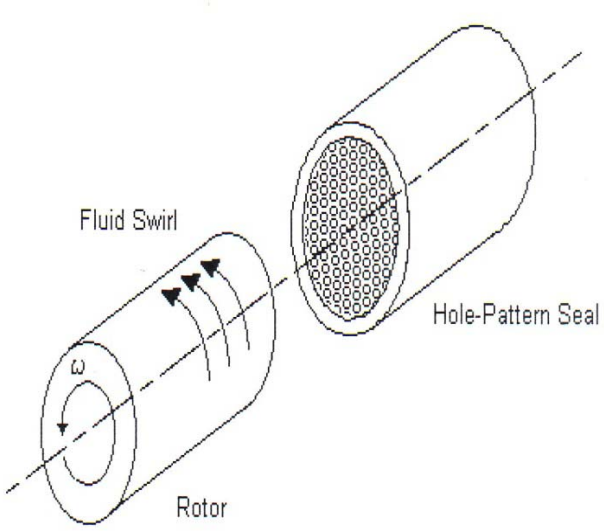

Figure 2. Hole-pattern Seal-Wade [8]

The friction factor plays an important role in determining the leakage characteristics of a given surface. In 1944, an American engineer by the name of Lewis F. Moody developed his widely used Moody diagram for commercial circular pipes [9]. For generations, the Moody diagram has been used to predict friction factors at certain flow conditions. Moody stipulates that the friction factor is a function of the Reynolds number, Re, and the surface roughness (e/d). According to Moody, the friction-factor decreases asymptotically with increasing Reynolds numbers. Moreover, the friction-factor for smooth pipes is lower than rough ones. Moody's diagram, however, is mostly applicable to commercial pipes and conduits of circular shapes. It considers the height of surface roughness, but does not take into account the spacing of these irregularities in the surface. Since then, numerous studies on pipe flow have been conducted and

information on the friction factor data is well documented. However, there exists little information on friction factor data for closely spaced parallel plates (i.e.channel flow). The parallel plates form a rectangular channel with a clearance significantly smaller than the width of the channel (i.e. W/H >> 1). Relatively recently, Ha [10] presented friction factor data using a flat-plate tester with air as the working fluid. Ha tested air passing between honeycomb surfaces (i.e. 1.57, 0.79, and 0.51 mm in cell width, 3.81 and 2.29 mm in cell depth). Three clearances were tested (i.e. 0.25, 0.38 and 0.51mm) at 5 different inlet pressures (6.9, 9.7, 12.4, 15.2, and 17.9 bar). In general, Ha's results show that the honeycomb surfaces yield larger friction-factor values than smooth surfaces. In most of the test cases, the friction factor remains nearly constant or decreases slightly with increasing Reynolds numbers in a fashion similar to that of the Moody diagram. However, in about 34% of the test cases, Ha observed a friction–factor jump phenomenon when testing opposed honeycomb surfaces. The friction-factor-jump is a significant increase in the friction-factor over small changes in the Reynolds numbers. Ha stipulates that the cause of this jump is due to a known cavity-flow phenomenon, which led him to instrument his test specimen with a dynamic pressure sensor in order to detect pressure oscillations in the cavity. In the cases where the friction-factor jump is present, Ha detected high pressure oscillations that he believes are the result of a normal mode resonance accompanied by harmonics of the Helmholtz frequency. However, in the non-friction-factor-jump cases, Ha detected two dominant frequencies: normal mode resonance and feedback mode resonance [11]. He

concluded that the absence of harmonics is a characteristic of the non-friction-factor jump cases. This friction-factor jump phenomenon can have serious consequences on the rotordynamic stability and became of a serious concern to the seal industry. Through the Lomakin effect, seals are expected to produce a positive direct stiffness given that the friction factor decreases with increasing Reynolds number. If the friction factor increases with increasing Reynolds number, the seal can produce a negative stiffness. ISOTSEAL, a code used in the Turbomachinery Laboratory at Texas A&M University, predicts that a negative stiffness can be produced in the case of a friction-factor-jump. Childs believes that this negative stiffness is enough to cause the seal to adhere to the rotor on his rotating test-rig (private conversation with Dr. Dara Childs).

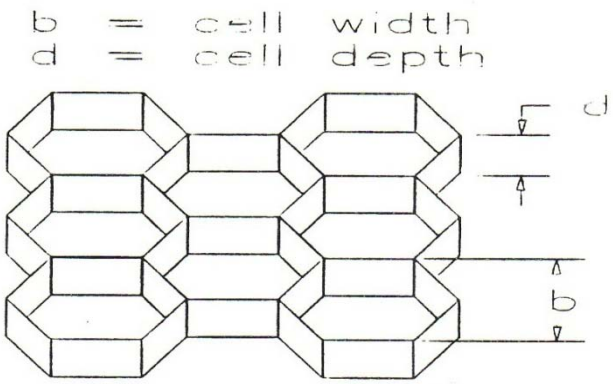

Figure 3. Honeycomb cell pattern used in Ha's investigation [10].

Thomas [12] used a different flat-plate tester and performed tests for closely-spaced plates with water as the working fluid. He investigated various configurations

including, smooth-on smooth, smooth-on-knurl (small and large knurls), and smooth-on-hole. Similar to Moody and Ha (except in the jump cases), Thomas observed that the friction factor decreases with increasing Reynolds numbers. Furthermore, Thomas determined that the smooth-on-hole configuration provides the lowest friction-factor data. Most studies, however, show that the smooth-on-smooth configuration yields the lowest friction factor. He also found that the friction factor increases with increasing clearance. However, there exists a clearance, referred to as a plateau, at which the friction factor ceases to increase.

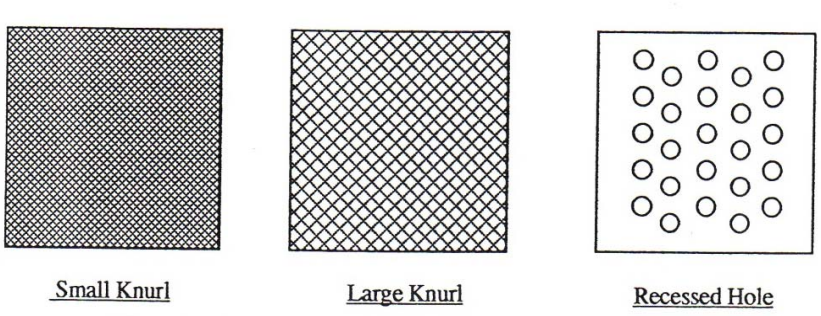

Figure 4. Patterns used in Thomas' investigation.

Nava [13] used the same flat-plate tester to further investigate Thomas' results. Her main goal was to find the plateau for each configuration and explore the variables that affect it. She examined configurations such as small and large knurls and small and large recessed holes and tested them in combination with a smooth plate. Nava found that the small and large knurls had a plateau of 0.508 mm, whereas the small and large

recessed holes had a plateau of 0.762 mm. Moreover, the large knurl size provided the highest friction factor, and as expected, the smooth-on-smooth configuration yielded the lowest friction factor.

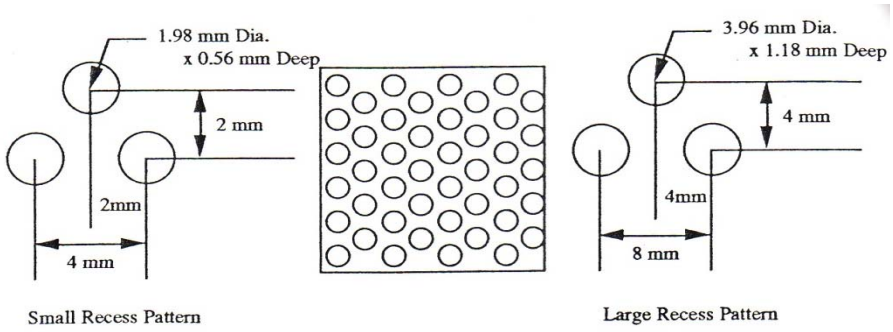

Figure 5. Small and large recess patterns used in Nava's investigation.

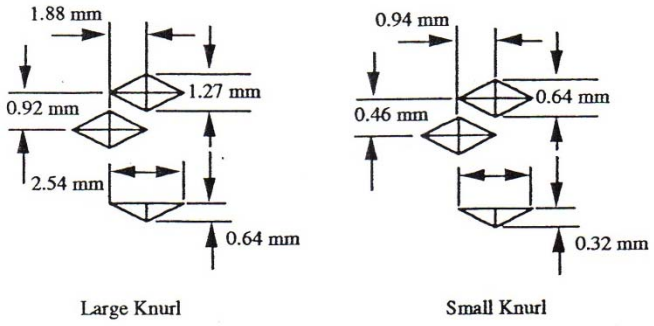

Figure 6. Small and large patterns used in Nava's investigation.

Villasmil [14] used a commercial CFD code to simulate the results obtained by Nava. Although the trends in the experimental and numerical results were very similar, the numerical simulation overestimated the friction factors. Moreover, the numerical

simulations reproduced the plateau phenomena for the small knurl pattern only. For the large knurl and large recessed holes, for the larger clearances the curves lay almost on top of each other leading to the belief that the plateau phenomena might occur. However, in a certain Reynolds number range, there is little dependence of the friction factor on the clearance in what Villasmil [15] referred to as the friction-factor-to-clearance indifference behavior.

This increase in the friction factor with increasing clearance conflicts with Moody's friction-factor diagram for pipe flow. From the Moody diagram, for a constant Reynolds number, the friction factor decreases with increasing clearance. Results by Ha and Childs for air flow between honeycomb surfaces show that the friction factor increases with increasing clearance. Similar results were obtained by DeOtte et al. [16] for water flow between closely spaced parallel plates. Fayolle and Childs [17] conducted tests for two identical liquid Hole-pattern seals except for the hole depth. Their results show an increase in the friction factor with increasing clearance and a major loss in the direct stiffness. This result was explained by examining the partial derivative of the friction factor with respect to clearance as shown in equation (2).

$$f_f + \Delta f \equiv f_{f_0} + \left.\frac{\partial f_f}{\partial R_n}\right|_{Cr} \cdot \Delta R_n + \left.\frac{\partial f_f}{\partial Cr}\right|_{R_n} \cdot \Delta Cr \tag{2}$$

From the Moody diagram, since the friction factor decreases with increasing Reynolds number and increasing clearance, both partial derivatives shown in Eq. (2) are negative. However, based on the results obtained by Fayolle and Childs, the first partial

derivative is negative and the second derivative is positive and becomes more dominant especially in the turbulent regime. Therefore, the net effect yields a significant reduction in the direct stiffness.

In summary, friction-factor data play an important role in the design of annular seals. Several experiments have been conducted involving incompressible flow in circular pipes. However, there is minimal friction factor data for compressible flow between closely spaced parallel plates. The friction-factor-jump phenomenon observed by Ha has raised concerns over the acceptance of using seals that exhibit this phenomenon. This thesis will examine the friction-factor-jump phenomenon observed by Ha. It also documents the results of high-pressure testing of Hole-pattern (HP) plates using the flat-plate tester developed at the Turbomachinery laboratory at Texas A&M University. Three surface configurations were tested including smooth-on-smooth, smooth-on-hole, and hole-on-hole configurations. The HP plates have been tested at three different clearances and three different inlet pressures to examine the effect of clearance and inlet pressure on the friction factor. The air flow is highly turbulent with Reynolds numbers ranging from 50,000 to 700,000.

THEORY

The derivation of the friction-factor formula based on the Fanno line flow for compressible flow in rectangular channels is the subject of this section. The test section represents a rectangular channel that can be modeled by the control volume shown in figure 7. The following derivation is obtained from Dr. G. Morrison's class notes [18] and John and Keith [19].

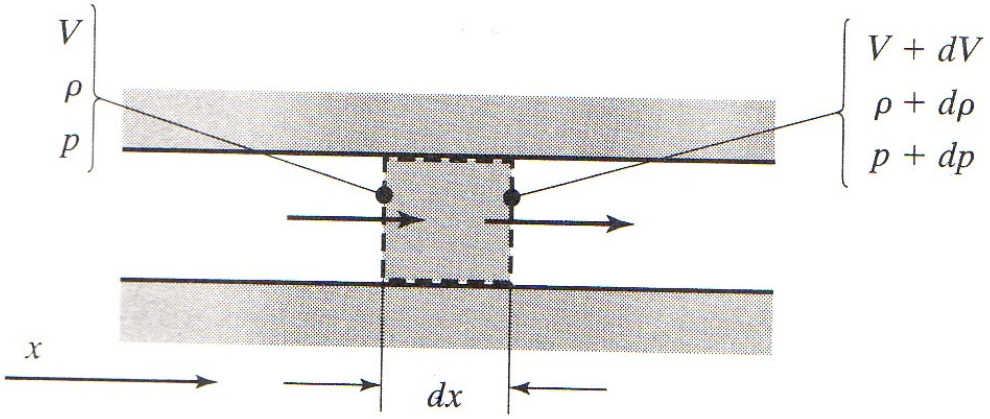

Figure 7. Control Volume for adiabatic , constant area channel flow.

One dimensional flow is assumed since the width-to-height ratio is large (i.e. W/H >>1). To simplify the analysis of this section further, air is assumed to be an ideal gas with constant specific heats. The effects of area change as well as the body forces and work crossing the control surface can be neglected. The air flow is assumed to be steady and adiabatic. The aforementioned assumptions constitute what is called the

Fanno line flow. The momentum equation in the x-direction for the control volume shown in the figure above yields:

$$-\tau_f A_s - AdP = \rho AVdV \tag{3}$$

where τ_f is the shear stress due to wall friction, A_s is the surface over which the frictional forces act and A is the cross-sectional are of the rectangular channel

The hydraulic diameter is defined by:

$$D_h = 4\frac{Cross-SectionalArea}{WettedPerimeter} \tag{4}$$

For a rectangular channel,

$$D_h = 4\frac{WH}{2(W+H)} \tag{5}$$

where W and H are the width and height of the rectangular channel, respectively.

In this specific case, since the width is very large compared to the height of the channel, D_h reduces to:

$$D_h = 2H \tag{6}$$

Define the friction factor as:

$$f = 4\frac{\tau_f}{0.5\rho V^2} \tag{7}$$

Substituting the friction factor definition into the momentum equation yields:

$$-dP - \frac{1}{2}\rho V^2 f\frac{dx}{D_h} = \rho VdV \tag{8}$$

The Mach number M is related to the velocity of the fluid by the following formula:

$$M = \frac{V}{\sqrt{\gamma RT}} \tag{9}$$

where γ is the ratio of specific heats and R is the gas constant for air.

The stagnation temperature and the static temperature are related by:

$$T_t = T(1+\frac{\gamma-1}{2}M^2) \tag{10}$$

This derivation aims to arrive at a relationship between the friction factor, the Mach number and the Mach number gradient. The following equation for the Mach number is derived from the conservation of mass, the ideal gas law, and the definitions of the Mach number and the stagnation temperature.

$$M = \left(\frac{-1+\sqrt{1+2(\gamma-1)(\frac{\dot{m}}{PA})^2(RT_t)}}{(\gamma-1)} \right)^{\frac{1}{2}} \tag{11}$$

where $\dot{m}$ is the mass flow rate through the test section.

In Eq. (11), $\dot{m}$, P, and T_t are measured quantities, whereas, R, γ and A are known quantities. Hence, the calculation of the Mach number becomes fairly simple. Using the equations above:

$$f = \frac{4H(1-M^2)}{\gamma M^3(1+\frac{\gamma-1}{2}M^2)}\frac{dM}{dx} \tag{12}$$

The Mach number gradient, $\frac{dM}{dx}$, is evaluated using the central difference method (i.e. $\frac{M_{i+1} - M_{i-1}}{2\Delta x}$) .Therefore, with knowledge of the Mach number and the evaluation of the Mach number gradient, the friction factor can be readily calculated.

TEST APPARATUS

A flat-plate tester enables a relatively rapid determination of friction factors for a variety of surfaces including smooth and roughened surfaces. The test facility is designed to simulate clearances between a smooth surface (i.e. rotor) and a rough surface (i.e. stator). This particular test rig utilizes high-pressure air as the working fluid. The test specimens consist of stainless steel plates that can easily be mounted on the backup plates through the use of screws. Figure 8 below depicts a simplified schematic of the test facility.

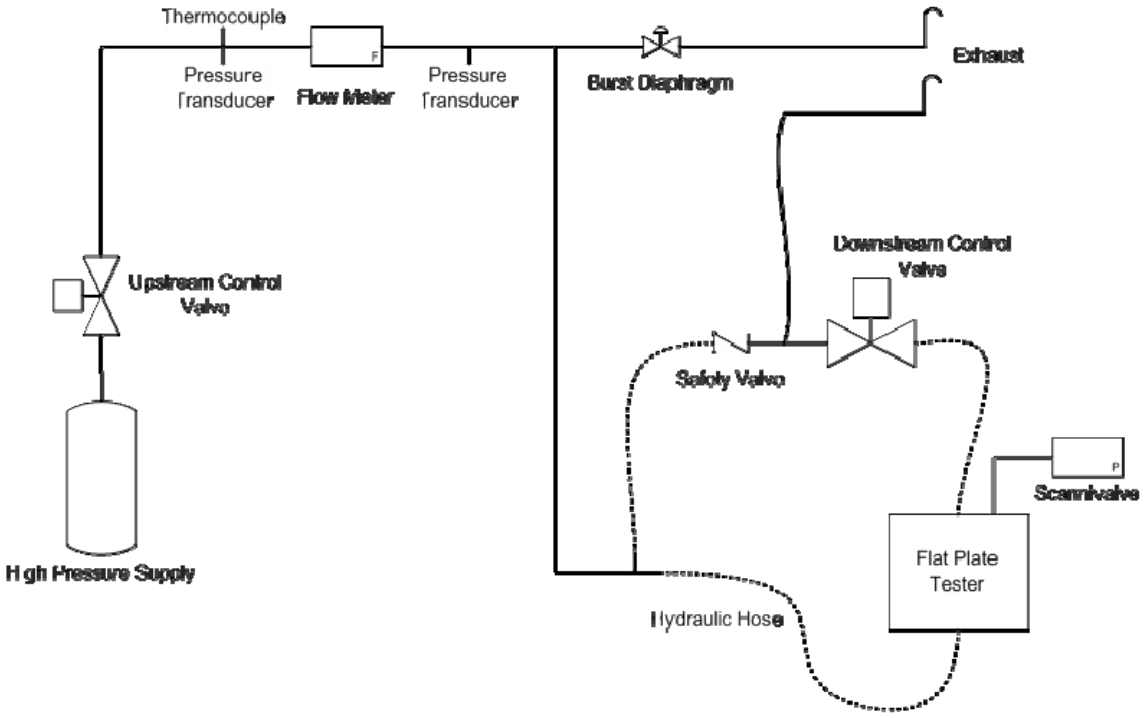

Figure 8. Flow Loop

The high-pressure air is stored in a tank at a nearby facility. This particular setup is rated for 104 bars, and a safety valve is used to ensure that the pressure in the test section does not exceed this value. An inlet control valve is used to allow the passage of air into the system. Downstream of the test section is a backpressure valve that allows controlling of the exit pressure.

The flat-plate tester consists of backup plates, a boundary vessel, and the test specimens. A detailed view is shown in figure 9 below.

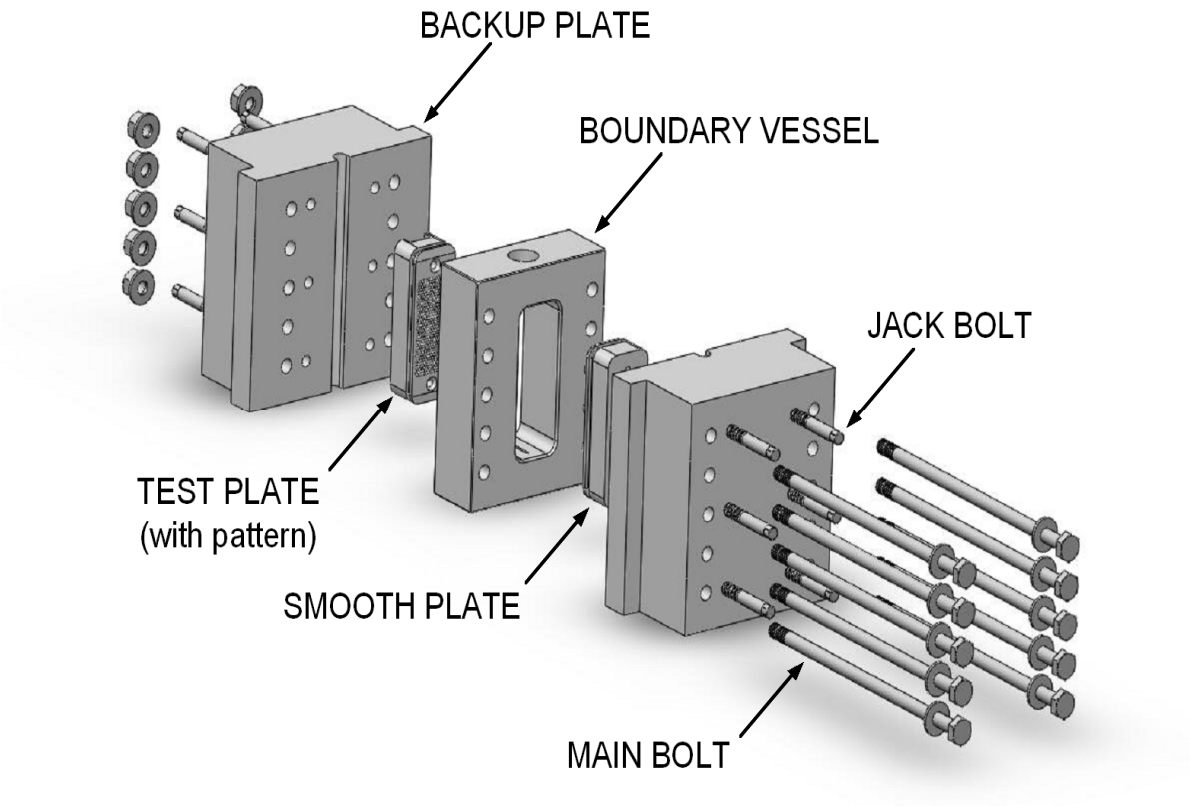

Figure 9. Detailed view of the flat-plate tester.

Description of the Test Plates

The test plates have two distinct surfaces: smooth and rough. The smooth plate is made out of 410 annealed stainless steel with a very high yield strength to withstand the high-pressure air. Figure 10 below shows a detailed view of the smooth plate. The dimensions of the plate are 4.45 cm x 6.35 cm x 15.24 cm. A groove runs along the periphery of the plate and serves as a place for a 352 O-ring and two backup rings to insure that air does not escape. The plate has two countersunk holes to allow its attachment to the backup plates.

Figure 11 shows the back face details of the smooth plate. The plate is instrumented with four subminiature dynamic pressure sensors located along the plate's length. The dynamic pressure sensors are installed flush with the smooth surface as shown. Miniature holes at the inlet and exit of the smooth plate serve as locations for temperature and pressure measurements. The Hole-pattern (HP) plate is almost identical to the smooth plate. They both have the same dimensions and are made out of the same material. Circular flat-bottom holes with a specified hole depth are drilled into the smooth surface as shown in figure 12. The back face details of the HP plate are depicted in figure 13. The HP plate is equipped with nine static pressure probes and four dynamic pressure sensors located along the length of the plate. The dynamic pressure sensors are mounted flush with the bottom of the holes.

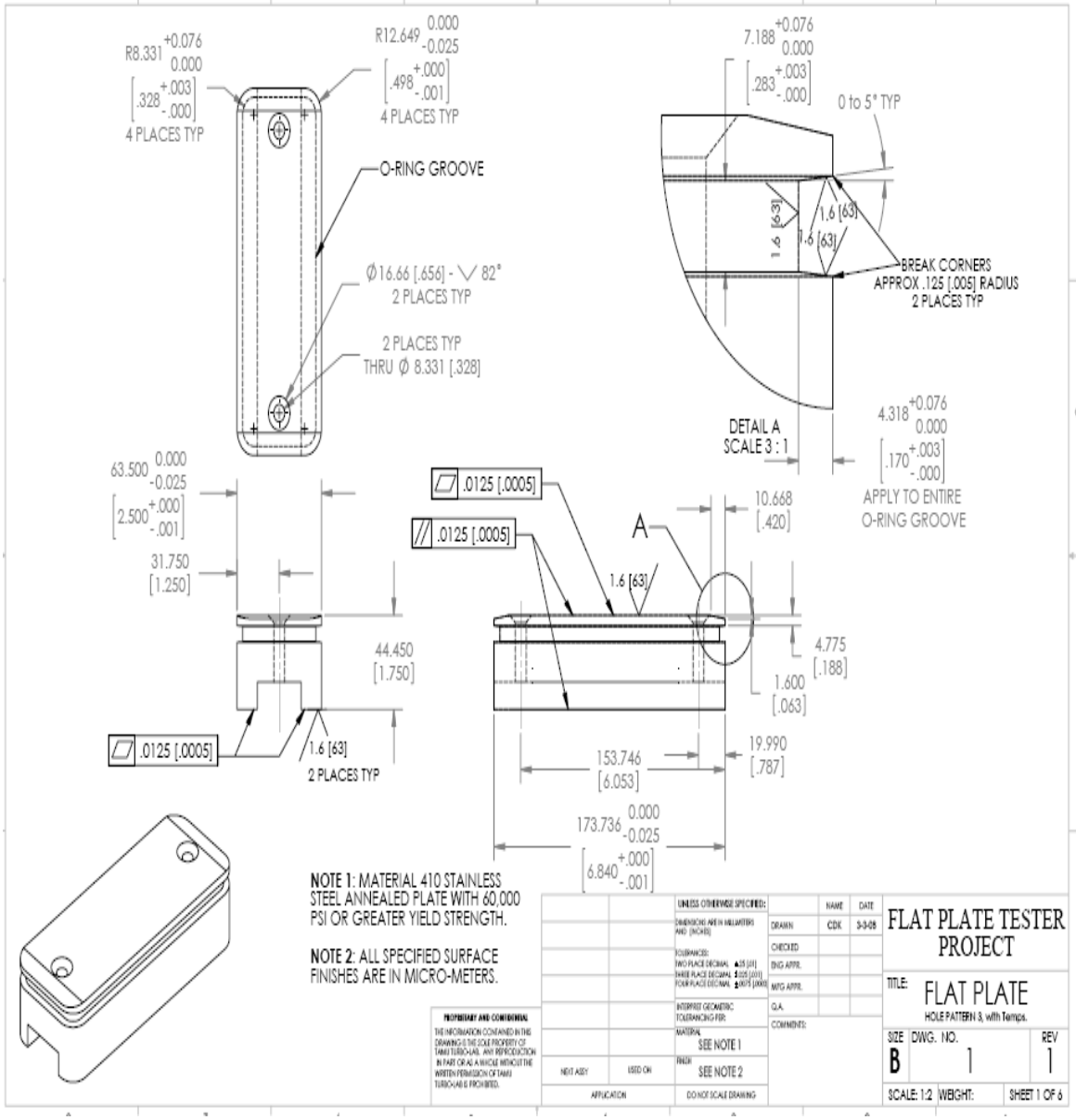

Figure 10. Smooth plate drawing.

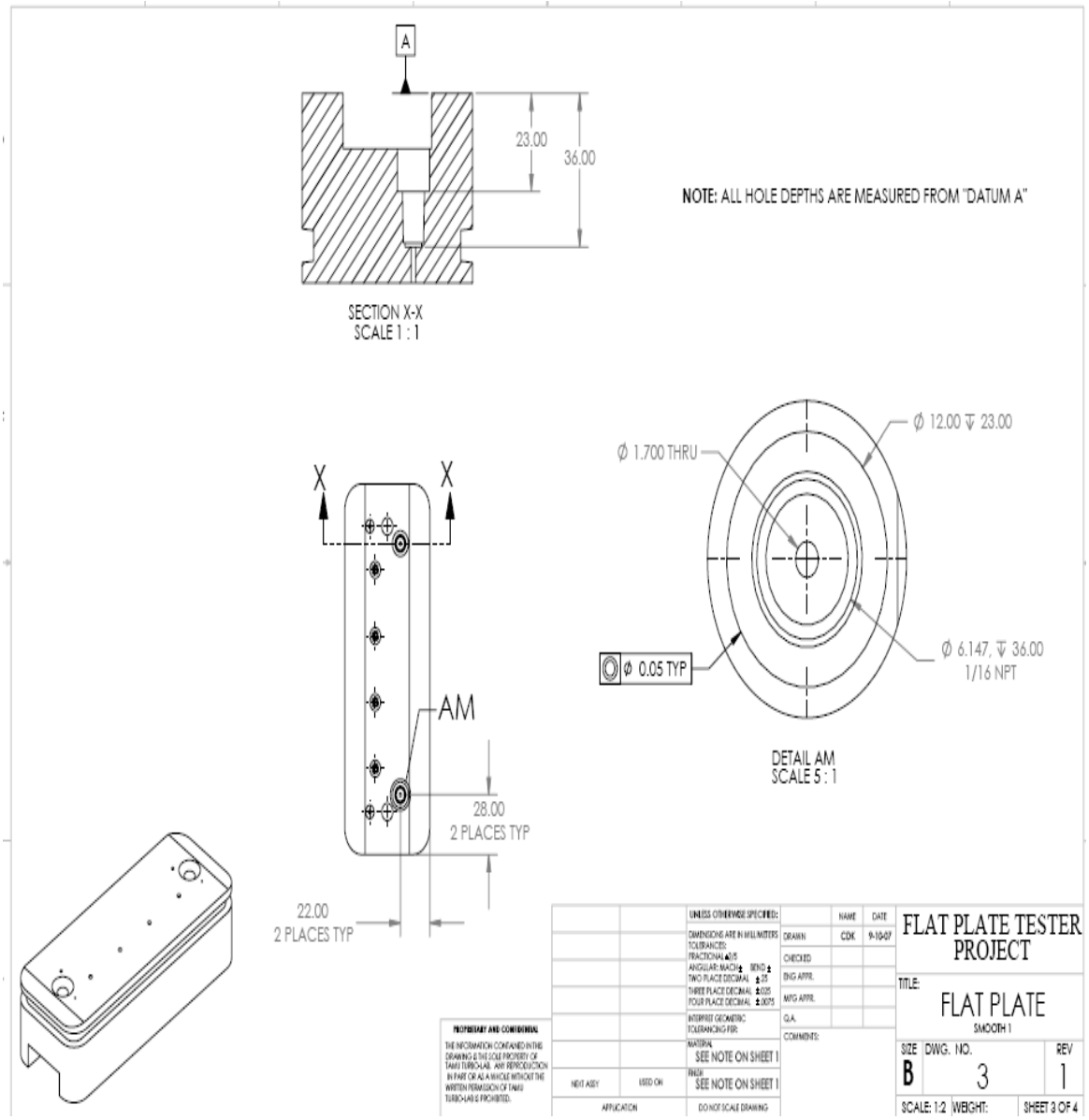

Figure 11. Back face details of smooth plate.

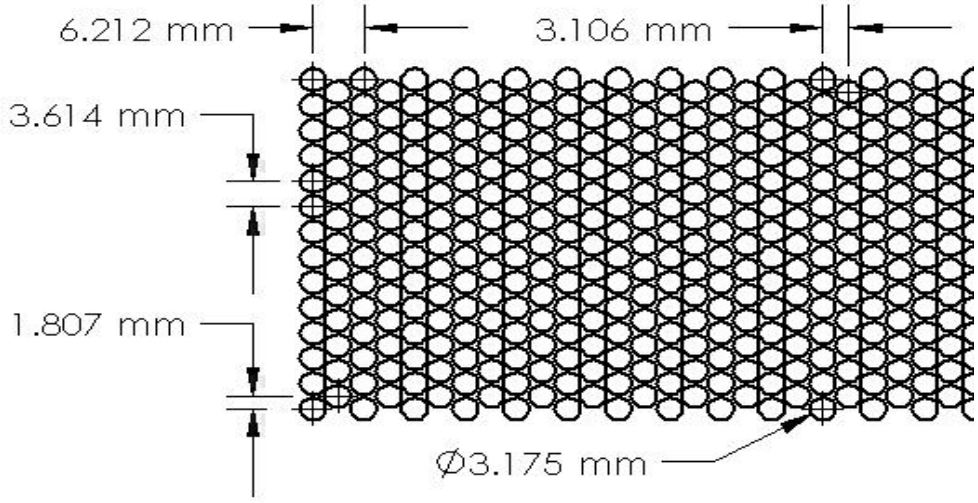

Figure 12. Hole-pattern used in this study.

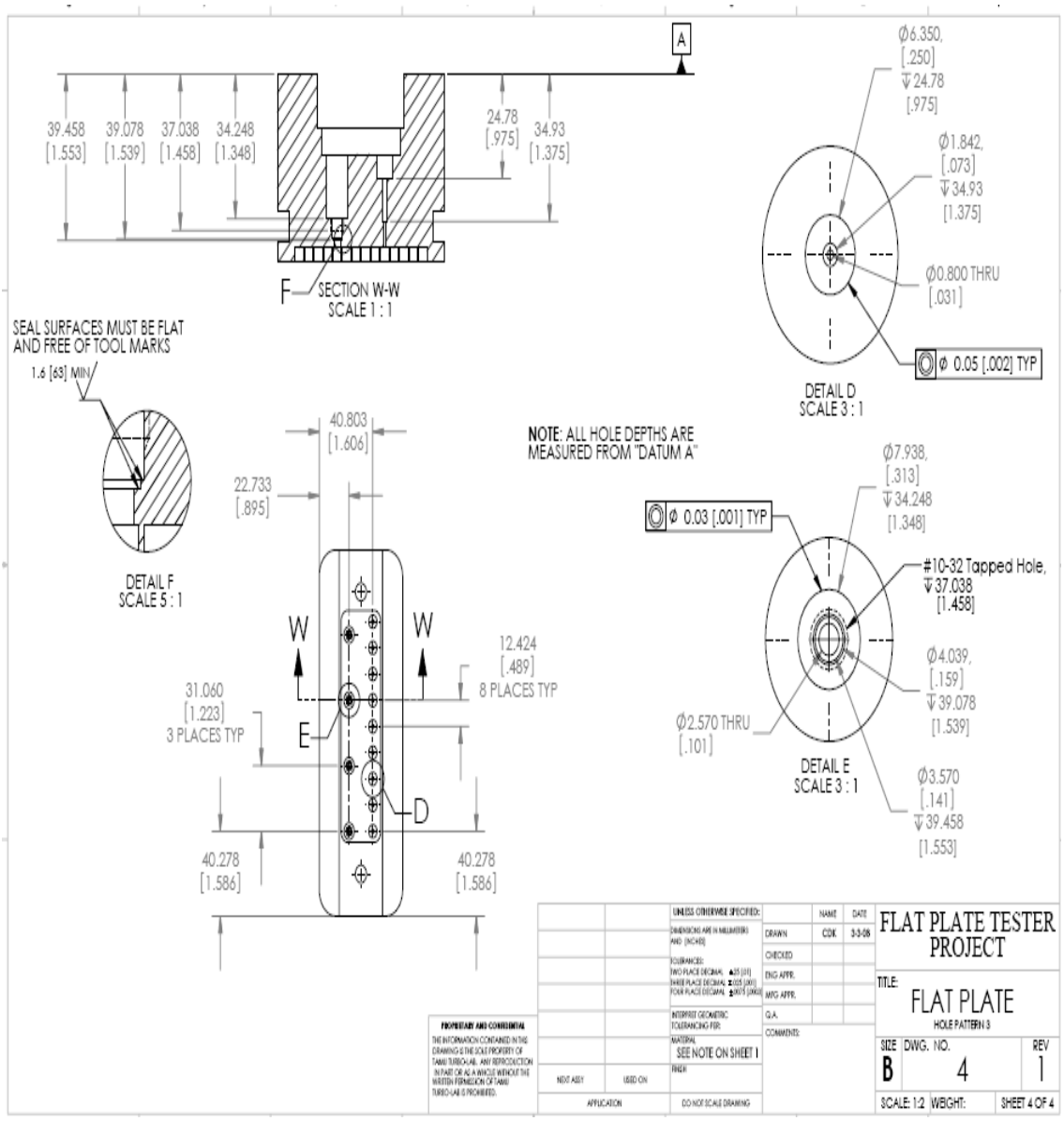

Figure 13. Back face details of Hole-pattern plate.

Boundary Vessel

The boundary vessel (figure 14) is the center piece of the assembly. It has a doughnut shape and contains a rectangular window where the test plates are inserted from both sides and come together. At the inlet and exit of the boundary vessel, an aperture of rectangular shape allows the air flow in and out of the test section. Ten holes on each side of the vessel allow it to be aligned with the cover plates with the use of 5/8 x 16 UNF carbon steel bolts.

Backup Plates

The backup plates (figure 15) consist of heavy blocks of 316 stainless steel. Ten outer holes on both sides of each cover plate are aligned with the holes in the boundary vessel. Six inner holes on each cover plate contain brass pins and serve as tool to disassemble the test rig and as an adjustment of the clearance between the plates. The entire assembly is pulled together by using 5/8 x 16 UNF carbon steel bolts. The test specimens are rigidly bolted onto the cover plates through the use of flat head screws.

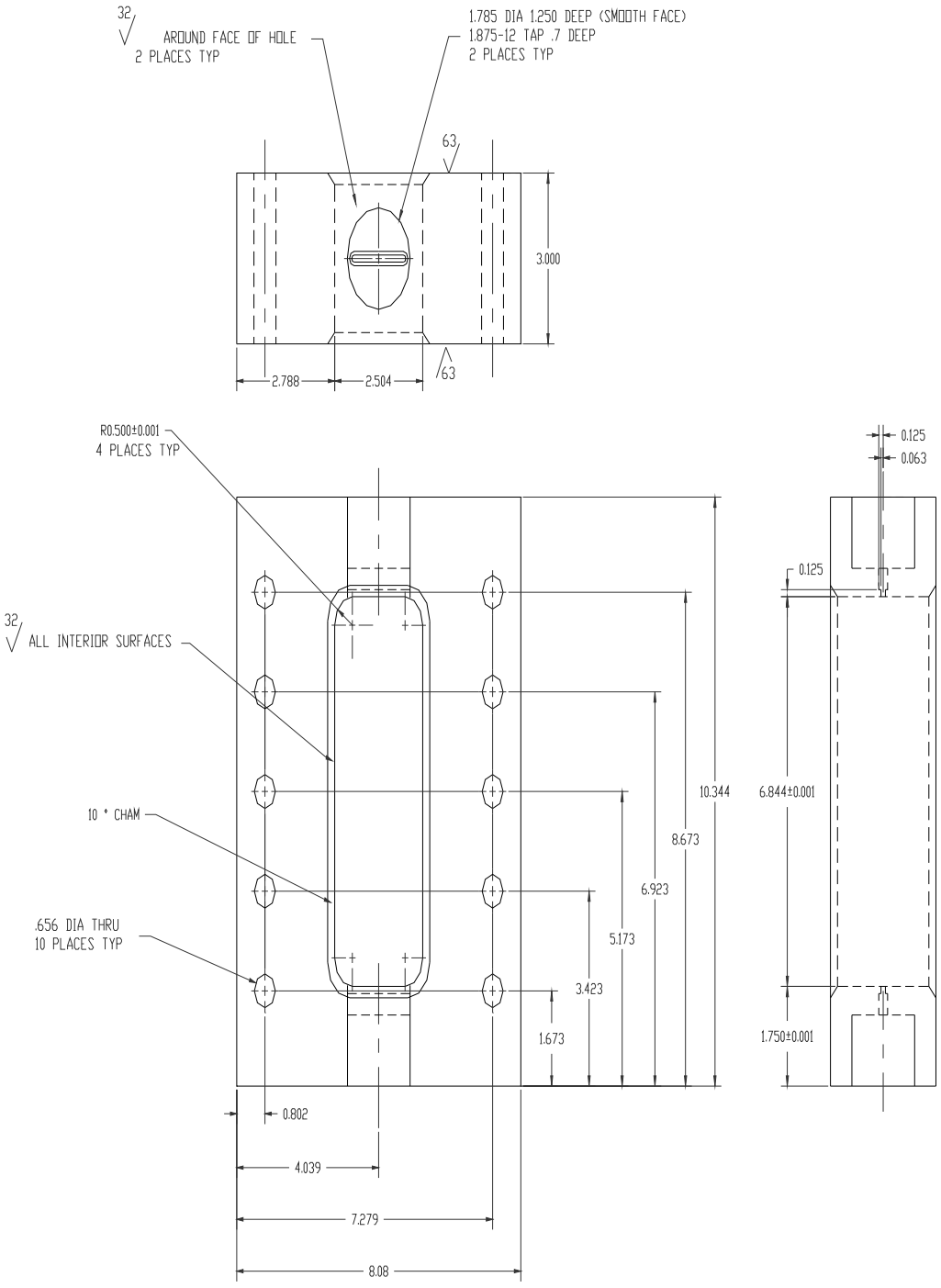

Figure 14. Detailed drawing of the boundary vessel-Hess [20]

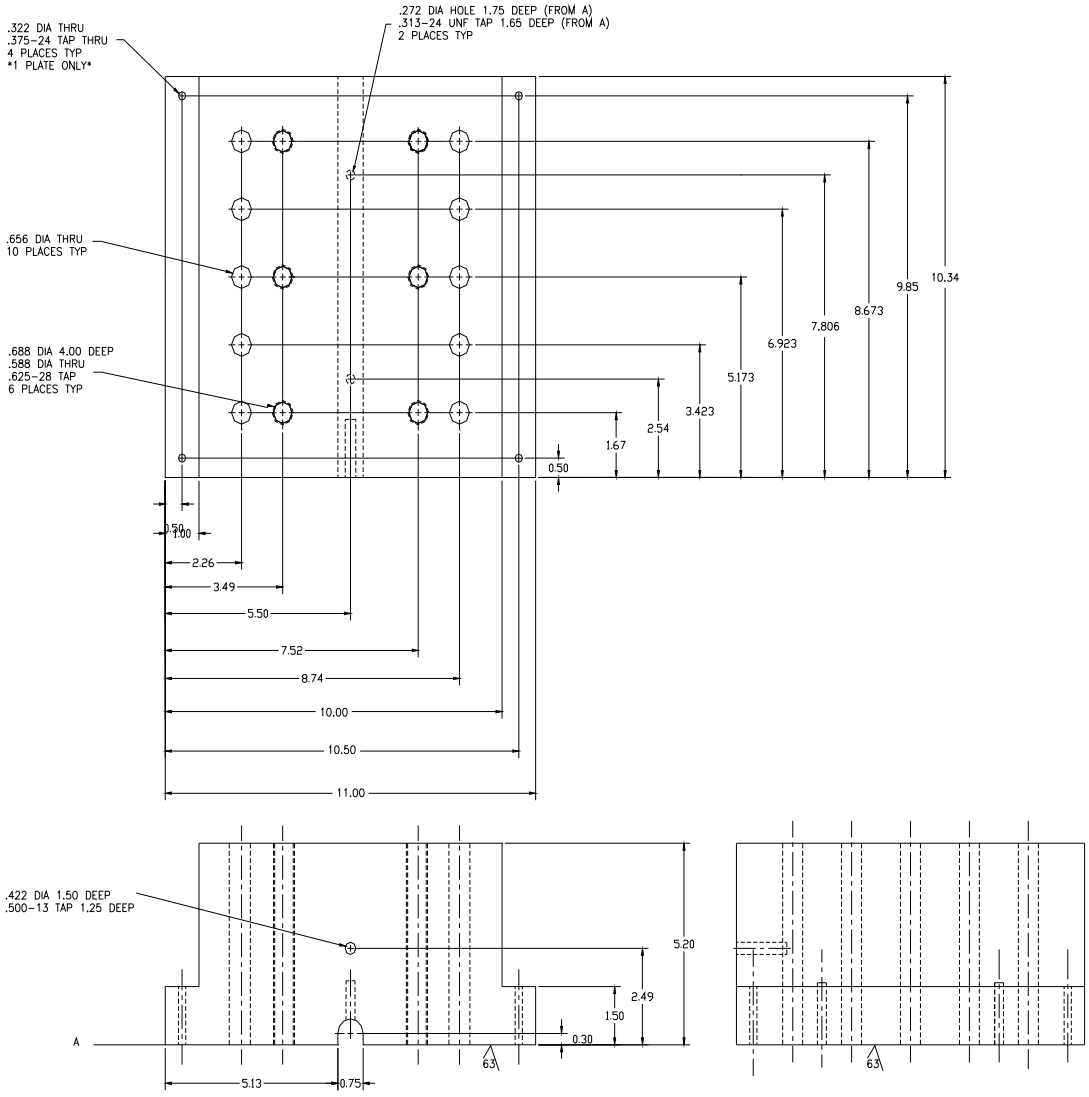

Figure 15. Detailed drawing of backup plates-Hess [20]

Instrumentation

As mentioned before, the flat-plate tester is used to obtain friction factor data. To achieve this task, measurements of pressure, temperature, and flow rate are required. The inlet control and backpressure valves are controlled via an electronic circuit that sends a 4-20 mA signal. Downstream of the inlet control valve is a turbine flow meter engineered by Flow Technology. The turbine flow meter has been calibrated at a pressure of 84 bar and a temperature of 295 °K. It is connected to a digital readout which displays readings in acfm (actual cubic foot per minute) and has an accuracy of ± 0.25%. Two Omega Engineering pressure transducers are positioned upstream and downstream of the turbine meter. The high performance pressure transducers are made out of stainless steel and are accurate to within ± 0.25%. Two additional pressure transducers are located at the inlet and exit of the flat plate tester. Prior to their use, the pressure transducers have been calibrated in-situ with a dead weight tester. These transducers are also connected to a digital readout that converts voltages to pressure readings. A type K thermocouple is located upstream of the flow meter, and two additional thermocouples are located at the inlet and exit of the smooth plate to allow measurements of the inlet and exit temperatures. The thermocouples are accurate to within ± 1° F, and are connected to a digital readout that converts voltages to temperature readings. The pressure, temperature and flow rate digital displays are connected to a NI Data Acquisition Board and a labview program is used to collect the data. A 32-V power supply is used to power all the instruments.

The static pressure probes along the test plates are made out of stainless steel tubes. The tubes are connected to the back of the test plates through the use of epoxy. This was achieved with extreme care to insure that the tubes do not kink or bend so as to block the air flow. The epoxy is allowed to cure for 24 hours before the use of the test plates. The desired plates are mounted on the cover plates and secured in position. Two Stainless steel shims of known thicknesses are used to set the clearance between the plates. The shims are 0.635 cm x 15.24 cm in dimensions and are greased onto the plates. Clearance tests were conducted using the method of fuse wires. Three fuse wires of known thickness were placed along the length of the plate. After the plates come together, measurements are taken at six points along the length of the wire. The results indicate that the clearance error percentage is within ± 3% for the 0.381 mm clearance and ± 4% for the 0.254 mm clearance as shown in Figure 16.

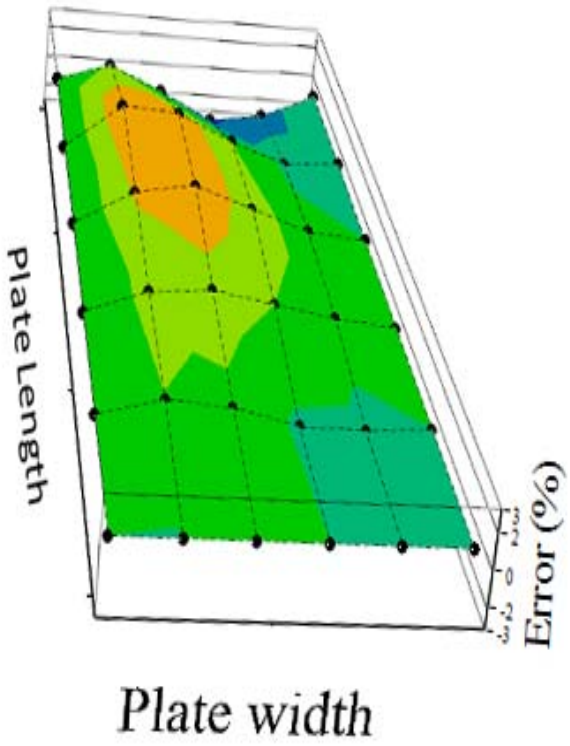

Figure 16. Error distribution for the 0.381 mm clearance.

The assembly process begins by inserting the plates into the rectangular window of the boundary vessel. Using a torque wrench, the bolts are tightened evenly back and forth until the plates come in contact with each other. Stainless steel tubes and compression fittings are used to connect the static pressure probes to the Scanivalve. This particular module has 16 ports that allow multiple-point measurements of the static pressures along the plate. It contains a RAM, 16 bit A/D converter and a microprocessor and communicates with a PC through an Ethernet TCP/IP Protocol. Also

mounted on the back face of the plates are the dynamic pressure sensors; four of these sensors were mounted flush with the surface of the smooth plate and the remaining four were mounted flush with the bottom of the holes of the HP plate. The dynamic pressure sensors are connected to a Dynamic Data Acquisition Board through a BNC to SMB cables. This NI PCI 4472 DAQ board is also used to power these subminiature ICP pressure sensors.

Testing Procedure and Data Acquisition

Arrangements are made with the staff at the low speed windtunnel facility one day before testing is to take place. A high-pressure air tank is found outside the facility and is pressurized using two air compressors. Once the pressure in the tank reaches 104 bars, the compressors are turned off. Each day of testing begins by verifying that all instrumentation involved is working properly. The desired plates are mounted on the cover plates and secured in position. Before the data acquisition process begins, the entire system is checked for unwanted leakage. This process is achieved by opening the inlet control valve while keeping the backpressure valve closed. Once the pressure in the system reaches 84 bars, the inlet control valve is closed and the pressure in the system is monitored. If no major leaks are found, testing may begin. To avoid malfunction of the flow meter, the inlet control valve is opened slowly while the backpressure valve is in the closed position. Once the entire system is pressurized to the desired pressure, the backpressure valve is slowly opened until a maximum

pressure differential is established. The pressure drops are then achieved by closing the backpressure valve while maintaining a constant inlet pressure value. This procedure is repeated for inlet pressure values of 84, 70, and 55 bar and for clearances of 0.635, 0.381 and 0.254 mm. Once steady state flow conditions are established, data are collected through a labview program. At the end of the testing day, the flow meter is disconnected from the flow loop and flushed with denatured alcohol to remove any moisture that can cause erratic readings in future testing.

Data Reduction

Tests are performed with smooth and hole pattern surfaces as listed in Table 1. Static data including pressures, temperatures, and flow rate are collected with a labview program. The labview program collects 100 samples per measurement, and an excel program is used to reduce all the data. The two pressures across the flow meter are averaged, and the resulting pressure is used. Using the ideal gas law, the air density is calculated at the temperature upstream of the flow meter. This density is used to convert the volumetric flow rate reading from acfm (actual cubic foot per minute) to mass flow rate units of Kg/sec. As shown in Eq. (12), knowledge of the Mach number and Mach number gradient is required in order to determine the friction factor. The Mach number is evaluated at 1.2424 cm intervals along the test section at the location of the static pressure probes. Since the stagnation temperature drop between the inlet and exit of the test section is not significant, adiabatic conditions are assumed, and an

average temperature is used. The Mach number gradient is evaluated using the central difference method (i.e. $\frac{M_{i+1} - M_{i-1}}{2\Delta x}$). To eliminate the inlet and exit effects, only six data points in the middle of the test plate are averaged to obtain an averaged value of the friction factor.

A Labview program is set up to acquire the time signal of the pressure oscillations detected by the dynamic pressure probes. The same program performs a Fast Fourier Transform (FFT) to locate and analyze the peaks on the frequency spectra. Finally, frequency spectra of the 8 channels are obtained by plotting the RMS Amplitude vs. Frequency. It should be noted that the frequency response for the HP plate with a hole depth of 1.9 mm could not be obtained because of permanent defects in the plate. The holes for the dynamic pressure sensor locations were larger than specified, which made it impossible for the sensors to be mounted flush with the bottom of the holes. Instead, these holes were sealed off with the use of screws to prevent leakage.

Table 1. List of test conditions used in this study.

Hole Diameter (mm)	Hole Depth (mm)	Clearance (mm)	Surface Configuration
-	-	0.381	Smooth-on-Smooth
3.175	1.9	0.254	Smooth-on-Hole
3.175	1.9	0.381	Smooth-on-Hole
3.175	1.9	0.635	Smooth-on-Hole
3.175	2.6	0.254	Smooth-on-Hole
3.175	2.6	0.381	Smooth-on-Hole
3.175	2.6	0.635	Smooth-on-Hole
3.175	3.302	0.254	Smooth-on-Hole
3.175	3.302	0.381	Smooth-on-Hole
3.175	3.302	0.635	Smooth-on-Hole

RESULTS AND DISCUSSION

This section presents the graphical results of the friction-factor data for the various surface configurations. A total of 37 test cases were conducted, and the conditions are summarized in Table 1. Recall that each test case was conducted with 3 different inlet pressures (84, 70, 55 bars). The results presented are for the combined effects of the friction factor from the smooth as well as the Hole-pattern surfaces. For simplicity, only typical plots are shown in this section, and the remaining plots can be found in the Appendix. Figure 17 shows that the pressure decreases along the length of the test specimen. This result is expected since the air is expanding inside the channel.

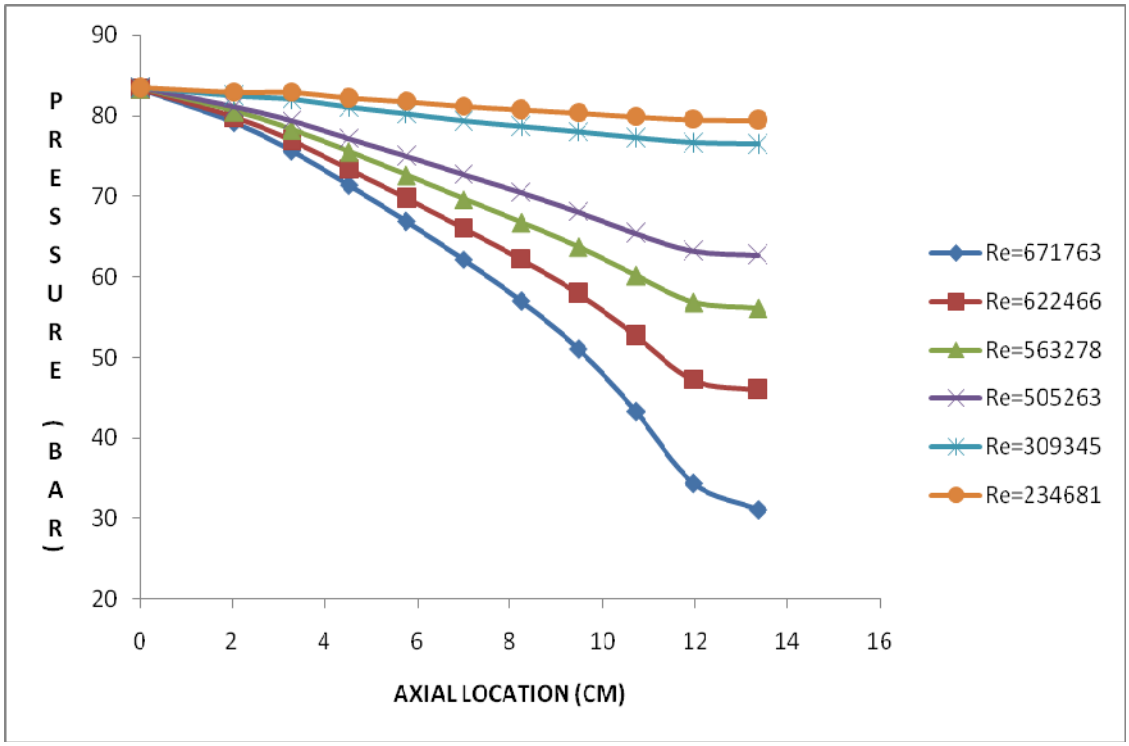

Figure 17. Pressure distribution along the axial location (P_{in}~84 bar, Ø=3.175 mm, d=3.302 mm, and C_p=0.635 mm).

The largest pressure drop occurs for Reynolds number 671,1763 and results in the largest increase in the Mach number as shown in Figure 18. Although the Mach number does not reach unity, the flow at this point chokes at the exit.

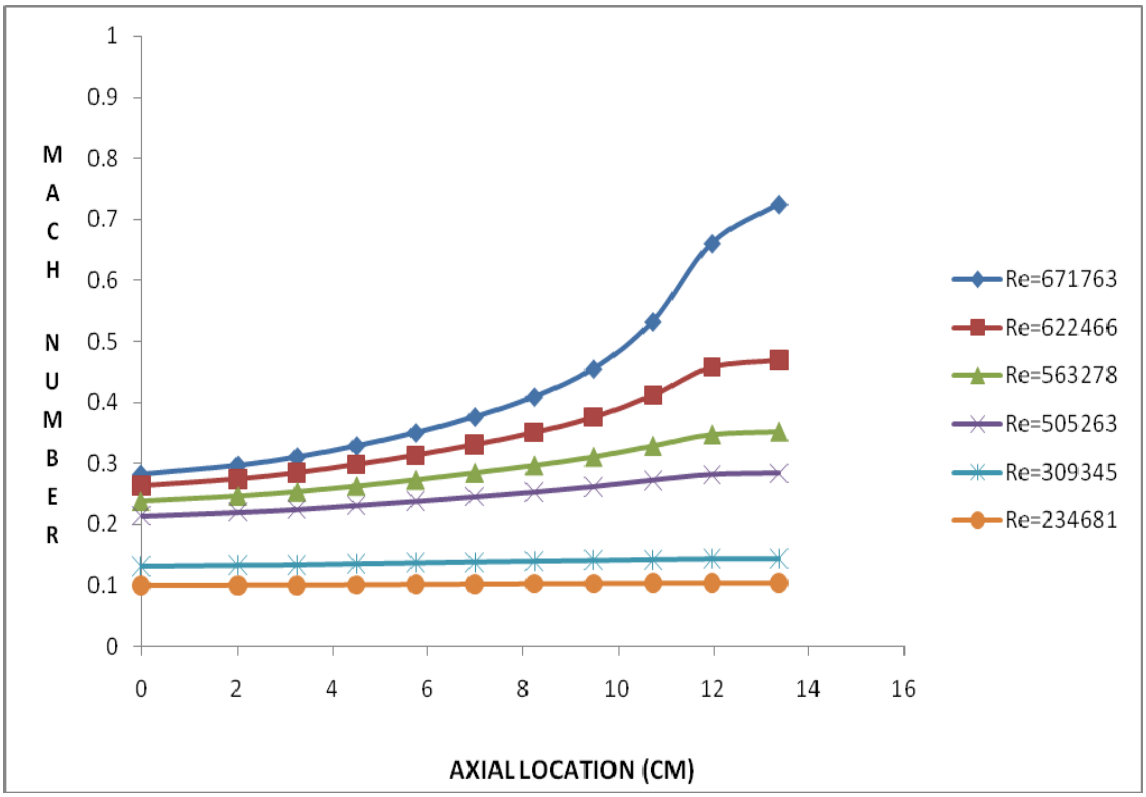

Figure 18. Mach number distribution along the axial location (P_{in}~84 bar, Ø=3.175 mm, d=3.302 mm, C_p=0.635 mm).

Figure 19 represents a typical plot of the variation of the friction factor along the length of the specimen. One would expect that the friction factor remains fairly constant along the length of the specimen. However, due to inlet and exit effects there is a sharp decrease in the friction factor towards the exit. For this reason, only 6 points

in the middle of the specimen were selected and averaged to obtain an averaged friction factor thereby reducing the margin of error.

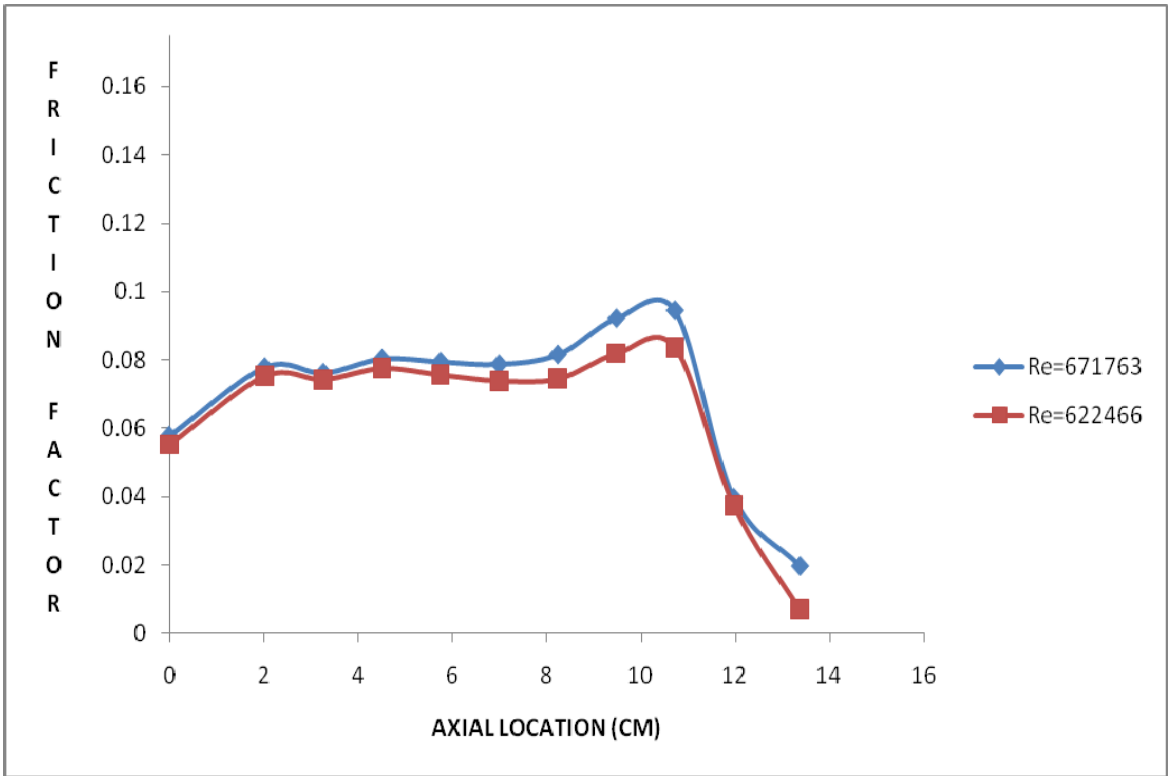

Figure 19. Friction factor distribution along the axial location (P_{in}~84 bar, Ø=3.175 mm, d=3.302 mm, C_p=0.635 mm).

Testing of the HP plates began by testing geometries of hole patterns specified by the sponsoring companies of this project. An abrupt "upset" in the flow was encountered as shown in figure 20. This phenomenon occurred while opening the backpressure valve to establish the pressure ratios in the "forward process". During the

forward process, a sudden reduction in the flow rate occurs as the pressure differential increases. This sudden drop in the flow rate is the result of an increase in the friction factor. Figure 21 shows two distinct friction factors; friction factors from before the upset occurs which are significantly lower than those that occur after the upset. This phenomenon occurred repeatedly and is independent of the surface configurations tested. Forward process tests with smooth-on-smooth configuration produced the same phenomenon (figure 22), leading to the conclusion that the upset phenomenon is not due to the holes. To determine whether this upset phenomenon is occurring inside the test section or due to the malfunction of the flow meter, two different actions were undertaken:

a) Parallel tests were run with a different flow meter, and the results confirmed the accuracy of the original flow meter and the validity of the initial tests.
b) The test section was bypassed and the hydraulic hoses were connected to an orifice flow restrictor. The results indicated that the flow rate increases continuously as the pressure differential increases. In other words, the upset phenomenon was not encountered.

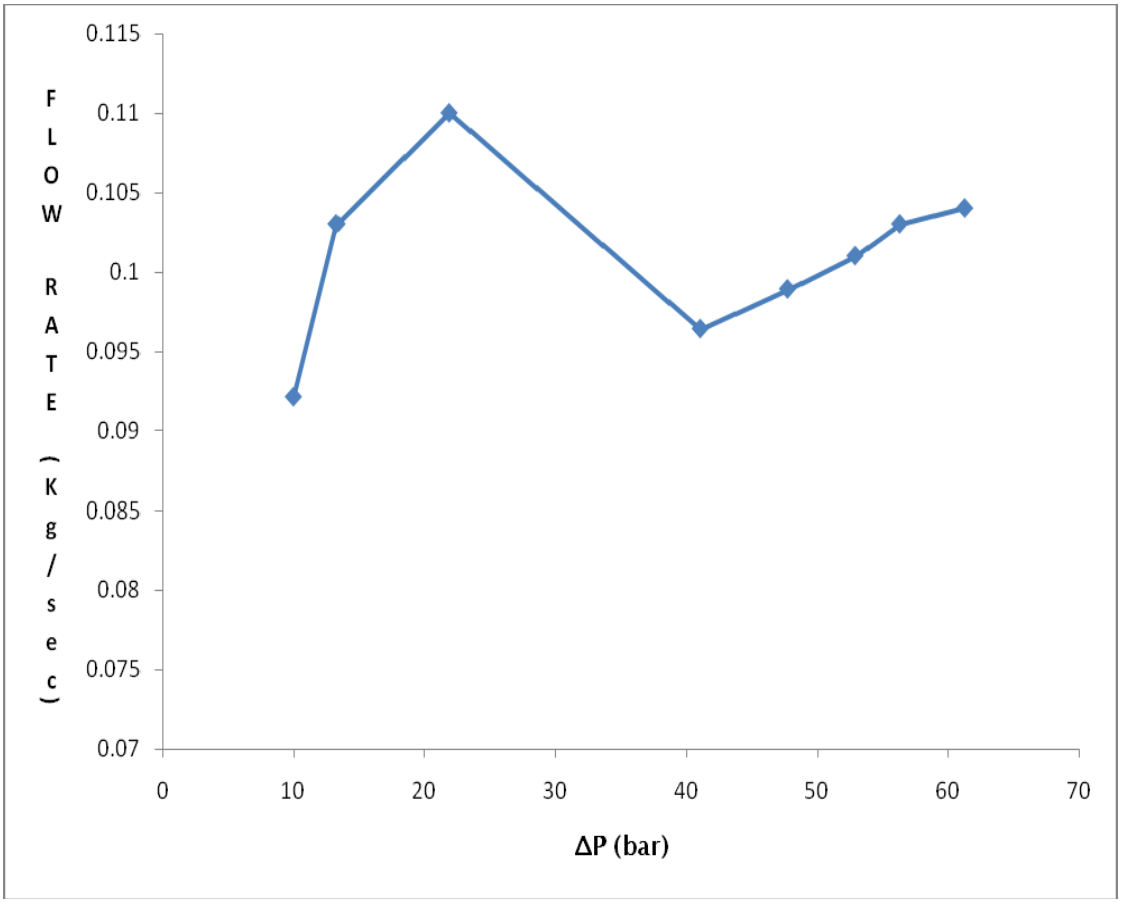

Figure 20. Typical flow rate behavior for the forward process method (P_{in}~84 bar, Ø=3.175 mm, d=3.175 mm, C_p=0.254 mm).

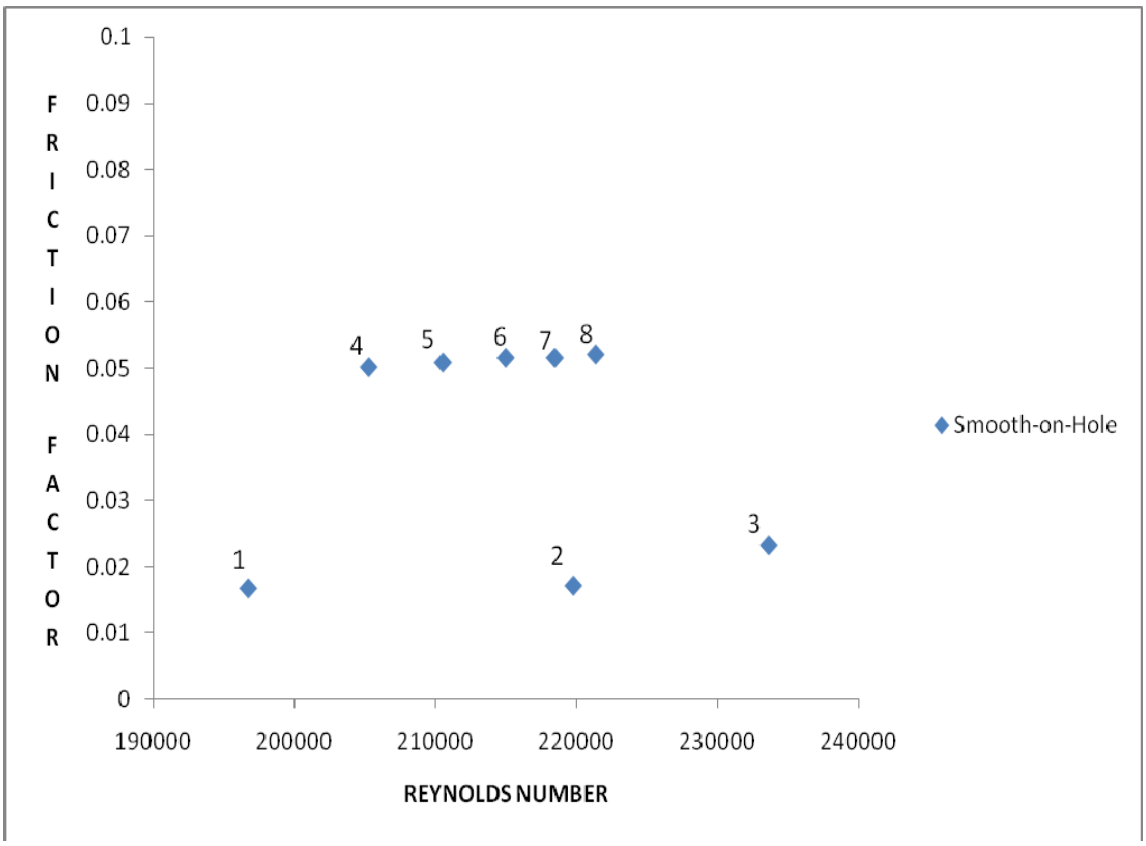

Figure 21. Friction factor upset phenomenon for smooth-on-hole configuration (P_{in}~84 bar, Ø=3.175 mm, d=3.175 mm, C_p=0.254 mm).

.

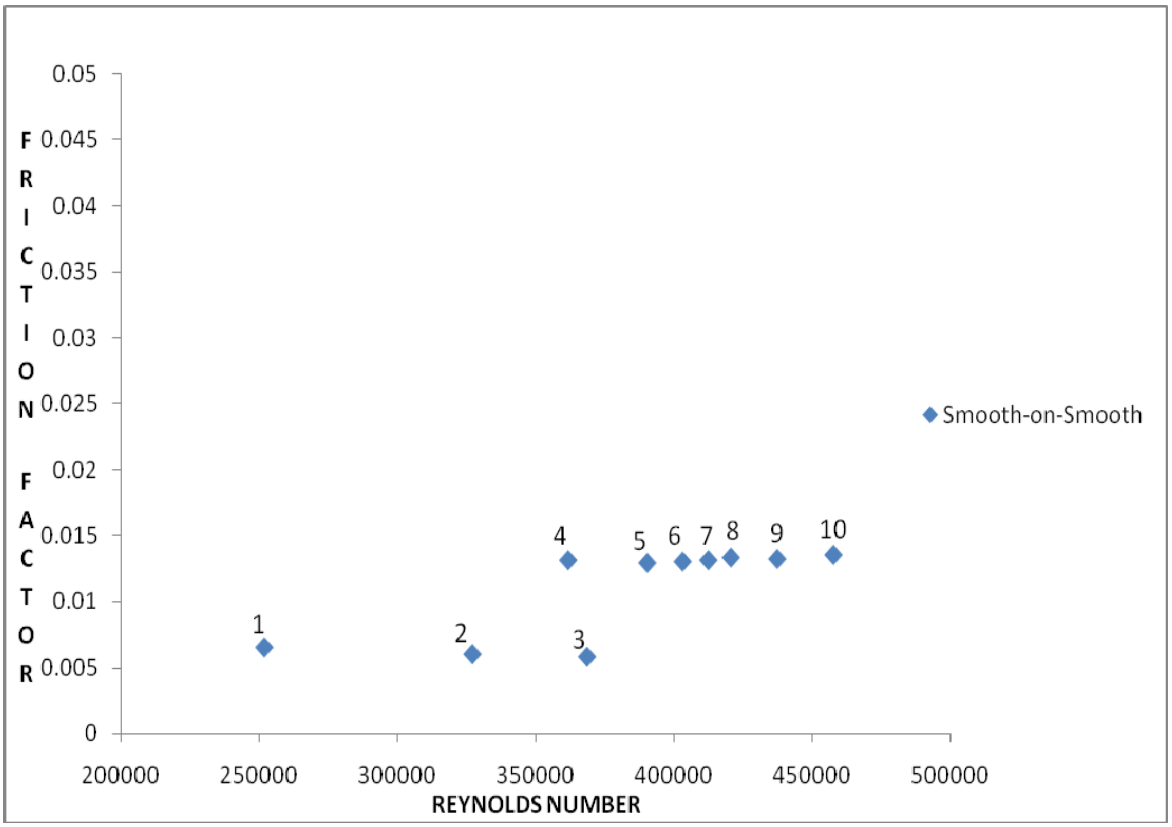

Figure 22. Friction factor upset phenomenon for smooth-on-smooth configuration (P_{in}~84 bar, C_p=0.381 mm).

These tests led to the conclusion that the upset phenomenon is occurring inside the test section. The analysis of Mr. John Fulton, of Exxon Mobil, of the upset phenomenon suggests a choked flow due to friction. This phenomenon is documented by Shapiro [21] as follows: "…any diminutions in the flow are due exclusively to the limiting effects produced by friction." For subsonic flow, "An increase in the value of 4fL/D over its maximum value will act to decrease M_1 until a steady-state solution again becomes possible with $M_2 = 1$. This results in a reduction in the flow rate, i.e. the flow is "choked" by friction." In the previous statement f, L, D, M1 and M2 are the friction factor, length of the duct, diameter of the duct, initial Mach number and final Mach number, respectively. Furthermore, the Fanno parameter (fL_{max}/D) between the inlet and exit of the test section shows that the length of the Hole-pattern (L_p=10 cm) approaches the L_{max} at which choking occurs. This result is illustrated in figure 23. Since the length of the pattern and the diameter (i.e. clearance) are unchanged in this case, the friction factor must change, and it does so from before-upset data to after-upset data as shown in figures 21 and 22. The numbers located above the data points in figures 21 and 22 indicate the order in which the test was conducted. Point 4 in both figures corresponds to the point at which the sudden decrease in flow rate occurs.

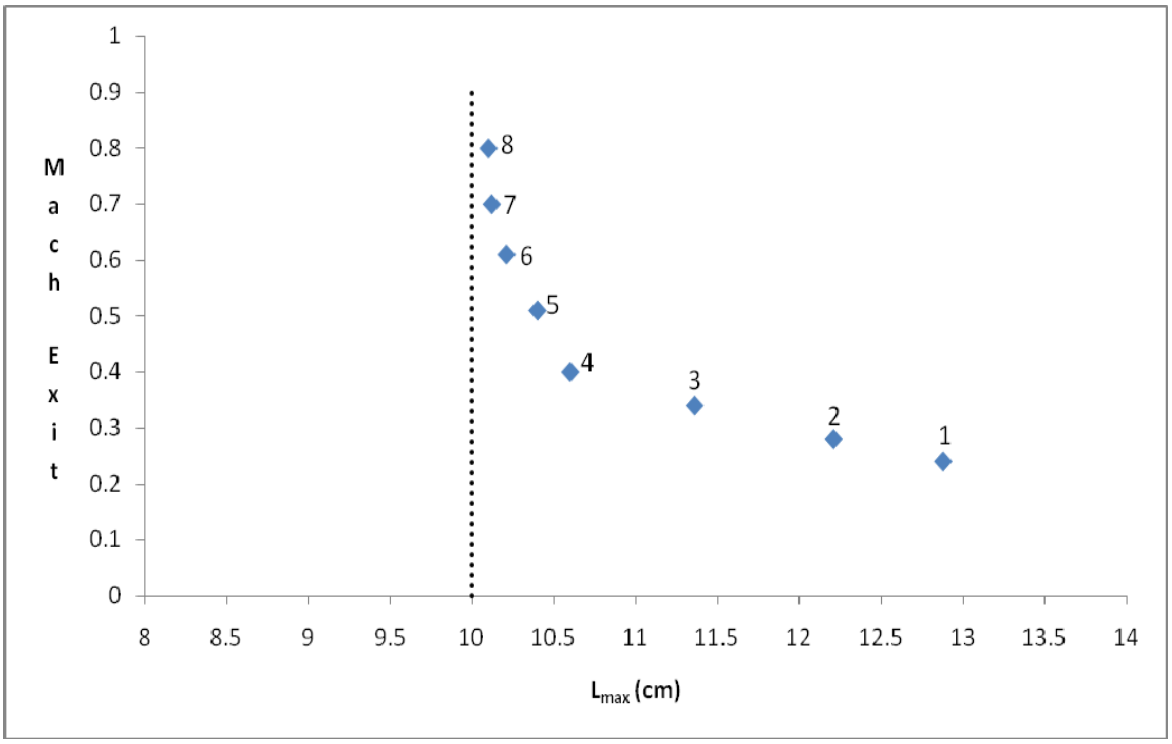

Figure 23. Exit Mach number vs. length at which choking occurs due to friction (P_{in}~84 bar, Ø=3.175 mm, d=3.175 mm, C_p=0.254 mm).

This upset phenomenon, however, was not encountered during the “reverse process”. In The reverse process, the pressure ratios are established by closing the back pressure valve while maintaining the inlet pressure constant. During the reverse process, the mass flow rate is continuously decreasing as the pressure differential decreases as shown in figure 25.

Consequently, the reverse process does not produce a “jump down” behavior in the friction factor (figure 26). In other words, the before-upset data are not reproduced during the reverse process. Instead, the friction-factor data obtained are similar to the after-upset data obtained from the forward process. Recalling that the friction-factor jump observed by Ha and illustrated in figure 24 is a gradual increase in the friction factor as the Reynolds number increases. However, this upset phenomenon is an abrupt increase in the friction factor as opposed to a gradual increase observed by Ha. Therefore, there is a substantial difference between the two phenomena.

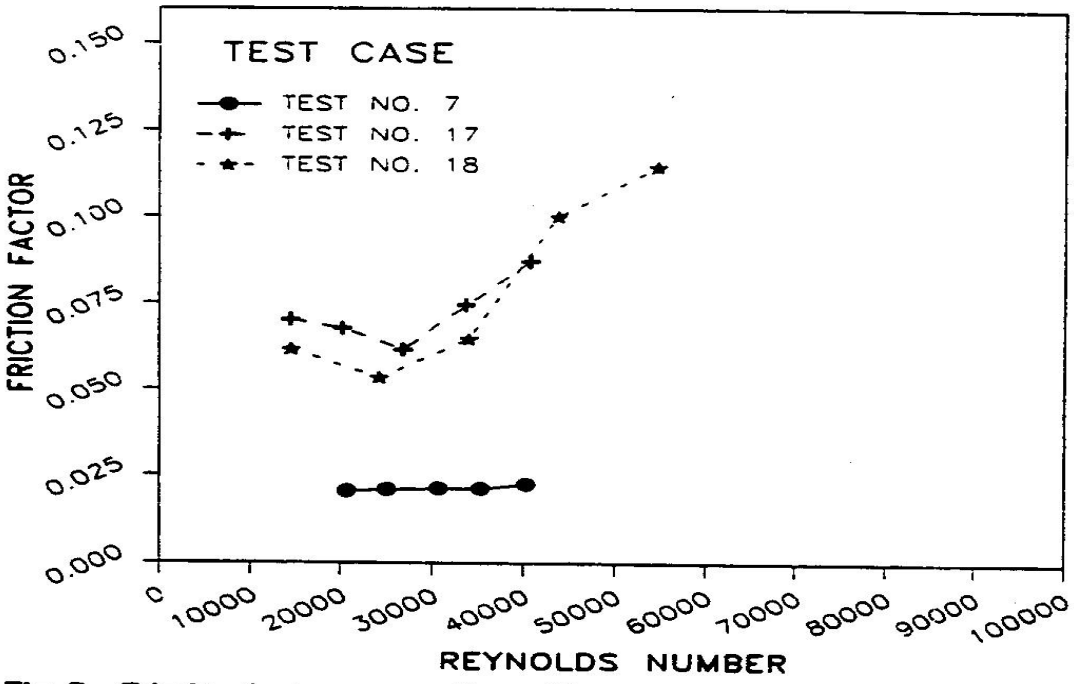

Figure 24. Ha's [11] friction-factor jump phenomenon.

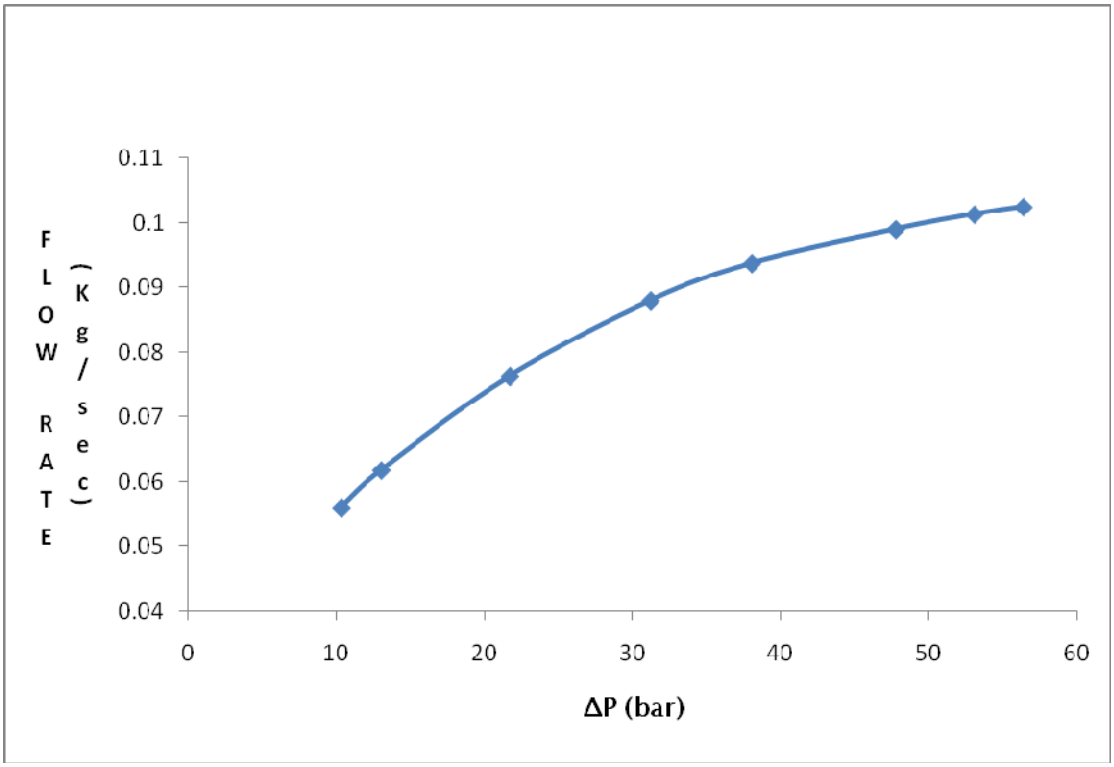

Figure 25. Typical flow rate behavior for the reverse process method (P_{in}~84 bar, Ø=3.175 mm, d=3.175 mm, C_p=0.254 mm).

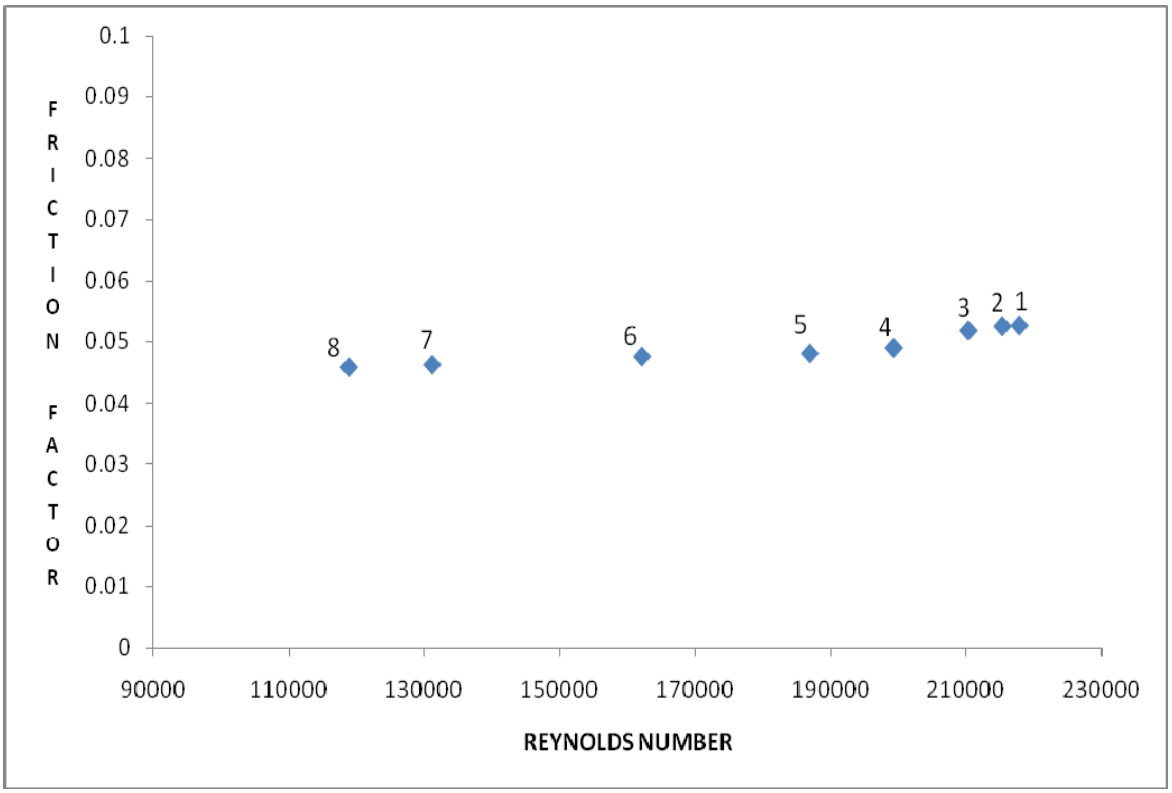

Figure 26. Friction factor vs. Reynolds number for smooth-on-hole configuration for the reverse process method (P_{in}~84 bar, Ø=3.175 mm, d=3.175 mm, C_p=0.254 mm).

Based on the results presented so far and the limited availability of compressed air, the project proceeded with testing of the hole patterns (shown in Table 1) using the reverse process method. Therefore, the results that follow correspond to friction factor data produced by the reverse process and for smooth-on-smooth and smooth-on-hole configurations, unless stated otherwise.

Effect of Inlet Pressure

Tests have been conducted with 3 different inlet pressures (84, 70, and 55 bars) to determine the effect of inlet pressure on the friction factor. In compressible flow, the density and local pressure of the air have a significant effect on the Mach number. As show in Eq. (11), the local pressure term appears in the denominator; therefore, the Mach number and the Mach number gradient decrease as the pressure increases. Figure 27 shows that the friction factor is a modest function of the inlet pressure. Therefore, the friction factor cannot be expressed solely as a function of Reynolds number. However, Ha's results for the non-friction- factor jump cases show that the friction factor decreases as the inlet pressure increases.

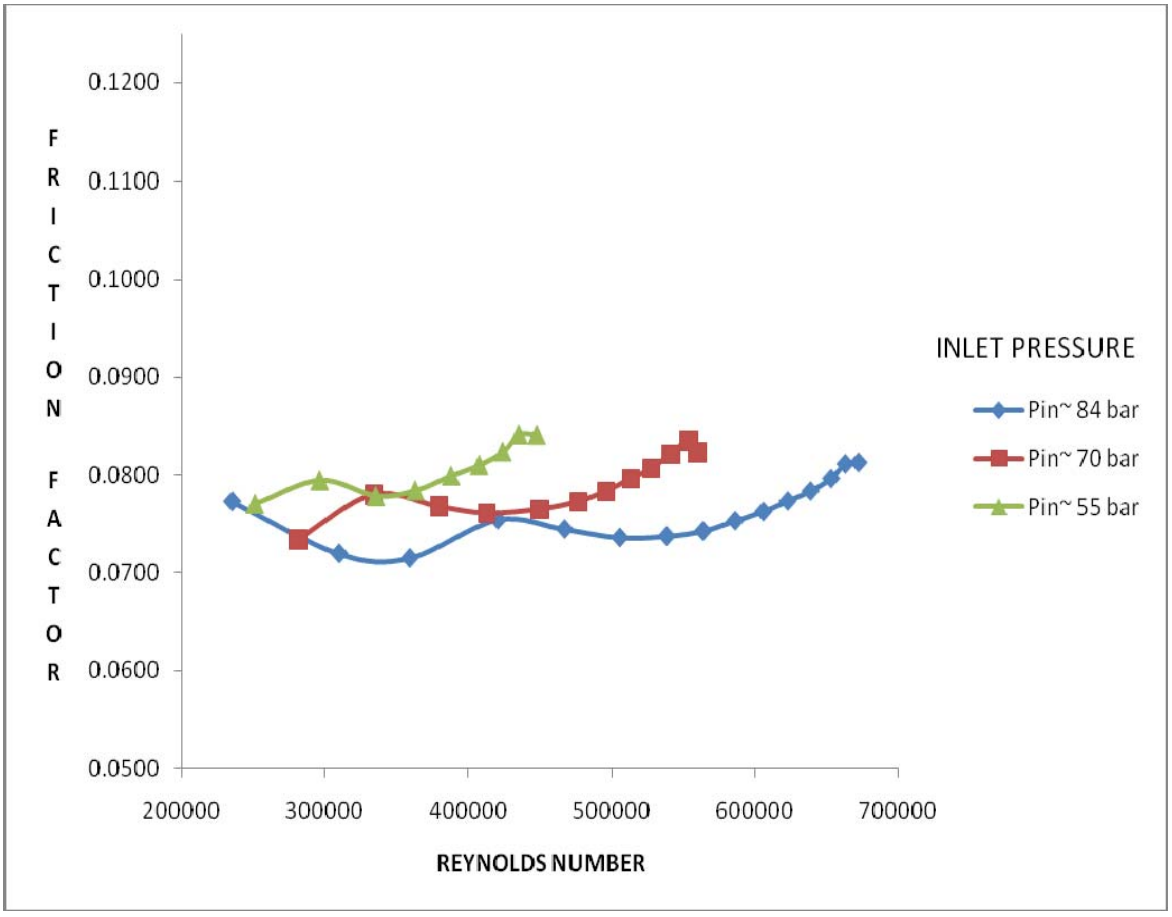

Figure 27. Effect of inlet pressure for smooth-on-hole configuration (Ø=3.175 mm, d=3.302 mm, C_p=0.635 mm).

Effect of Hole Depth

Three HP plates were tested with 3 different hole depths (3.302, 2.6, and 1.9 mm) to determine the effect of hole depth on the friction factor. Figure 28 depicts the typical plot obtained for the friction factor versus Reynolds number for the smooth-on-hole and smooth-on-smooth configurations. As expected, the smooth-on–smooth configuration produces the lowest friction factor data. The 1.9 mm hole depth produces by far the largest friction factor followed by the 3.302 and 2.6 mm. Therefore, the HP plate with a hole depth of 1.9 mm would be expected to leak the least, and the smooth plates leak the most as shown in figure 29. However, based on the results obtained, one cannot conclude whether the friction factor increases or decreases with increasing hole depth. Figure 30 illustrates the plot of the friction factor versus the hole depth for the three clearances tested. Similar results were also reported by Ha in that the friction factor versus the hole depth exhibits an oscillating behavior (figure 31).

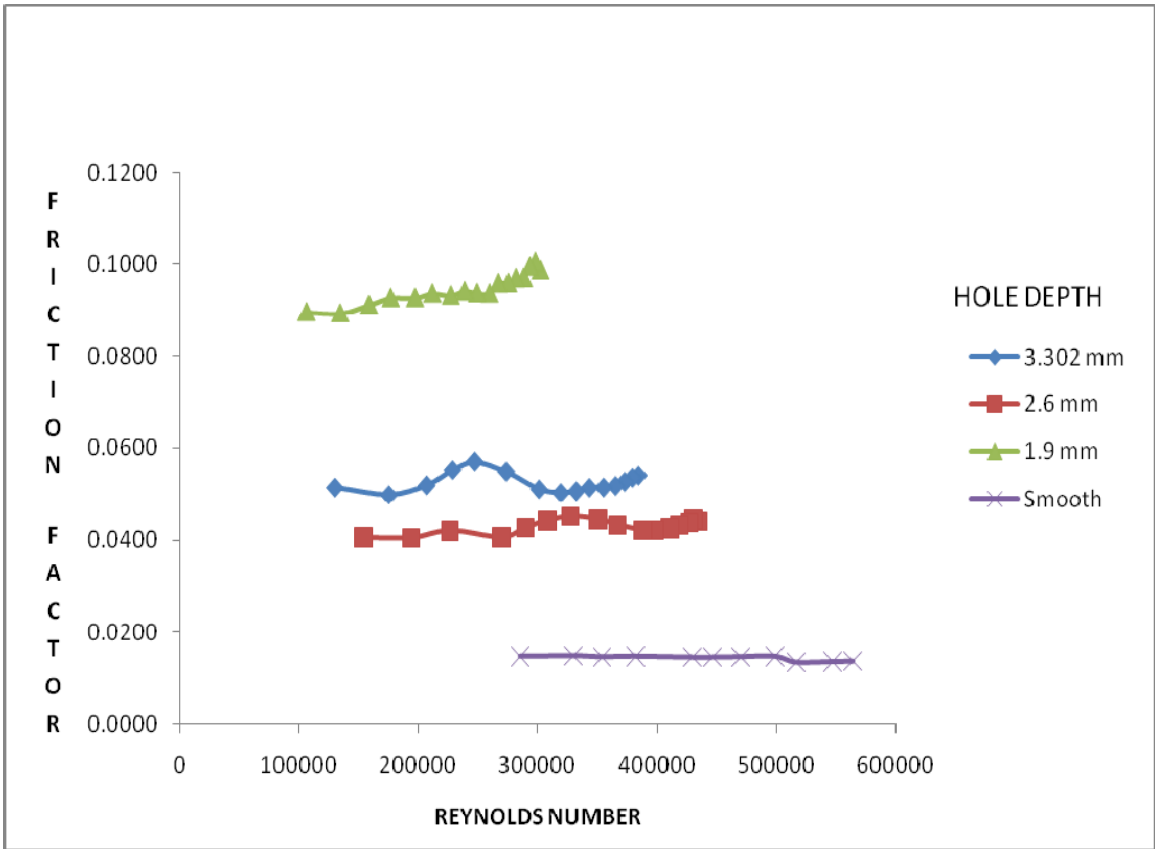

Figure 28. Effect of hole depth for smooth-on-hole configuration (P_{in}~84 bar, Ø=3.175 mm, C_p=0.381 mm).

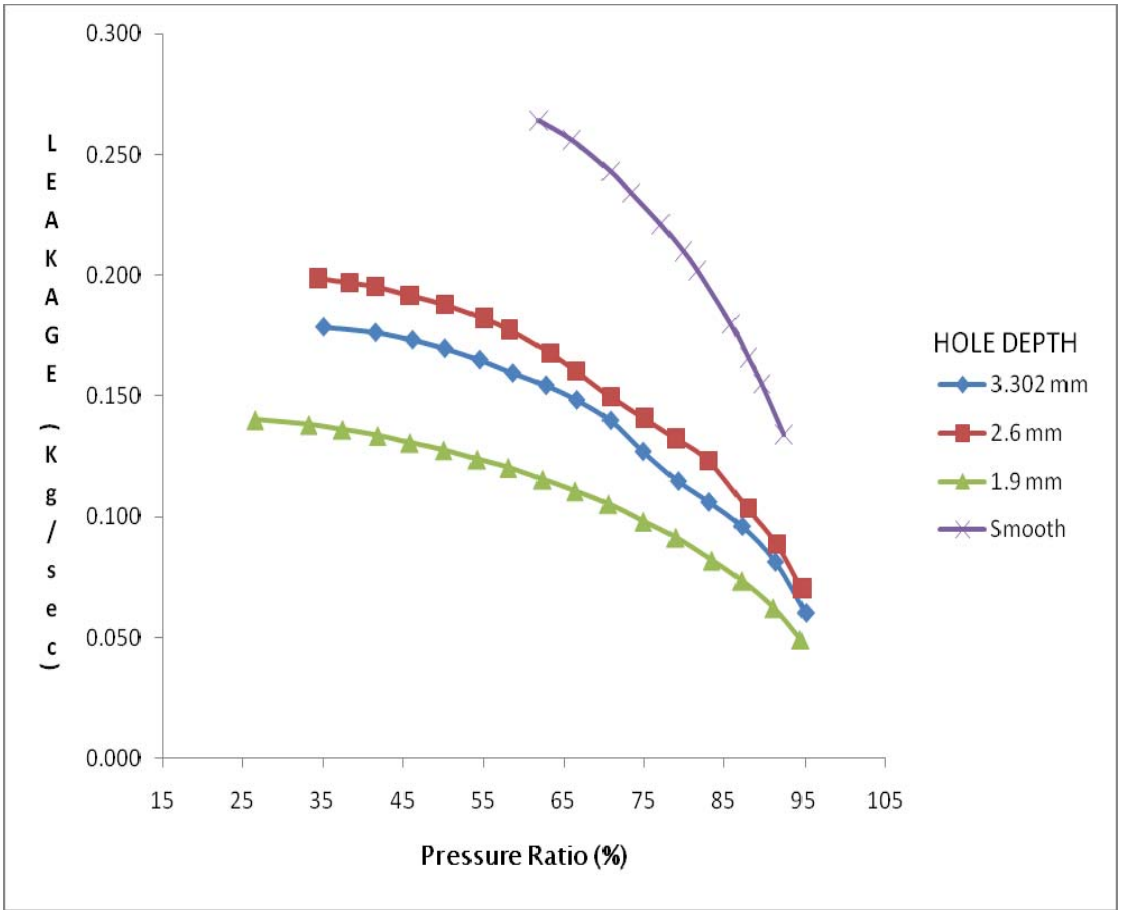

Figure 29. Comparison of leakage performance with cell depth (P_{in}~84 bar, Ø=3.175 mm, C_p=0.381 mm).

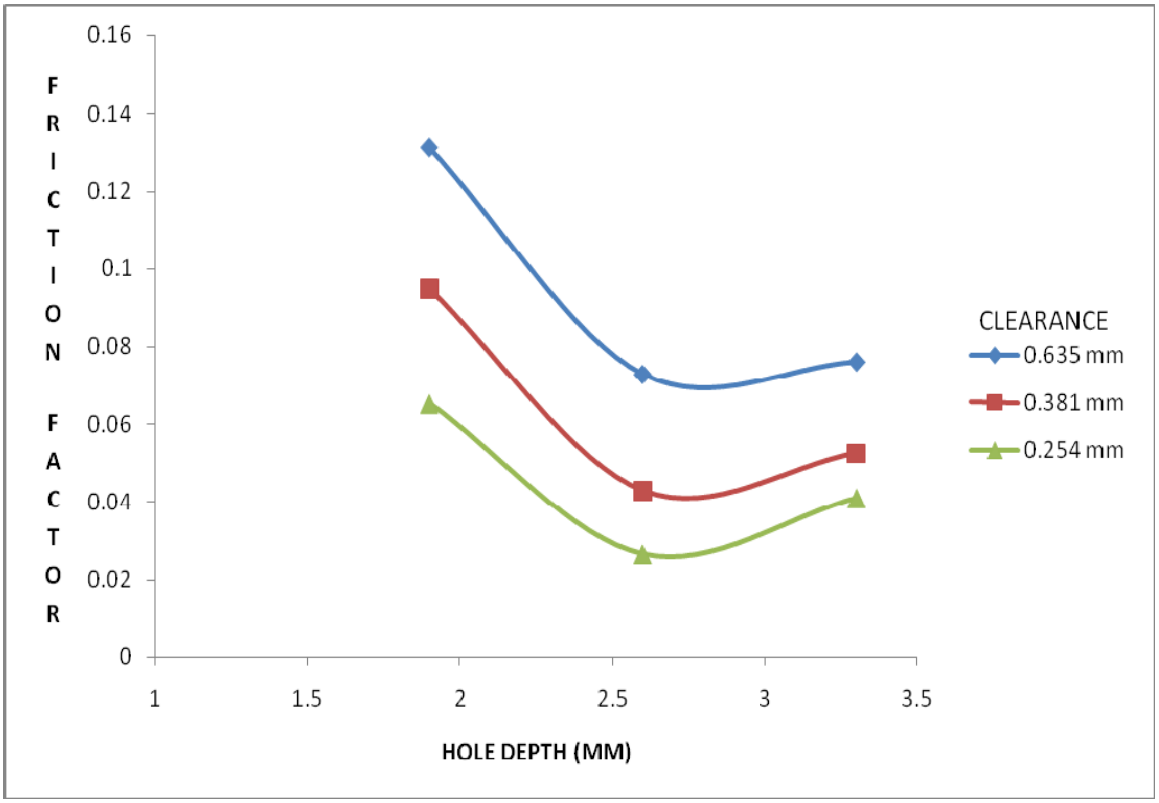

Figure 30. Friction factor vs hole depth for three clearances (P_{in}~84 bar, Ø=3.175 mm).

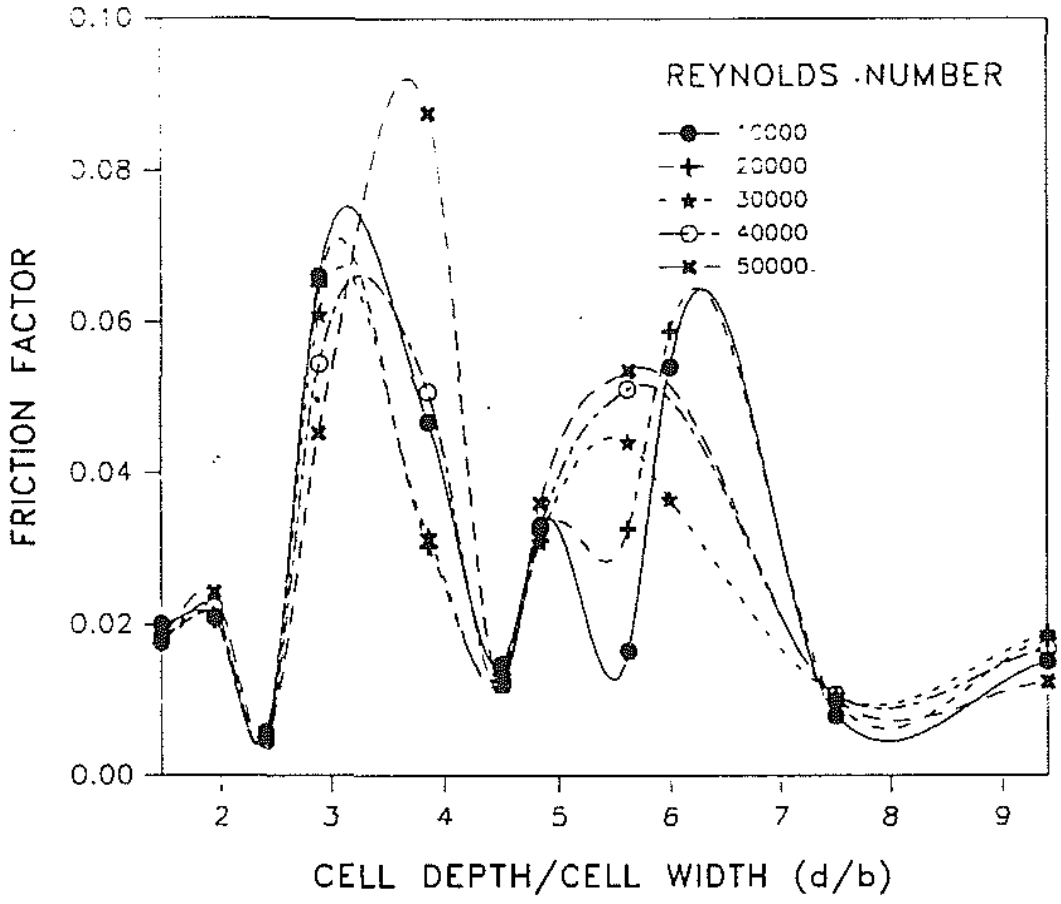

Figure 31. Ha's [11] result for friction factor vs. cell depth to cell width ratio.

Effect of Clearance

Three clearances were tested (0.254, 0.381 and 0.635 mm) to determine the effect of clearance on the friction factor. Previous studies have reported the existence of a plateau where the friction factor ceases to increase with increasing clearance. The results from these experiments show a continuing increase in the friction factor with increasing clearance as shown in figure 32. Moreover, the results of Deotte et al. [16] and Fayolle and Childs [17] also show an observed increase in the friction factor with increasing clearance for liquid damper seals. This result was also observed by Ha for air flow between honeycomb surfaces.

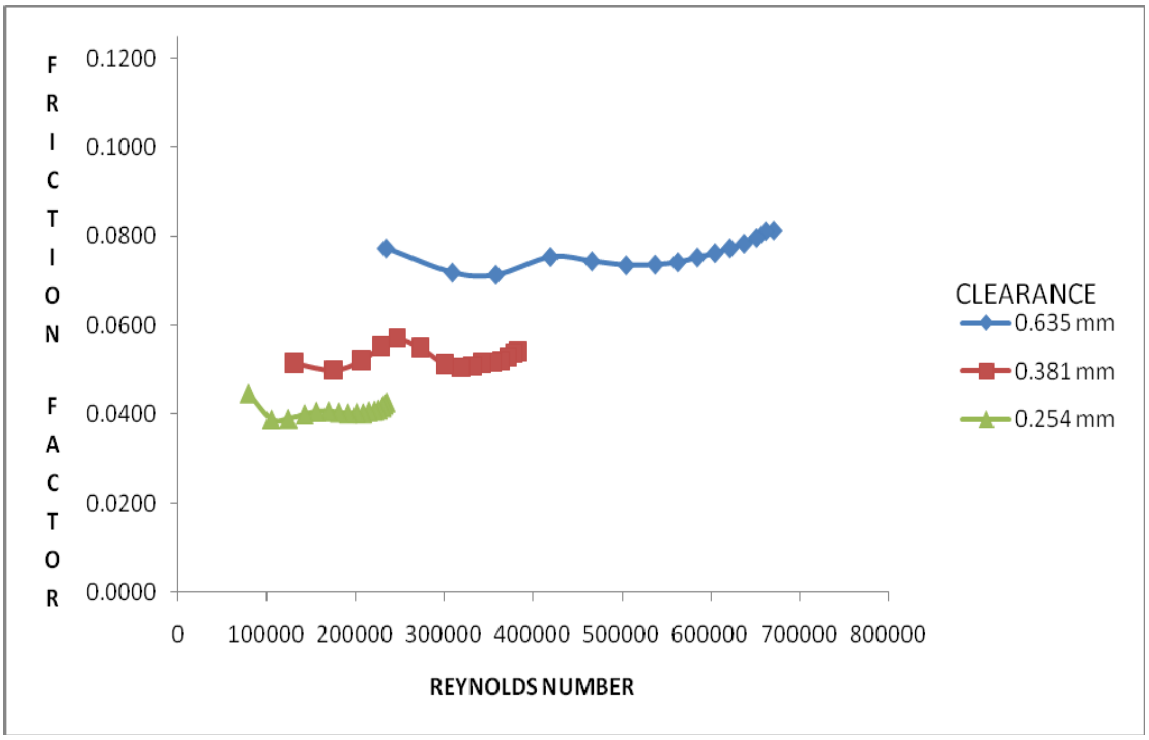

Figure 32. Typical plot for the effect of clearance on the friction factor (P_{in}~84 bar, Ø=3.175 mm, d=3.302 mm).

Effect of Reynolds Number

a) Non-friction factor jump cases

As mentioned earlier, this thesis seeks to examine the friction-factor jump phenomenon reported by Ha. Recalling that Ha observed this phenomenon in 34% of his test cases and for flow between opposed honeycomb surfaces. The results presented so far correspond to air flow between smooth-on-rough and smooth-on-smooth surfaces and have yet to exhibit the friction-factor jump phenomenon. The general trend is that the friction factor remains nearly constant or increases slightly with increasing Reynolds number as shown in figure 33.

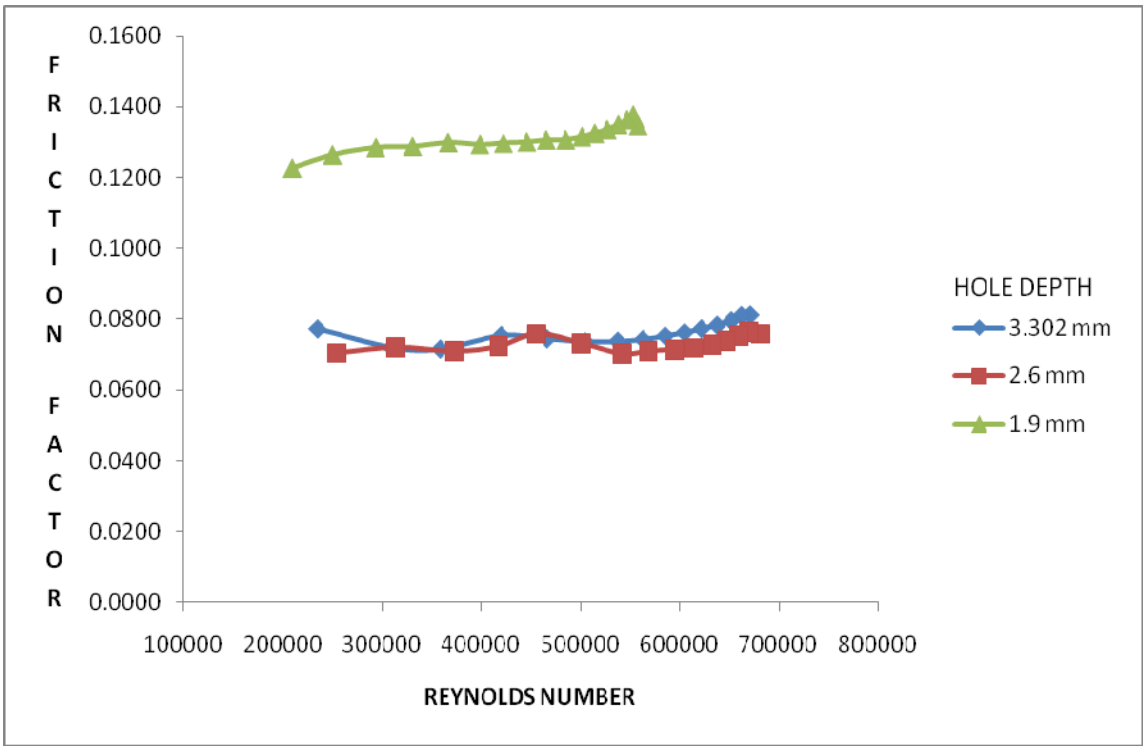

Figure 33. Friction factor vs. Reynolds numbers for non-friction- factor-jump cases (Pin~84 bars, Ø=3.175 mm, Cp=0.635 mm).

To gain insights into the flow over the cavities, Ha instrumented his test specimen with a dynamic pressure sensor. In this study, 4 dynamic pressure sensors were installed on each plate, the time signal was acquired, and the FFT was performed to locate the dominant frequencies. With the assumption that a cavity (i.e. hole) behaves like an open-ended pipe, the Helmholtz frequency can be calculated by using the following formula $f_{res} = \frac{c}{4d}$ [22], where c is the speed of sound and *d* is the hole depth. For hole depths of 2.6 and 3.302 mm, the Helmholtz frequencies are around 32 and 25 KHz, respectively. Figures 34 through 40, show the typical frequency spectra obtained for "non-friction factor jump" cases for hole depths of 3.302 and 2.6 mm. Channels 1, 2, 3 and 4 correspond to dynamic pressure sensor locations on the smooth plate (in the order from inlet to exit) and Channels 5, 6, 7 and 8 correspond to dynamic pressure sensor locations on the HP plate (in the order from inlet to exit). For the smooth-on-smooth configuration, there were no dominant frequencies detected on the frequency spectra. This result is expected due to the absence of the holes. However, for the smooth-on-hole configuration with hole depths of 3.302 mm and 2.6 mm, the frequency spectra reveal dominant frequencies that do not match the theoretical value of the Helmholtz frequency. Unlike the frequency spectra produced by the smooth-on-smooth configuration, dominant frequencies were located on both the smooth and the HP side at the three clearances (0.254, 0.381 and 0.635 mm). For all clearances tested and for different Reynolds numbers, the frequency spectra produced by the dynamic

sensors located on the smooth side are almost identical to those produced by the sensors located on the bottom of the cavity. However, the amplitude of these frequencies is always higher on the HP side. Moreover, there appears to be a slight increase in the dominant frequency from inlet to exit. A possible explanation is that the Mach number increases from inlet to exit which leads to a slight increase in the dominant frequency. The frequency spectra obtained vary with the clearance. Strong oscillations occur for the 0.635 mm clearance. These oscillations get weaker as the clearance decreases and sometimes suppressed for the smallest clearance tested (0.254 mm). From the frequency spectra for the non-friction-factor jump cases, the dominant frequencies deviate from the Helmholtz frequency and do not have any visible effect on the friction factor. Therefore, the absence of the Helmholtz frequency would seem to be a characteristic of the non-friction-factor jump cases.

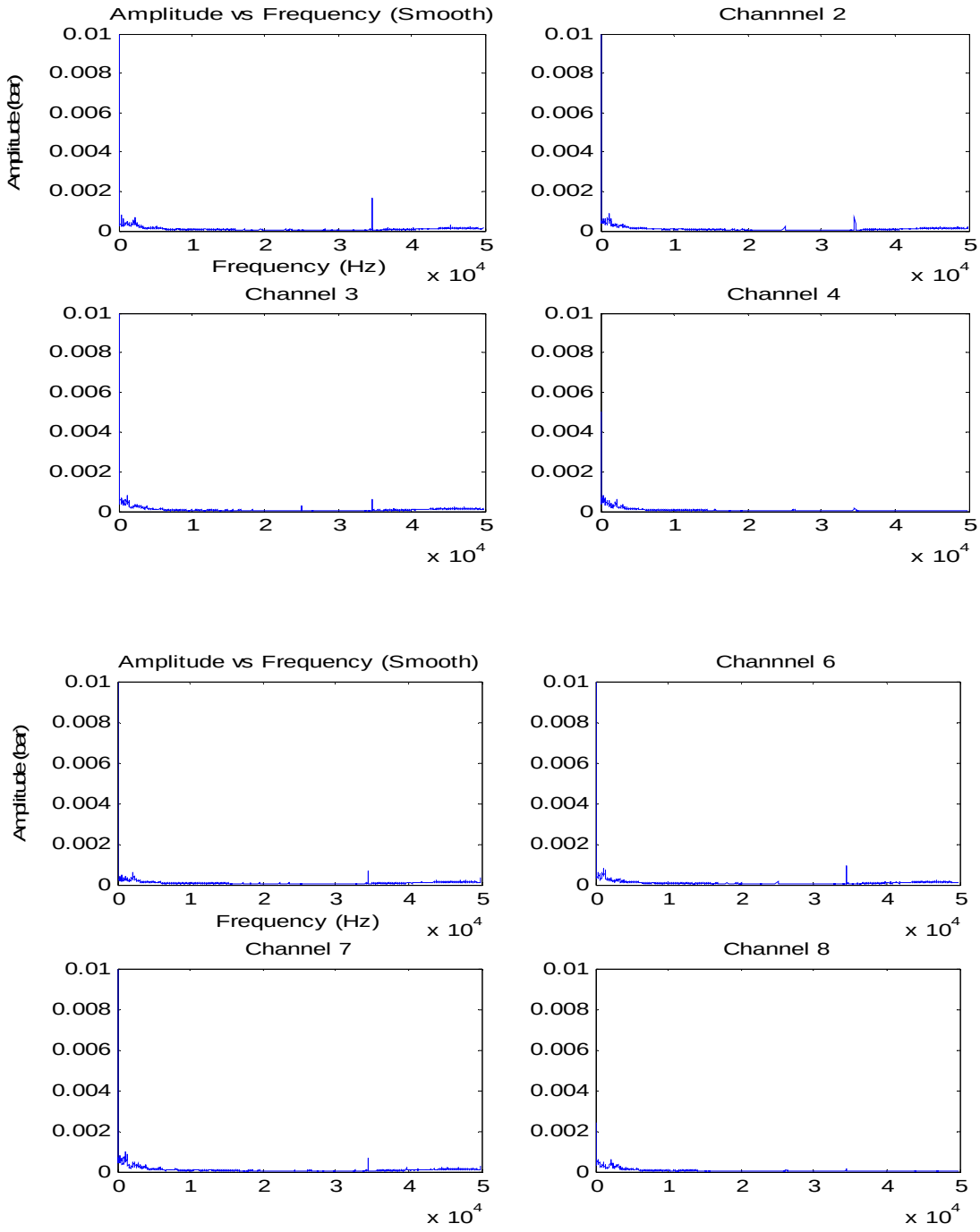

Figure 34. Frequency spectra for smooth-on-smooth configuration (C_p=0.381 mm, P_{in}= 84 bar).

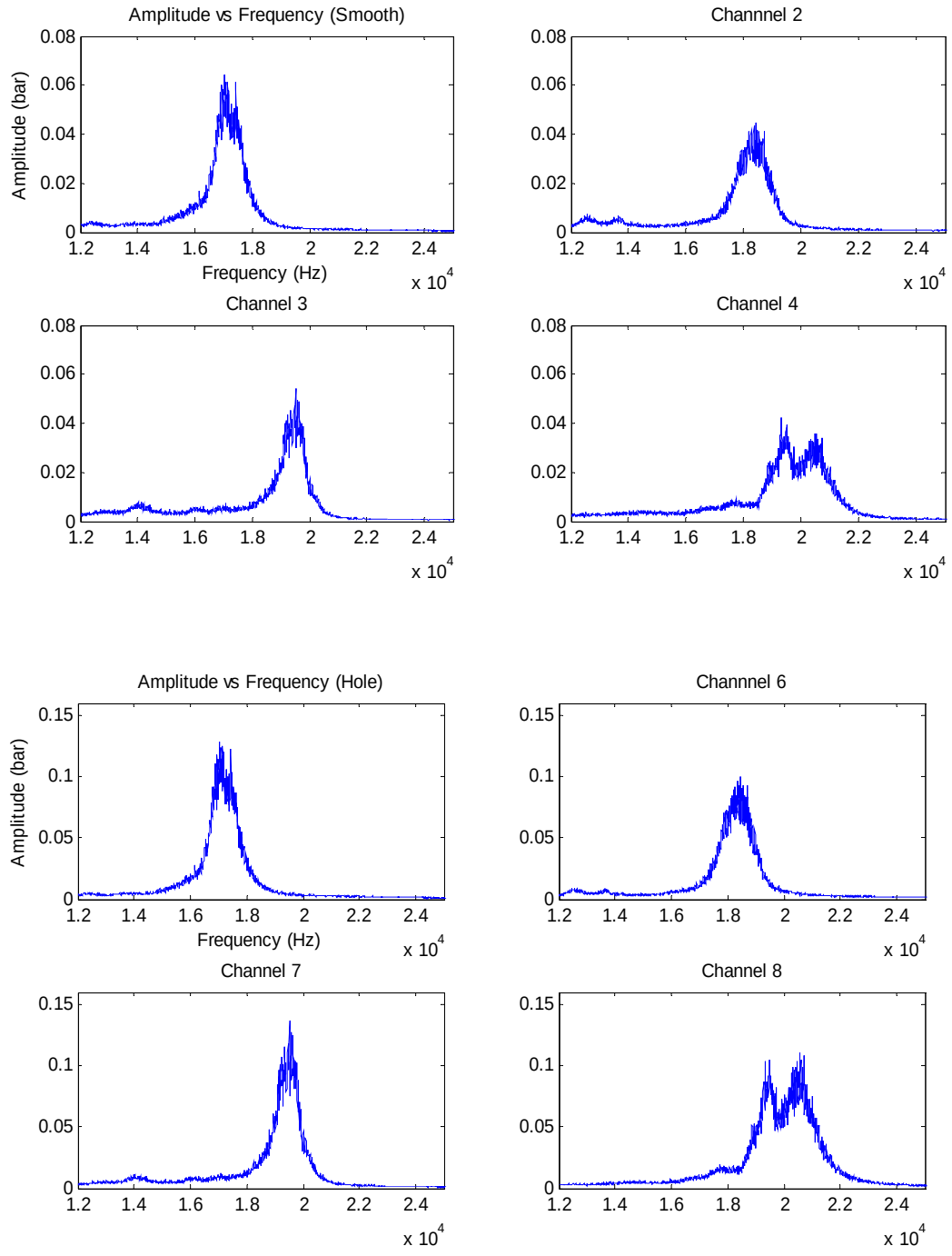

Figure 35. Frequency spectra for smooth-on-hole configuration (d=3.302 mm, C_p=0.635 mm P_{in}=84 bar).

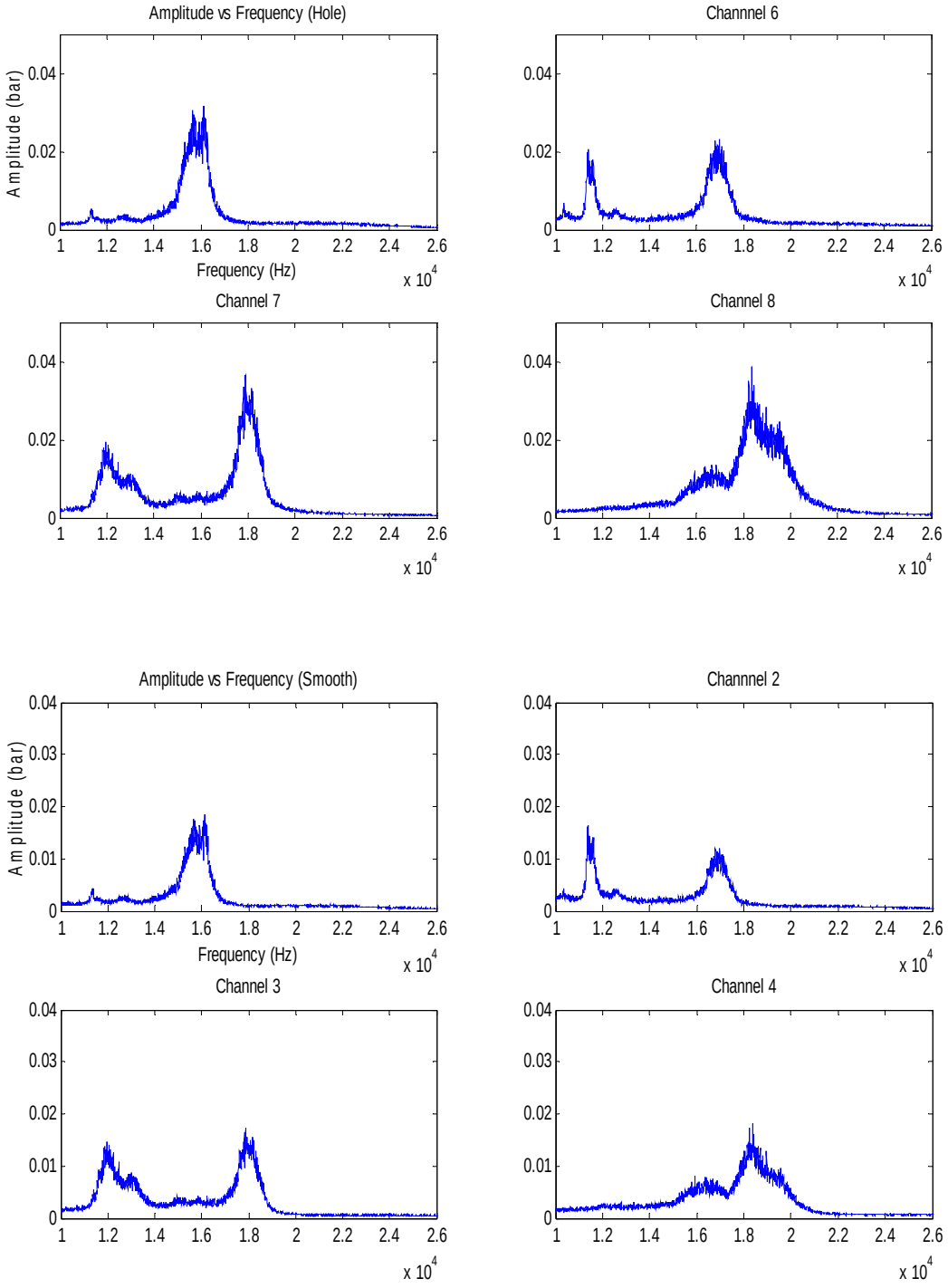

Figure 36. Frequency spectra for smooth-on-hole configuration (d=3.302 mm, C_p=0.381 mm, P_{in}=84 bar).

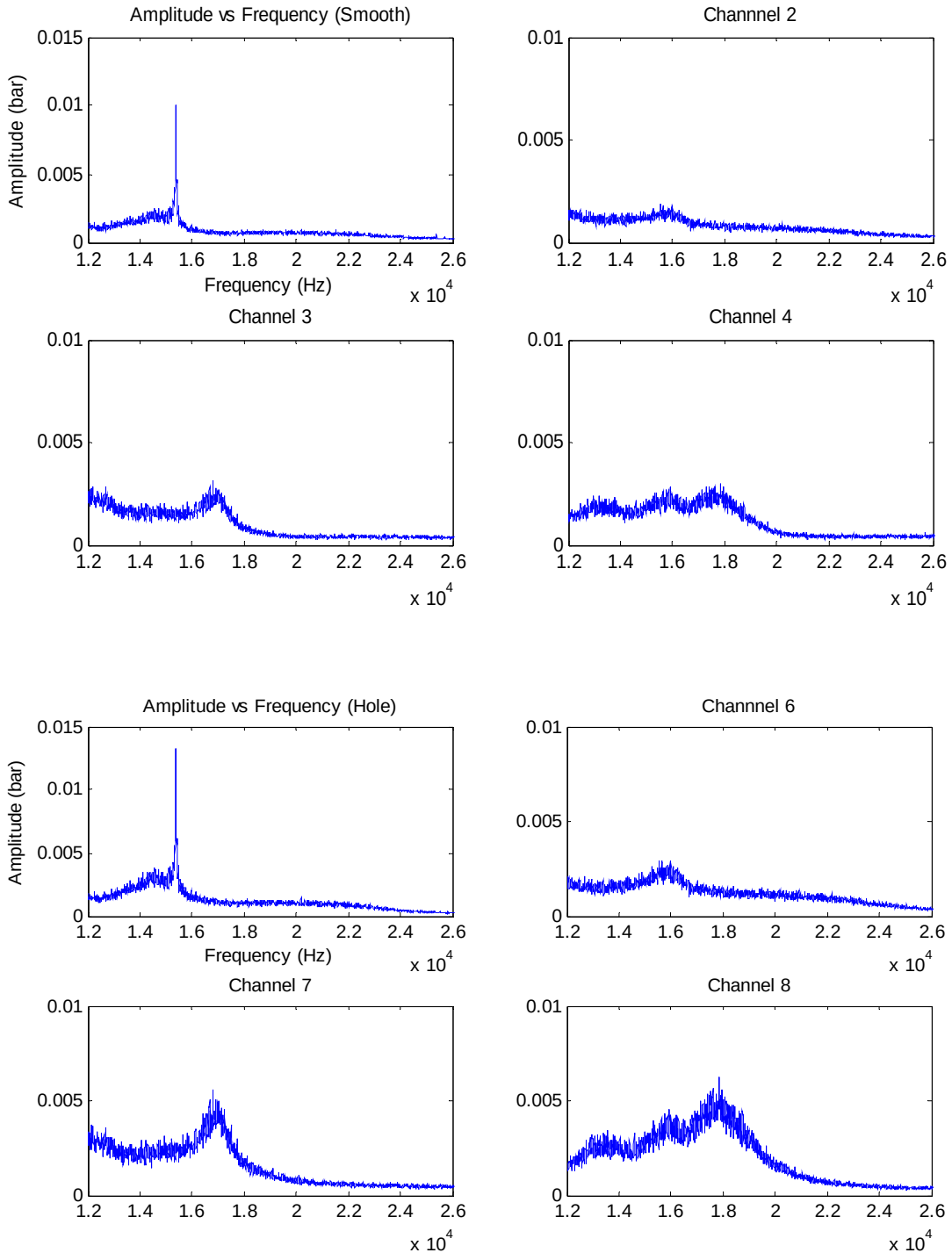

Figure 37. Frequency spectra for smooth-on-hole configuration (d=3.302 mm, C_p=0.254 mm, P_{in}=84 bar).

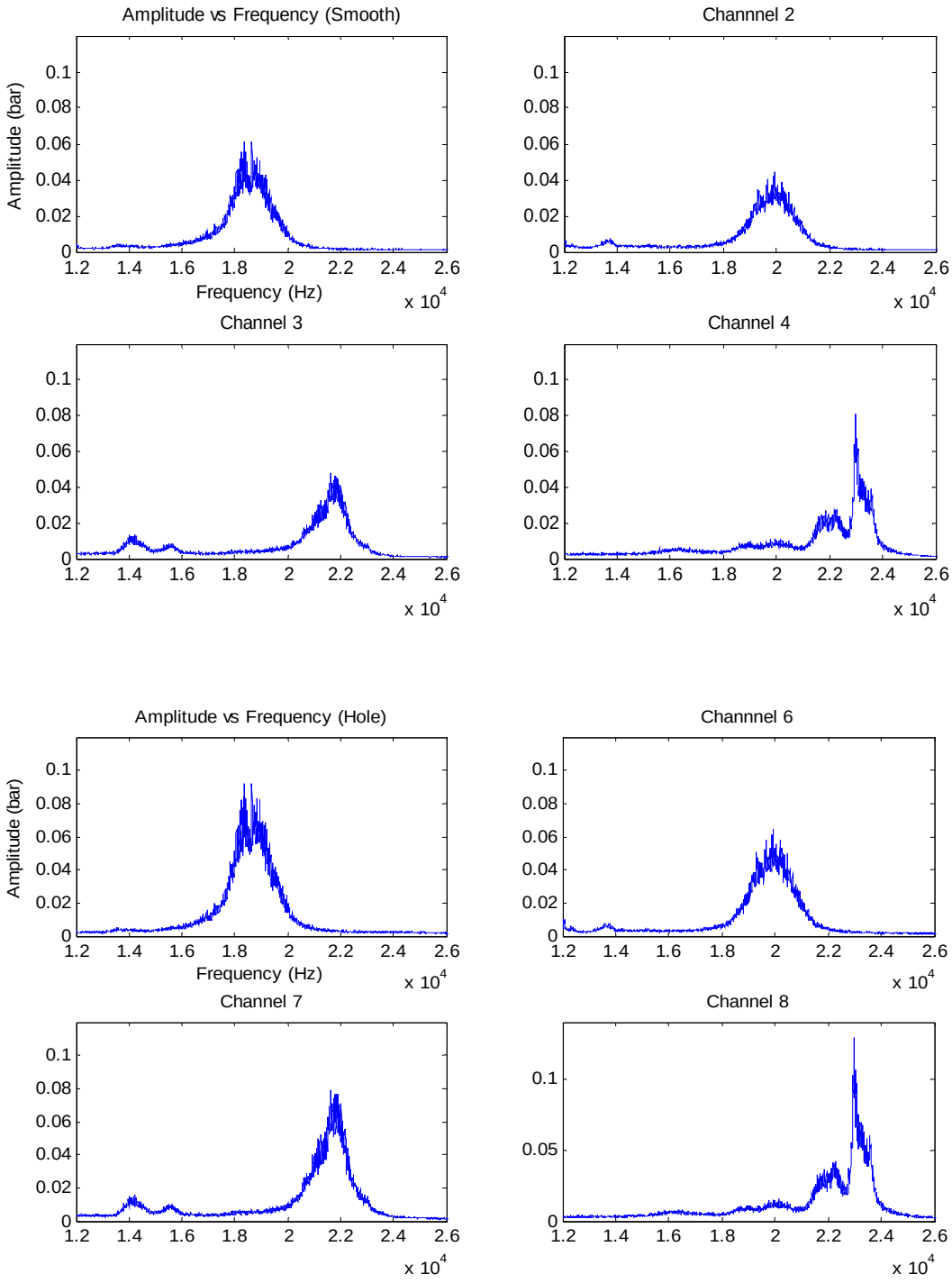

Figure 38. Frequency spectra for smooth-on-hole configuration (d=2.6 mm, C_p=0.635 mm, P_{in}=84 bar).

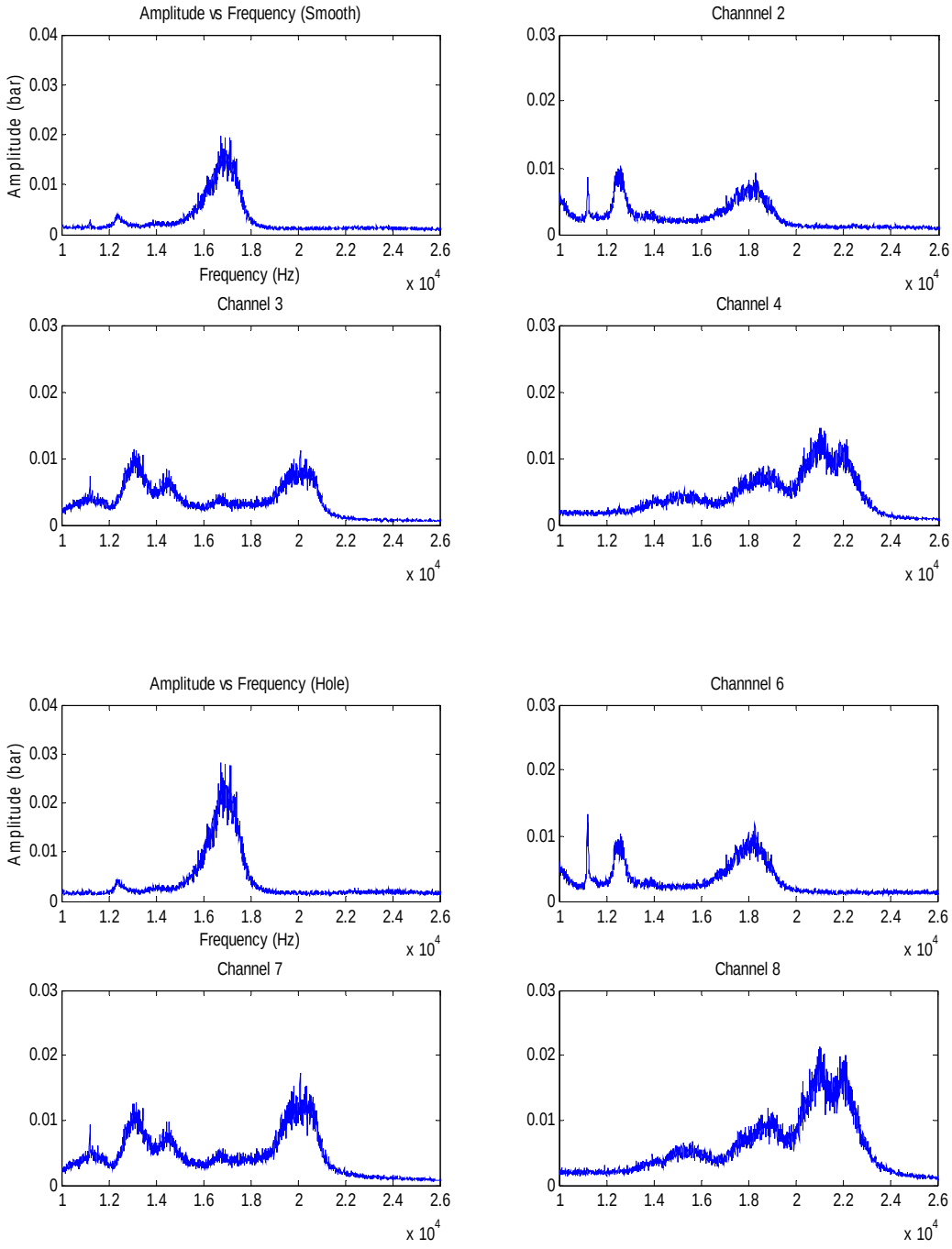

Figure 39. Frequency spectra for smooth-on-hole configuration (d=2.6 mm, C_p=0.381 mm, P_{in}=84 bar).

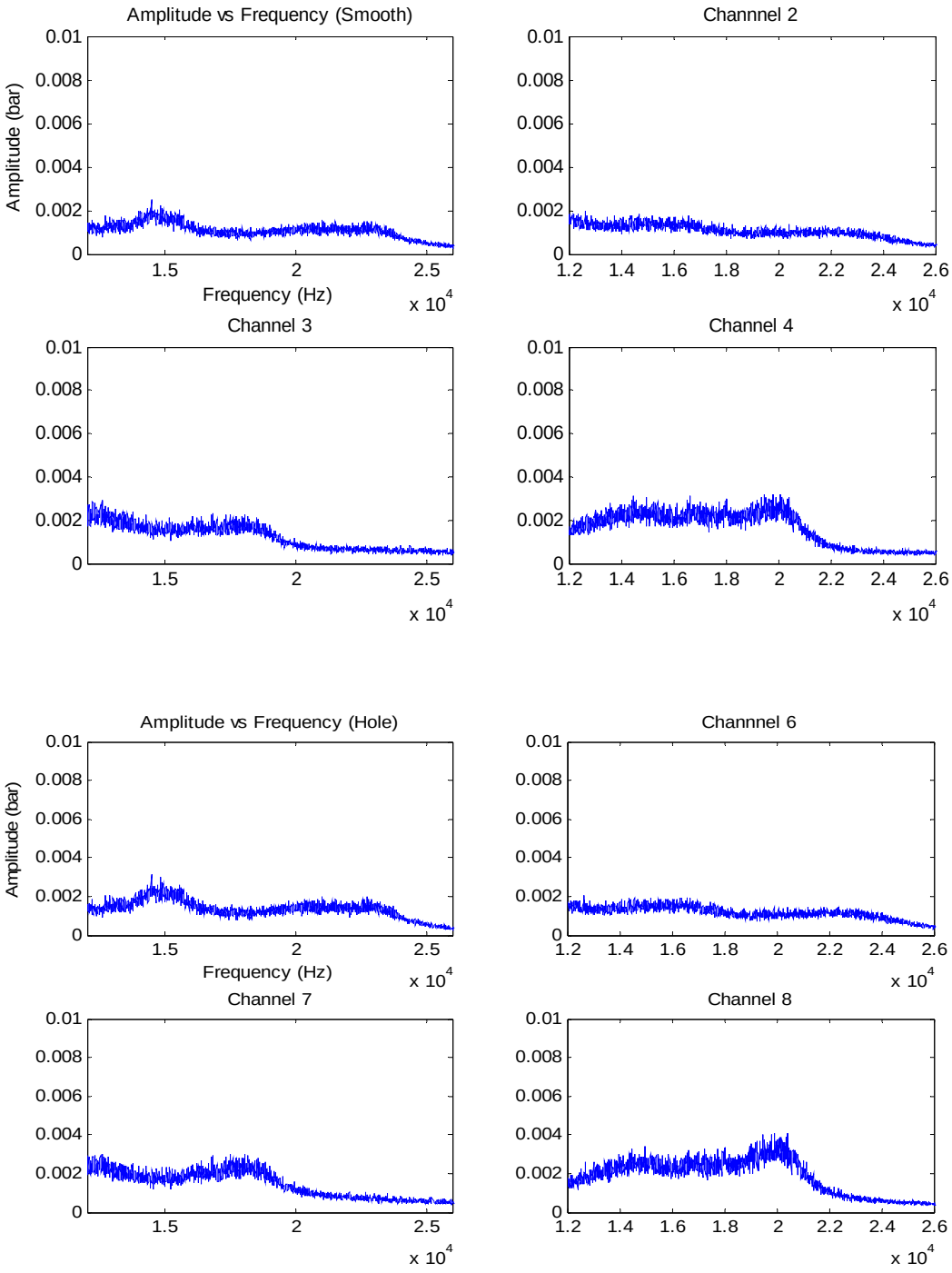

Figure 40. Frequency spectra for smooth-on-hole configuration (d=2.6 mm, C_p=0.254mm, P_{in}=84 bar).

b) Friction-factor jump cases

The friction-factor jump phenomenon was not observed in the smooth-on-hole configuration. In an attempt to validate Ha's results of opposed roughened surfaces, tests have been conducted with a hole-on-hole configuration. The Hole-pattern as well as the hole depth are almost identical for both test specimens. The HP plates are also instrumented with dynamic pressure sensors located flush with the bottom of the holes. The order of the channels is similar to that of the smooth-on-hole configurations. Figures 41 through 43 show the graphical results for the behavior of the friction factor for the three clearances and three inlet pressures. The results stemming from the hole-on-hole configuration exhibit the friction-factor jump phenomenon. There is a significant increase in the friction factor with increasing Reynolds numbers. For an inlet pressure of 84 bar and a clearance of 0.635 mm the friction factor increases from a value of 0.1 to a value of 0.136, almost a 36% increase. Also, similar to the non-friction factor jump cases, the friction factor increases with increasing clearance. Calculation of the Helmholtz acoustic frequency for a hole depth of 3.302 mm yields a value of around 25.6 KHz. Interestingly enough, the frequency spectra (shown in figures 44 through 47) obtained from the friction-factor jump cases reveal a Helmholtz frequency that matches the theoretical value of 25.6 KHz. However, the harmonics of the fundamental frequency were not detected on the frequency spectra due to the inability of the dynamic data acquisition board to detect frequencies higher than 50 KHz. The friction-factor jump is attributed to the presence of the normal mode resonance which is

associated with the large scale coherent structure in the flow. The magnitude of the Helmholtz frequency is sufficient enough to interfere with the main flow and results in an increase in flow resistance which translates into an increase in the friction factor. However, in the 0.635 mm case, there exist a fall-off in the friction factor as the Reynolds number continues to increase, which suggests that the cavity-flow phenomena is detuning. Figure 44 corresponds to the point at which the friction factor reaches a maximum value at a Reynolds number of 478962. Past this point, the magnitude of the Helmholtz frequency decreases as the Reynolds number increases as illustrated in figure 45. This decrease in the magnitude is associated with the fall-off in the friction factor. Ha's friction-factor jump, however, does not exhibit this fall-off behavior at the high end. Based on the results obtained, the presence of the Helmholtz frequency would seem to be a characteristic of the friction-factor jump phenomenon.

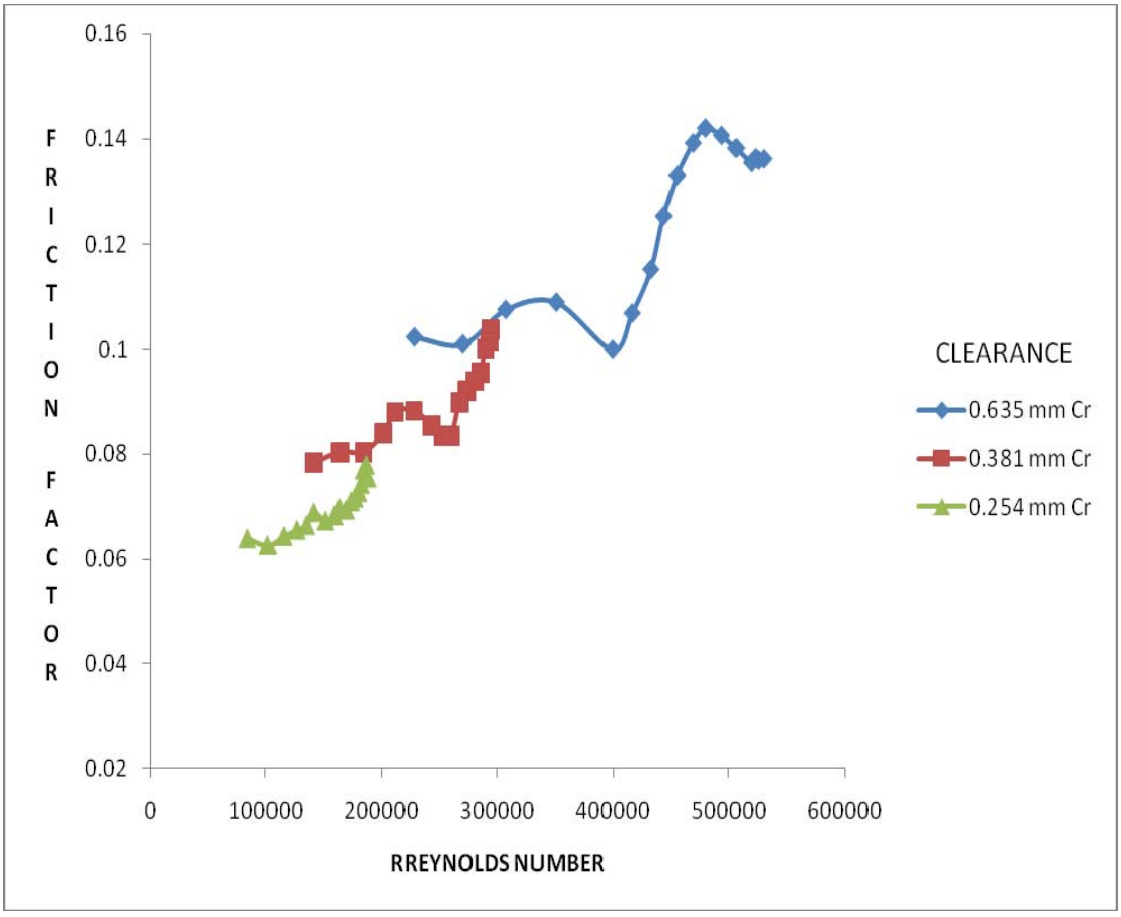

Figure 41. Friction factor vs. Reynolds number for hole-on-hole configuration (P_{in}~84 bars, Ø=3.175 mm, d=3.302 mm).

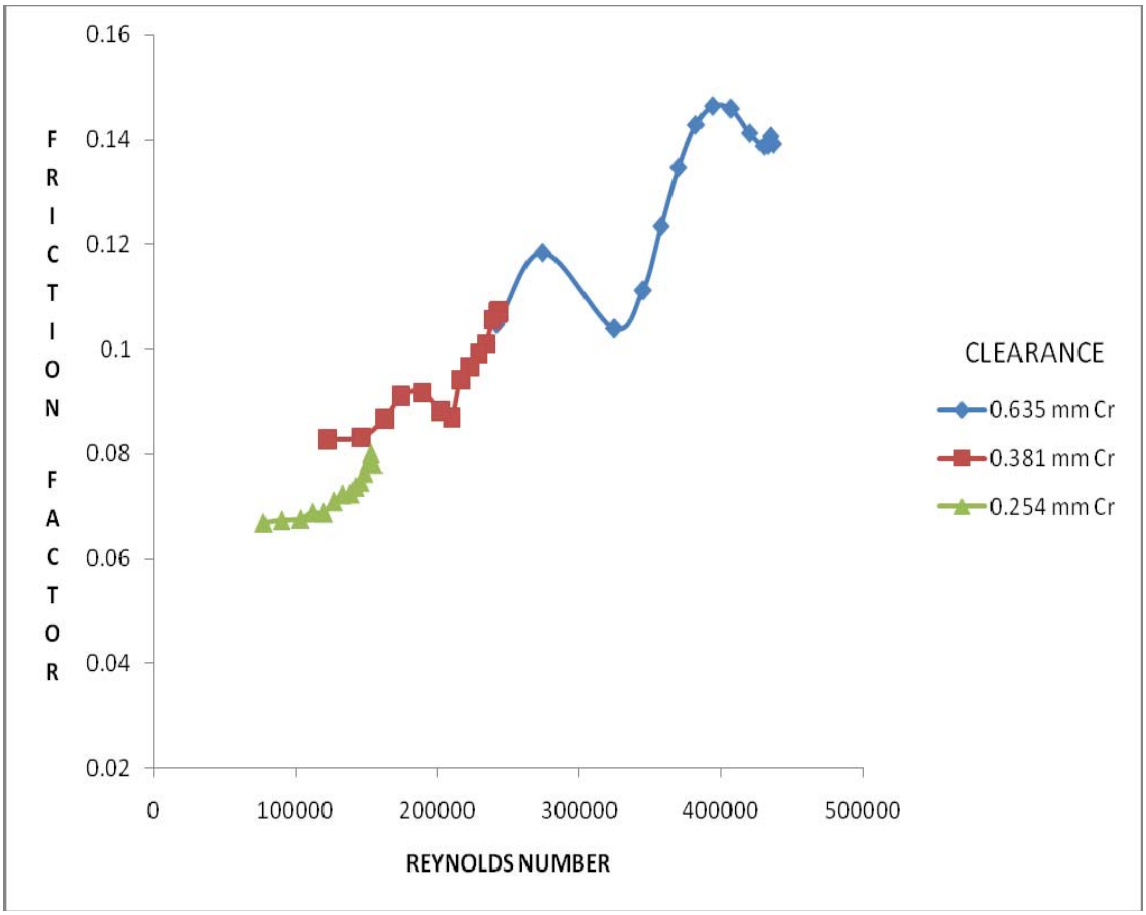

Figure 42. Friction factor vs. Reynolds number for hole-on-hole configuration (P_{in}~70 bars, Ø=3.175 mm, d=3.302 mm).

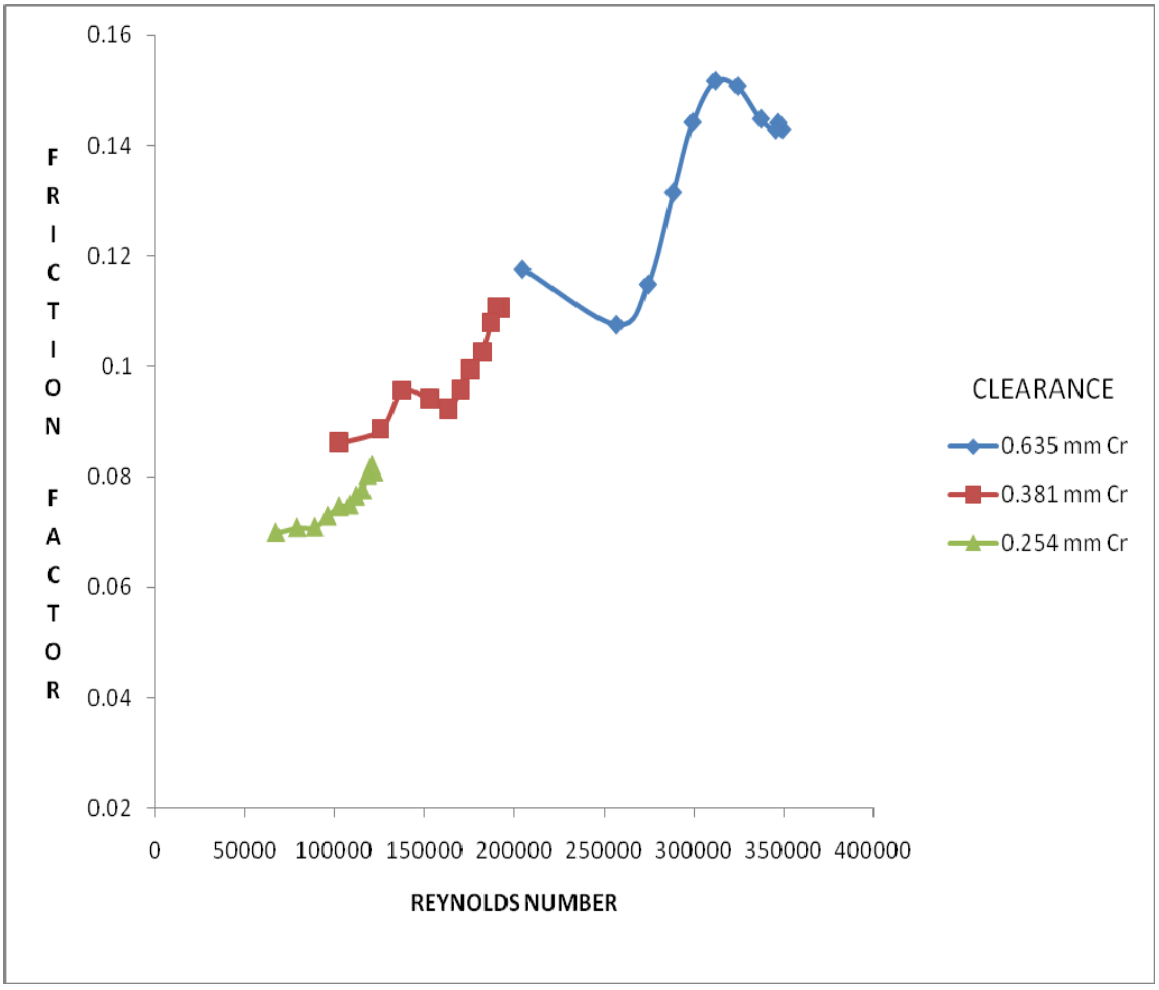

Figure 43. Friction factor vs. Reynolds number for hole-on-hole configuration (P_{in}~55 bars, Ø=3.175 mm, d=3.302 mm).

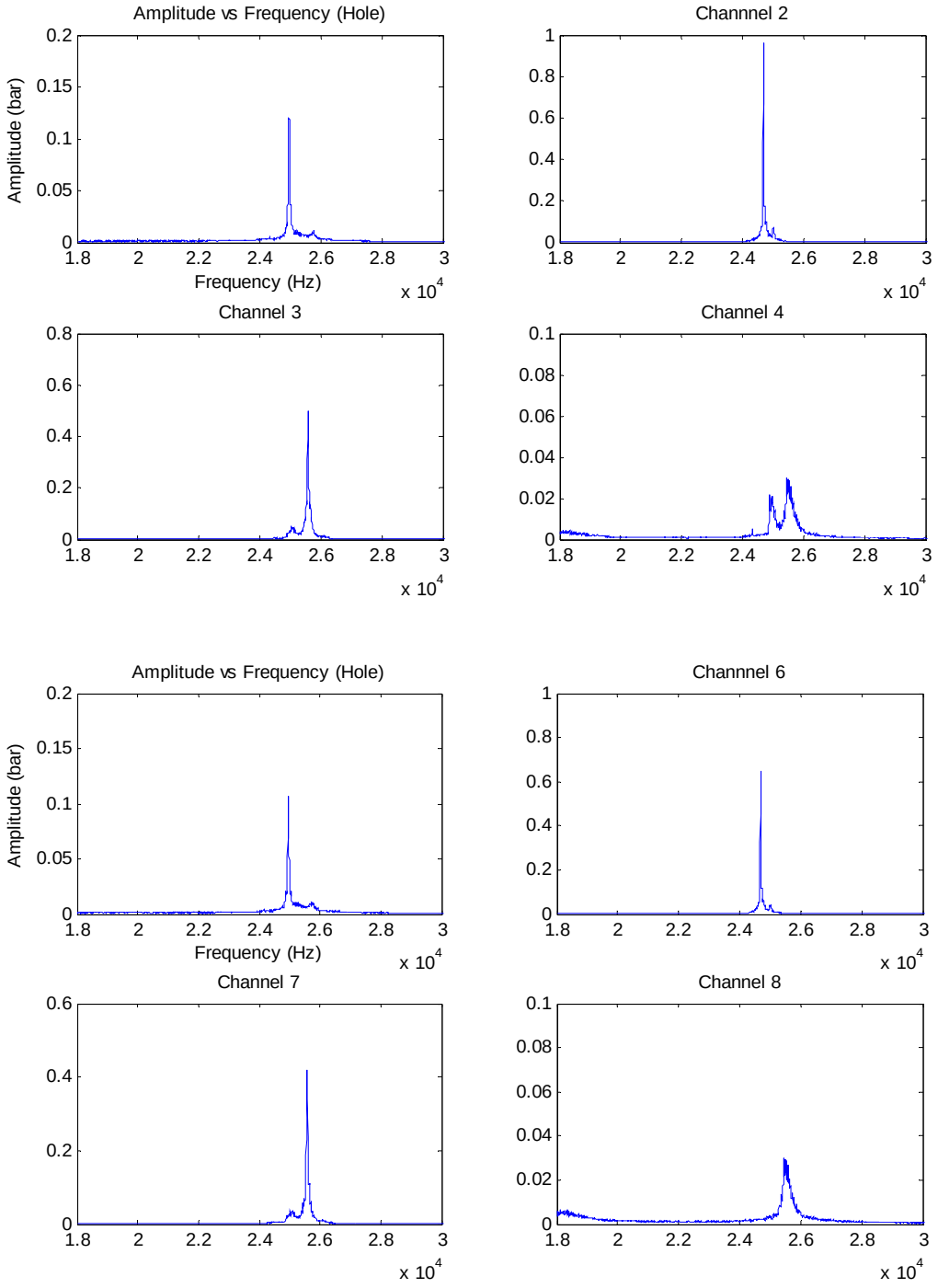

Figure 44. Frequency spectra for hole-on-hole configuration (d=3.302 mm, C_p=0.635 mm, Pin= 84 bar, Re=478962).

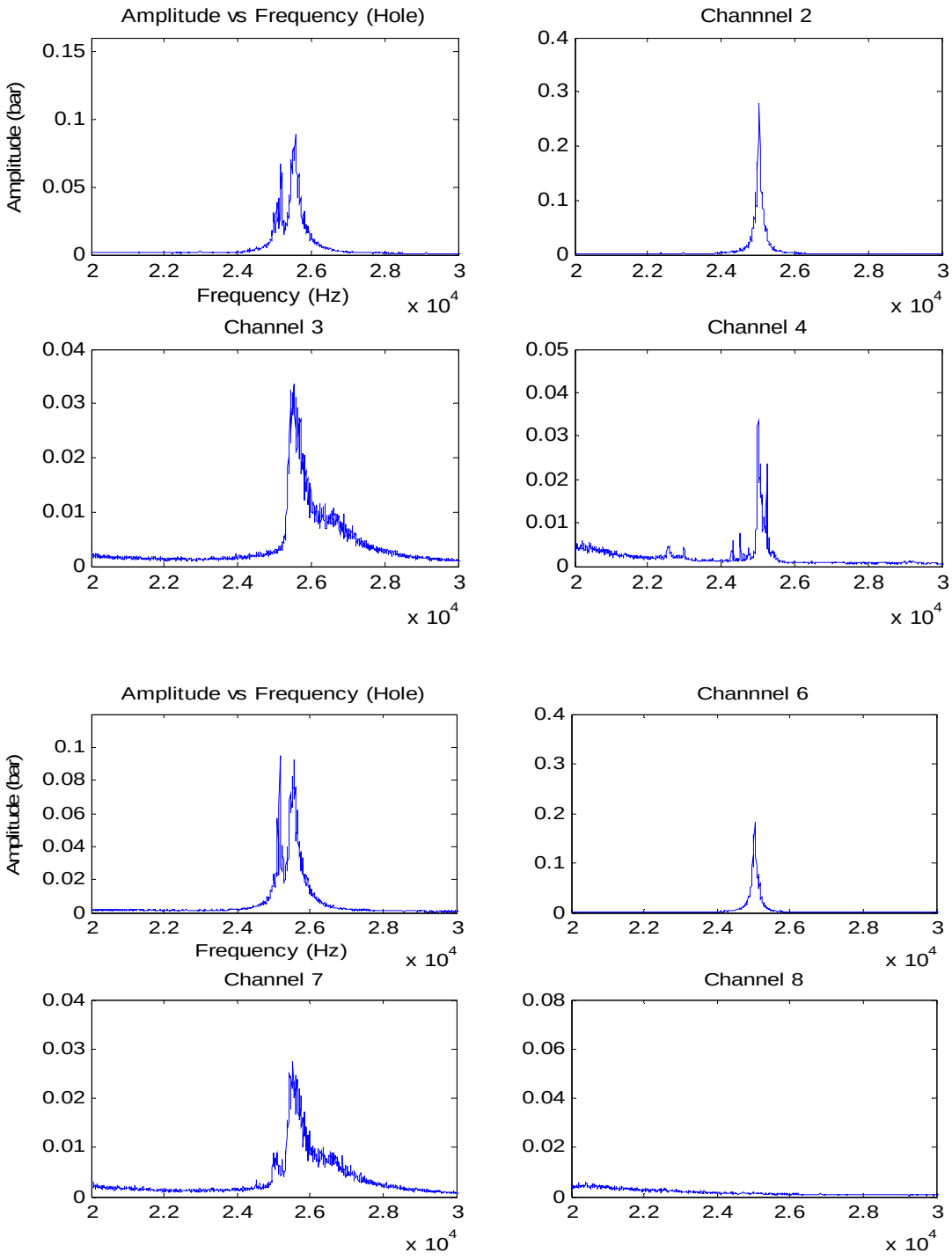

Figure 45. Frequency spectra for hole-on-hole configuration (d=3.302 mm, C_p=0.635 mm, P_{in}= 84 bar, Re=521813).

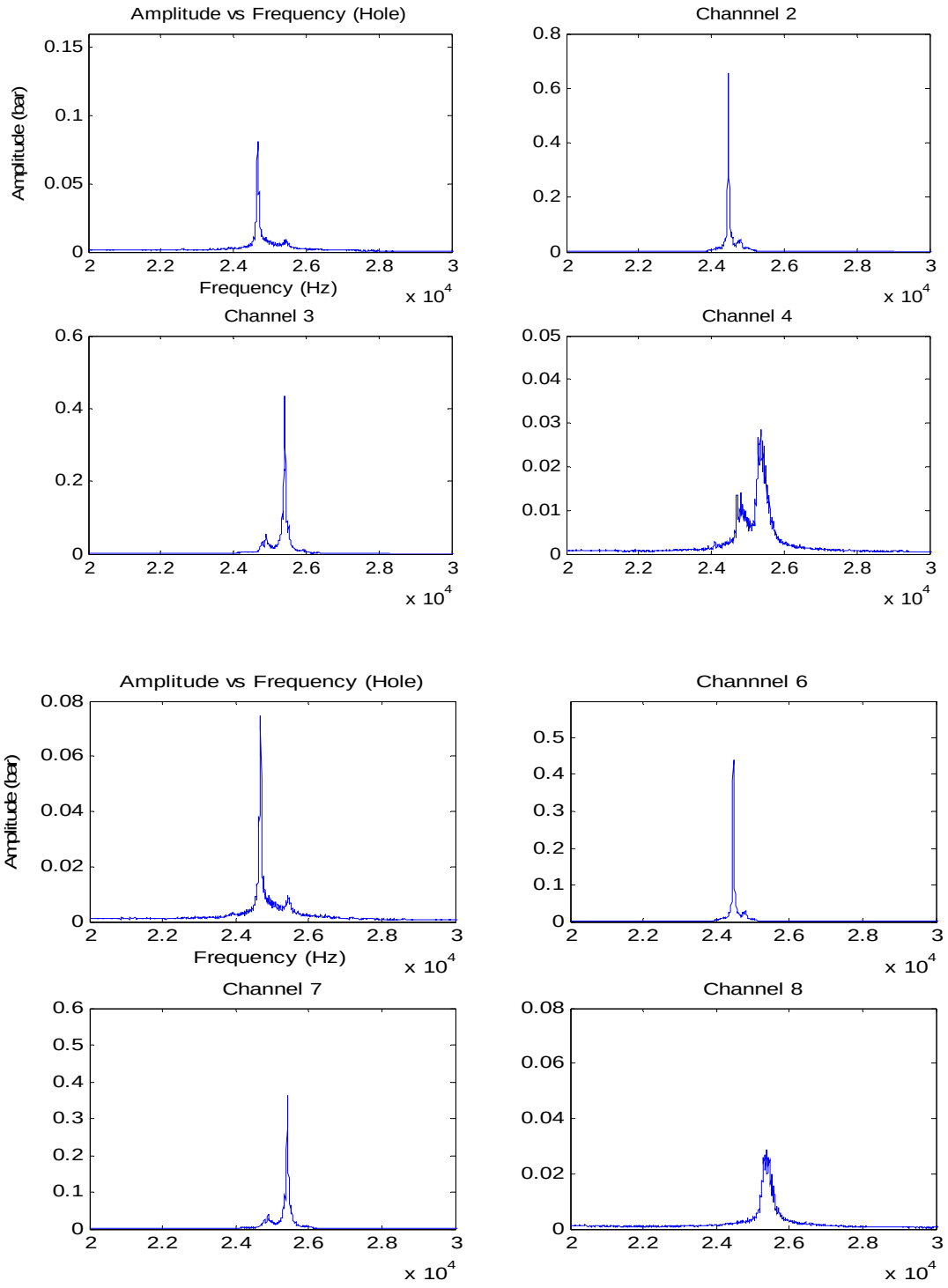

Figure 46. Frequency spectra for hole-on-hole configuration (d=3.302 mm, C_p=0.635 mm, P_{in}=70 bar).

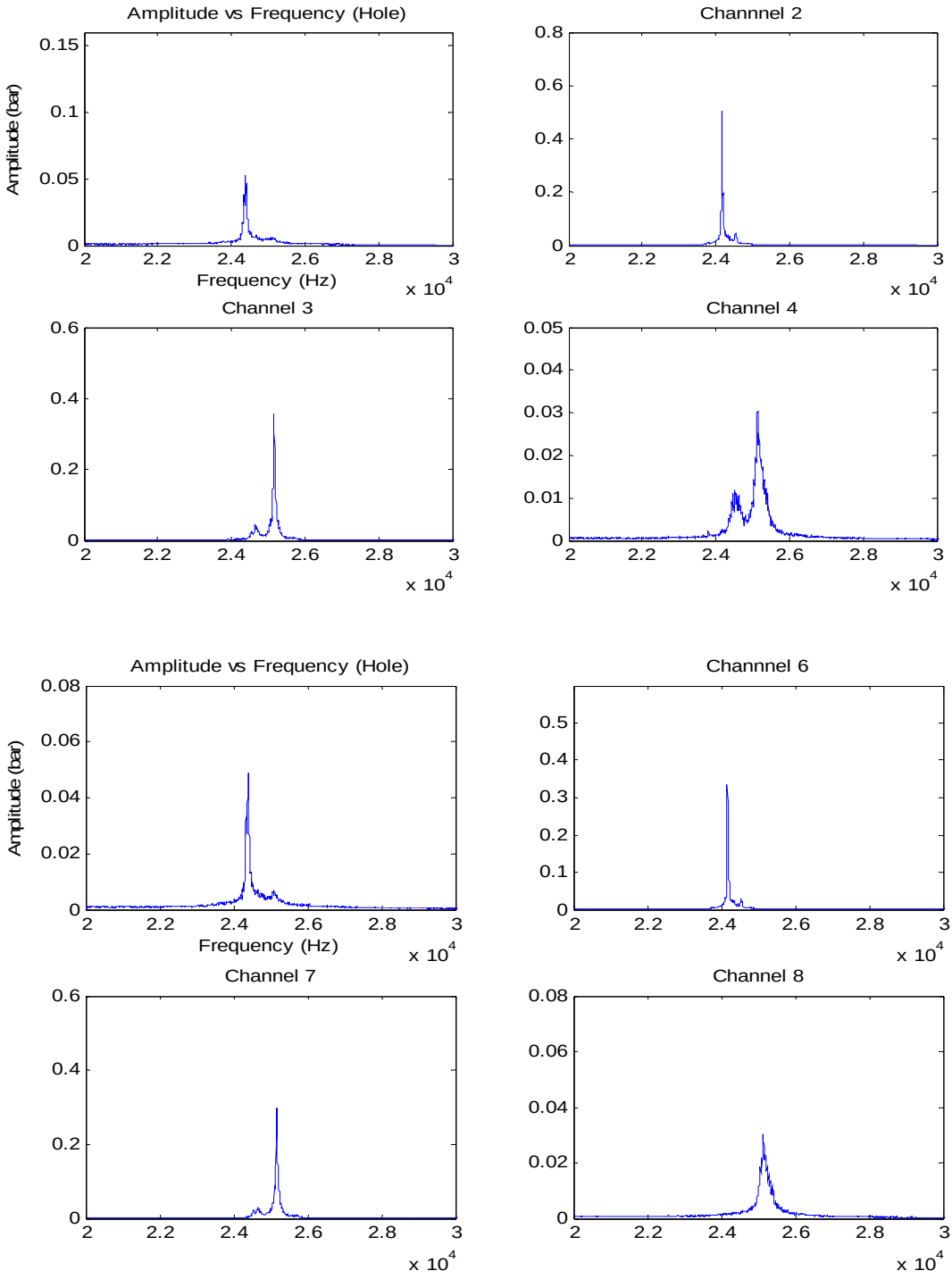

Figure 47. Frequency spectra for hole-on-hole configuration (d=3.302 mm, C_p=0.635 mm, P_{in}=55 bar).

UNCERTAINTY ANALYSIS

The general uncertainty analysis is based on the method described by Coleman [23]. The uncertainty in a variable r which is a function of J variables is given by the following formula:

$$U_r = \left[\left(\frac{\partial r}{\partial X_1} U_{X_1}\right)^2 + \left(\frac{\partial r}{\partial X_2} U_{X_2}\right)^2 + \ldots \left(\frac{\partial r}{\partial X_J} U_{X_J}\right)^2 \right]^{\frac{1}{2}}$$

In the case of the Mach number in Eq. (11), the primary variables are $\dot{m}$, P, A and T_t .The uncertainties in these variables are 1.7 x 10^{-5} Kg/sec, 0.008 bar, 1.29 x 10^$^{-6}$ m^2, and 1°K respectively.

Differentiating the Mach number with respect to each of the primary variables yields the following partial derivatives terms:

$$\frac{\partial M}{\partial P} = \frac{\frac{-1}{P}\left(\frac{\dot{m}}{PA}\right)^2 \left(\frac{RT_t}{\gamma}\right)}{M\sqrt{1+0.8\beta}}$$

$$\frac{\partial M}{\partial A} = \frac{\frac{-1}{A}\left(\frac{\dot{m}}{PA}\right)^2 \left(\frac{RT_t}{\gamma}\right)}{M\sqrt{1+0.8\beta}}$$

$$\frac{\partial M}{\partial \dot{m}} = \frac{\dot{m}\left(\frac{\dot{m}}{PA}\right)^2 \left(\frac{RT_t}{\gamma}\right)}{M\sqrt{1+0.8\beta}}$$

$$\frac{\partial M}{\partial T_t} = \frac{(\frac{\dot{m}}{PA})^2(\frac{R}{\gamma})}{2M\sqrt{1+0.8\beta}}$$

where $\beta = \left(\frac{\dot{m}}{PA}\right)^2\left(\frac{RT_t}{\gamma}\right)$

Differentiating the friction factor with respect to the primary variables in Eq. (12) yields the following partial derivatives.

$$\frac{\partial f}{\partial H} = \frac{4(1-M^2)}{\alpha}\frac{dM}{dx}$$

$$\frac{\partial f}{\partial (dx)} = \frac{-4H(1-M^2)}{\alpha}\frac{dM}{(dx)^2}$$

$$\frac{\partial f}{\partial (dx)} = \frac{-8HM\alpha - 4H(4.2M^2+1.4M^4)(1-M^2)}{\alpha^2}\frac{dM}{dx}$$

where $\alpha = 1.4M^3(1+0.2M^2)$

The estimated maximum uncertainty in the Mach number and the friction factor are 2.2% and 2.5% respectively.

CONCLUSIONS

The flat-plate tester has been used to determine the friction factor behavior of high-pressure air flow between various surface configurations including smooth-on-smooth, smooth-on-hole and hole-on-hole. Clearances varied between 0.254 and 0.635 mm with a Reynolds number range from 50,000 to 700,000. Tests were conducted for hole depths of 1.9, 2.6 and 3.302 mm and under 3 different inlet pressures (84, 70 and 55 bar).

With the exception of conclusion (a), the following conclusions correspond to tests conducted with the "reverse process" method. Based on the results obtained it was found that:

(a) Tests conducted with the forward process method produced an upset phenomenon regardless of the surface configuration tested. This peculiar phenomenon yields two distinct friction factors (before-upset and after-upset data). The likely explanation for this upset is that choking due to friction occurs at some point in the flow which results in a sudden decrease in the flow rate as the pressure differential increases.

(b) Tests conducted with the reverse process method failed to produce a jump down behavior. In other words, the reverse process reproduced the after-upset data only.

(c) Roughened surfaces provide larger friction factors than smooth surfaces, almost six times in some cases.

(d) In compressible flow, the change in density and local pressure has an impact on the friction factor. The friction factor is a modest function of the inlet pressure and cannot be expressed solely as a function of Reynolds number.

(e) The HP plate with a hole depth of 1.9 mm yields the largest friction factor followed by the HP plates with hole depths of 3.302 and 2.6 mm. Therefore, the 1.9 mm hole depth produces the minimum leakage.

(f) The plateau phenomenon was not encountered in this study. The results obtained are validated by Hess for water flow, Ha and Childs for air, and numerous other studies.

(g) For the non-friction-factor-jump cases, the friction factor remains constant or increases slightly with increasing Reynolds numbers. The frequency spectra

reveal spikes that do not correspond to the Helmholtz frequency. The amplitude of these frequencies increases with increasing clearance. The absence of the Helmholtz frequency is a characteristic of the non-friction-factor-jump cases.

(h) The friction-factor-jump cases are restricted to the rough-on-rough configurations. There is an observed increase in the friction factor as the Reynolds number increases. The corresponding frequency spectra reveal the presence of the Helmholtz frequency. This normal mode resonance interferes with the flow so as to increase the resistance to the main flow thereby increasing the friction factor. Ha obtained similar results for opposed honeycomb surfaces and was able to detect to the Helmholtz frequency that corresponds to the cavity depth tested.

RECOMMENDATIONS

(a) Invest in a new inlet valve that matches more closely the flow rate range of future experiments. This will not only allow for easier control of the valve, but also help reduce the amount of time spent on each test.

(b) Conduct repetitive tests using both the forward process and reverse process methods without shutting down. This will help gain a better understanding of the upset phenomenon encountered in this study.

(c) Extend the Reynolds number Range by testing clearances less than 0.254 mm and greater than 0.635 mm.

(d) Test more plates with different Hole-patterns and hole-diameter to investigate the effect of the hole diameter and spacing of the holes on the friction factor.

(e) The friction factor jump phenomenon occurred by testing two opposed HP plates with a hole depth of 3.302 mm. It would be valuable to perform tests with opposed HP plates with hole depths other than the one used in this study.

REFERENCES

[1] Childs, D.W., 1993, *Turbomachinery Rotordynamics: Phenomena, Modeling and Analysis*, John Wiley & Sons, Inc., New York.

[2] Hirs, G.A., 1973, "Bulk-flow Theory for Turbulence in Lubricant Films," ASME Journal of Lubrication Technology, **95,** pp. 137-146.

[3] Von Pragenau, G., 1982, "Damping Seals for Turbomachinery," NASA Technical Paper No. 1987.

[4] Childs, D.W., and Moyer, D., 1985, "Vibrations Characteristics of the HPOTP (High Pressure Oxygen Turbobump) for the SSME (Space Shuttle Main Engine)," ASME, Journal of Engineering for Gas Turbine and Power, **107 (**1) pp. 152-159.

[5] Zeidan, F., Perez, R., and Stephenson, E., 1993, "The Use of Honeycomb Seals in Stabilizing Two Centrifugal Compressors," *Proceedings of the Twenty-Second Turbomachinery Symposium*, The Turbomachinery Laboratory, Texas A&M University, College Station, TX, pp. 3-15.

[6] San Andres, L., Soulas, T., 2007, "A Bulk Flow Model for Off-centered Honeycomb Gas Seals," ASME Transactions, **129**, pp. 185-193.

[7] Childs, D.W., and Yu, Z., 1988, "A Comparison of Experimental Rotordynamic Coefficients and Leakage Characteristics Between Hole-pattern Gas Damper Seals and a Honeycomb Seal," Journal of Engineering for Gas Turbines and Power, **120**, pp. 778-783.

[8] Wade, J., 2004, "Test Versus Predictions for Rotordynamic Coefficients and Leakage Rates for Hole-pattern Gas Seals at Two Clearances in Choked and Unchoked Conditions," M.S. Thesis, Texas A&M University, College Station, TX.

[9] Massey, B., 2006, *Mechanics of Fluids*, Taylor and Francis Group, New York.

[10] Ha, T.W., 1989, "Friction Factor Data for Flat-Plate Tests of Smooth and Honeycomb Surfaces," M.S. Thesis, Texas A&M University, College Station, TX.

[11] Ha, T.W., 1992, "Rotordynamic Analysis of Annular Honeycomb-Stator Turbulent Gas Seals Using Friction Factor Model Based on Flat Plate Tests," Ph.D. Dissertation, Texas A&M University, College Station, TX.

[12] Thomas, J., 1992, “Determination of Variation of Friction Factor with Reynolds Number for Flow Between Two Closely Spaced Rough Plates,” Senior Thesis, Texas A&M University, College Station, TX.

[13] Nava, D.L., 1993, “Observations of Friction Factors for Various Roughness Patterns in Channel Flow,” M.S. Thesis, Texas A&M University, College Station, TX.

[14] Villasmil, L.A., 2002, “Understanding the Friction Factor Behavior in Liquid Annular Seals with Deliberately Roughened Surfaces, a CFD Approach,” M.S. Thesis, Texas A&M University, College Station, TX.

[15] Villasmil, L.A., 2006, “Parameters Defining Flow Resistance and the Friction Factor Behavior in Liquid Annular Seals with Deliberately Roughened Surfaces,” Ph.D. dissertation, Texas A&M University, College Station, TX.

[16] DeOtte, R., Morrison, G.L., Nava D.L., and Hess, J.C., 1994, “A Study of Friction Factors in Channel Flow Between Plates with Highly Roughened Surfaces,” *Fluid Machinery* 1994, U.S. Rohatgi and A. Ogut, eds, ASME, **195**, New York, pp. 23-27.

[17] Childs, D.W., and Fayolle, P., 1999, “Test Results for Liquid ‘Damper’ Seals Using a Round-Hole Roughness Pattern for the Stators,” ASME Transactions, Journal of Tribology, **121**, pp. 42-49.

[18] Morrison, G.L., 2008, “Gas Dynamics Class Notes,” Texas A&M University, College Station, TX.

[19] John, J.E.A., 2006, *Gas Dynamics,* Allyn and Bacon, Newton, MA.

[20] Hess, J.C., 1993, “Dynamic Pressure Response of Water Flow Between Closely Spaced Roughened Flat Plates,” M.S. Thesis, Texas A&M University, College Station, TX.

[21] Shapiro, A.H., 1953, *The Dynamics and Thermodynamics of Compressible Fluid Flow*, The Ronald Press Company, New York.

[22] Randall, R.H., 1951, *An Introduction to Acoustics*, Addison-Wesley, Reading, MA.

[23] Coleman, H.W., 1989, *Experimentation and Uncertainty Analysis for Engineers*, John Wiley & Sons. Inc, New York.

APPENDIX A

FRICTION FACTOR VS. REYNOLDS NUMBER FOR SMOOTH-ON-HOLE CONFIGURATIONS WITH THREE INLET PRESSURES

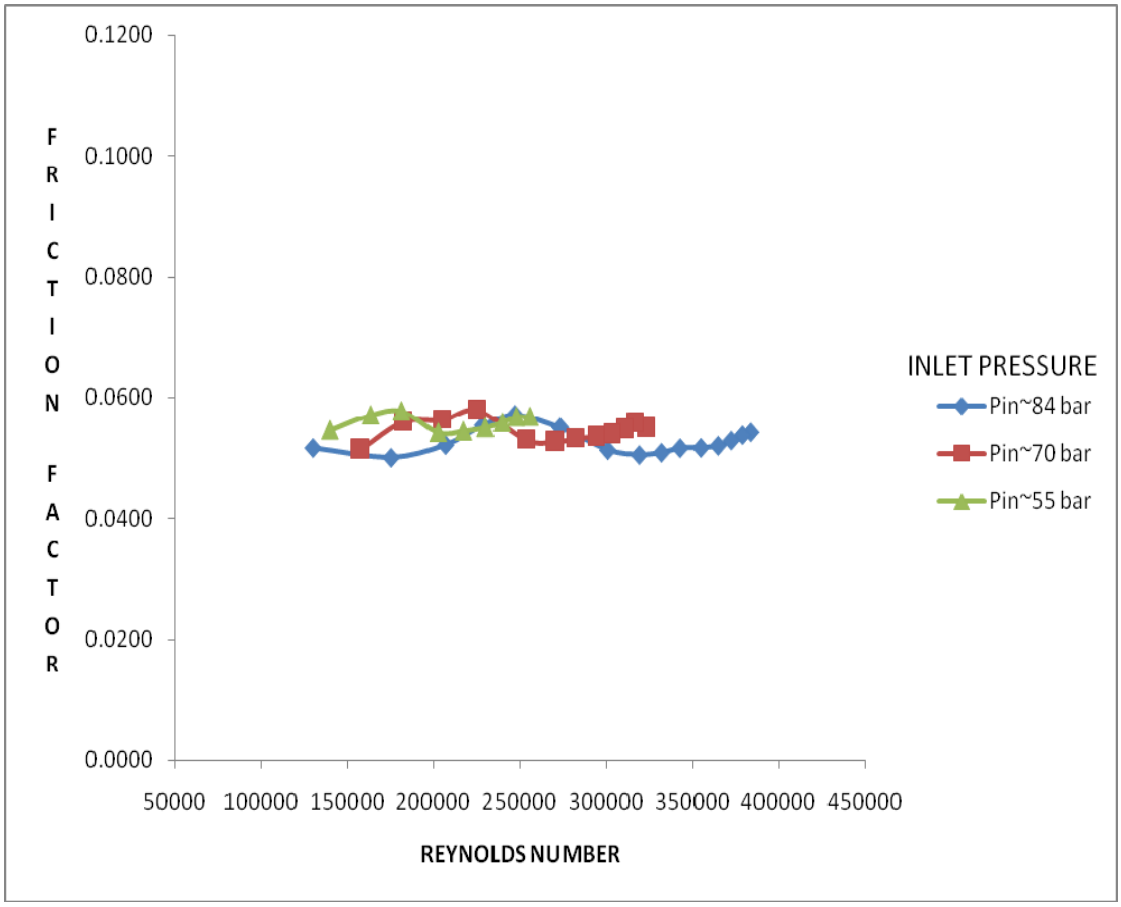

Figure 48. Effect of inlet pressure for smooth-on-hole configuration (Ø=3.175 mm, d=3.302 mm, C_p=0.381 mm).

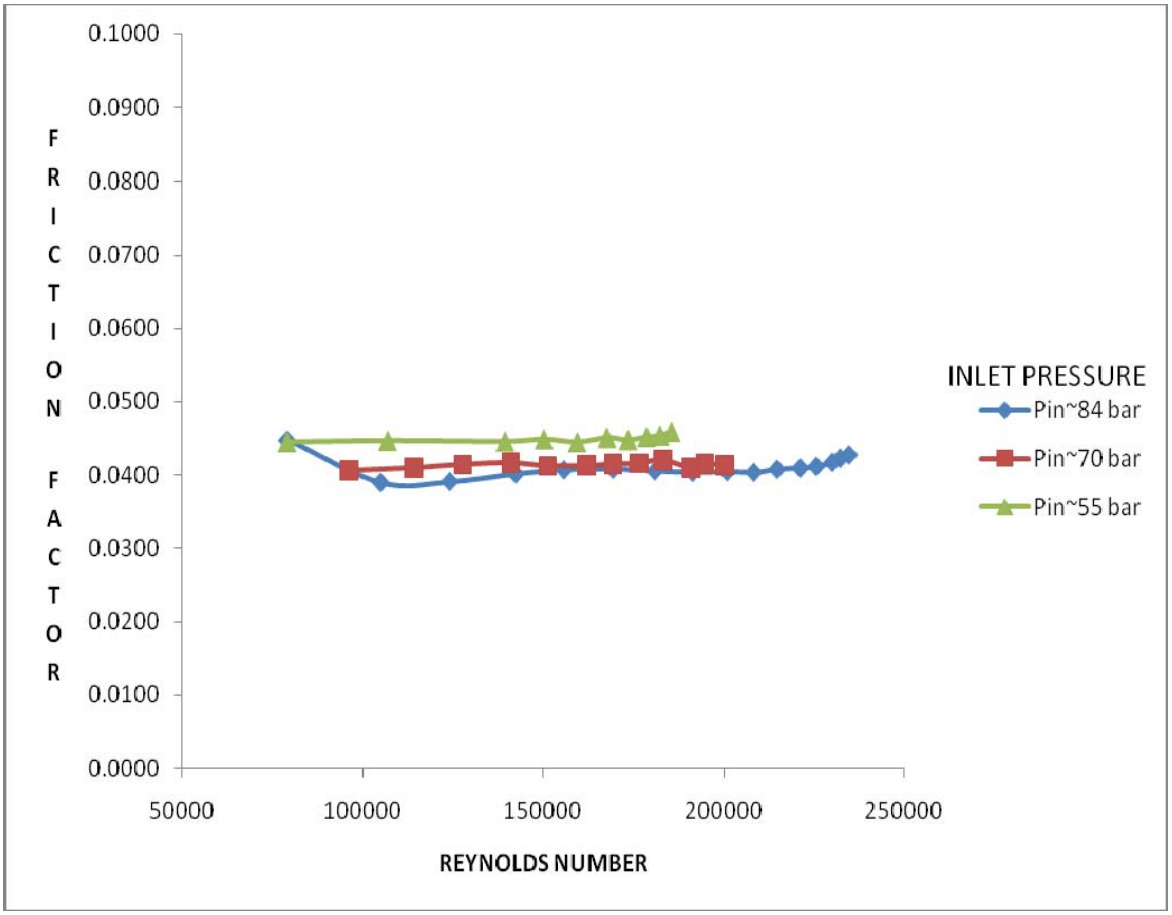

Figure 49. Effect of inlet pressure for smooth-on-hole configuration (Ø=3.175 mm, d=3.302 mm, C_p=0.254 mm).

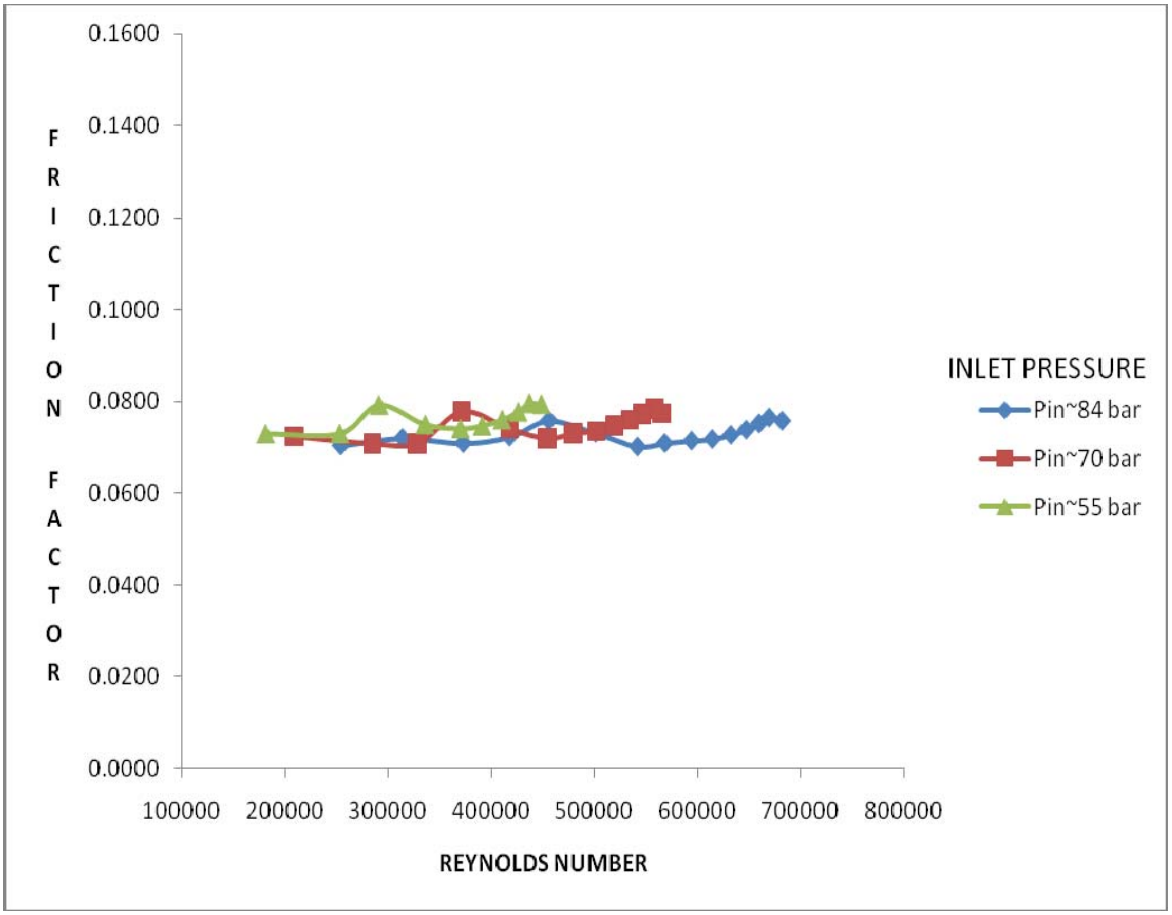

Figure 50. Effect of inlet pressure for smooth-on-hole configuration (Ø=3.175 mm, d=2.6 mm, C_p=0.635 mm).

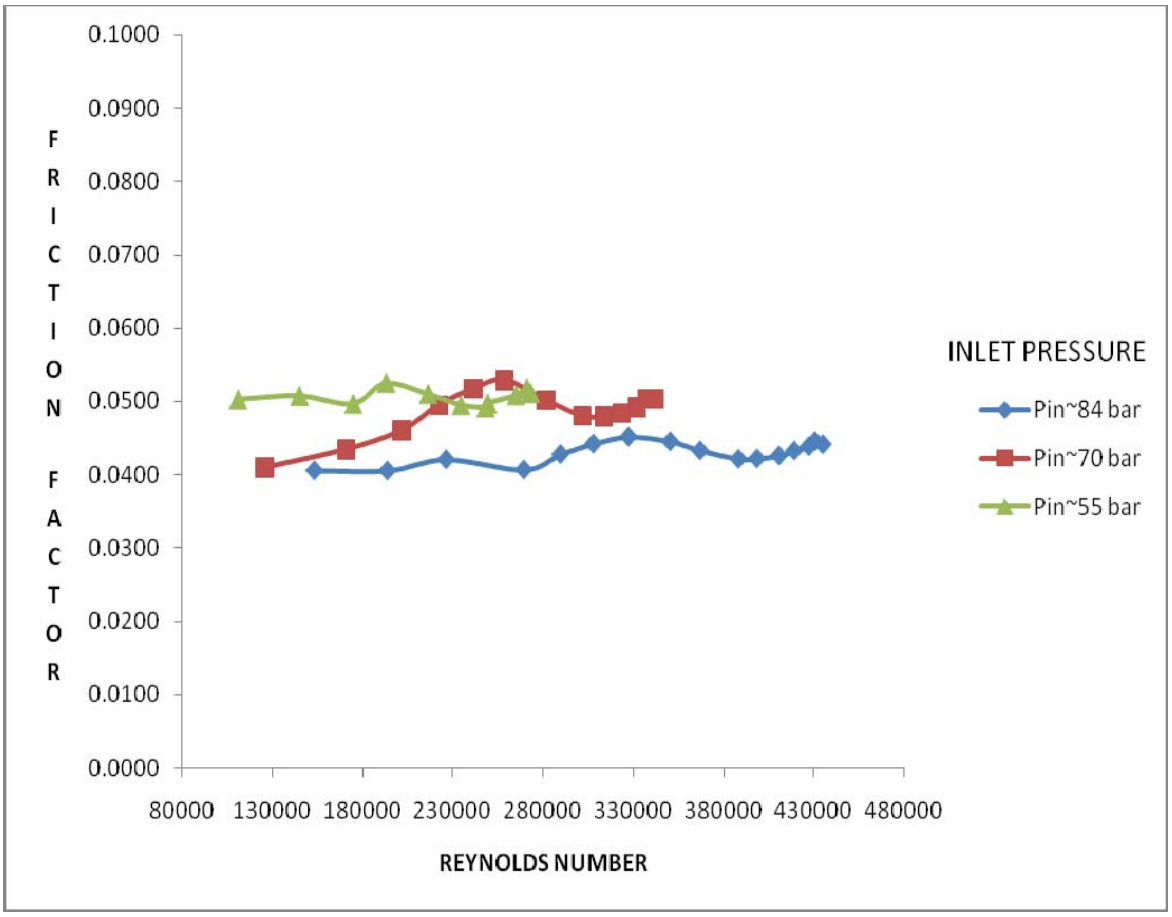

Figure 51. Effect of inlet pressure for smooth-on-hole configuration (Ø=3.175 mm, d=2.6 mm, C_p=0.381 mm).

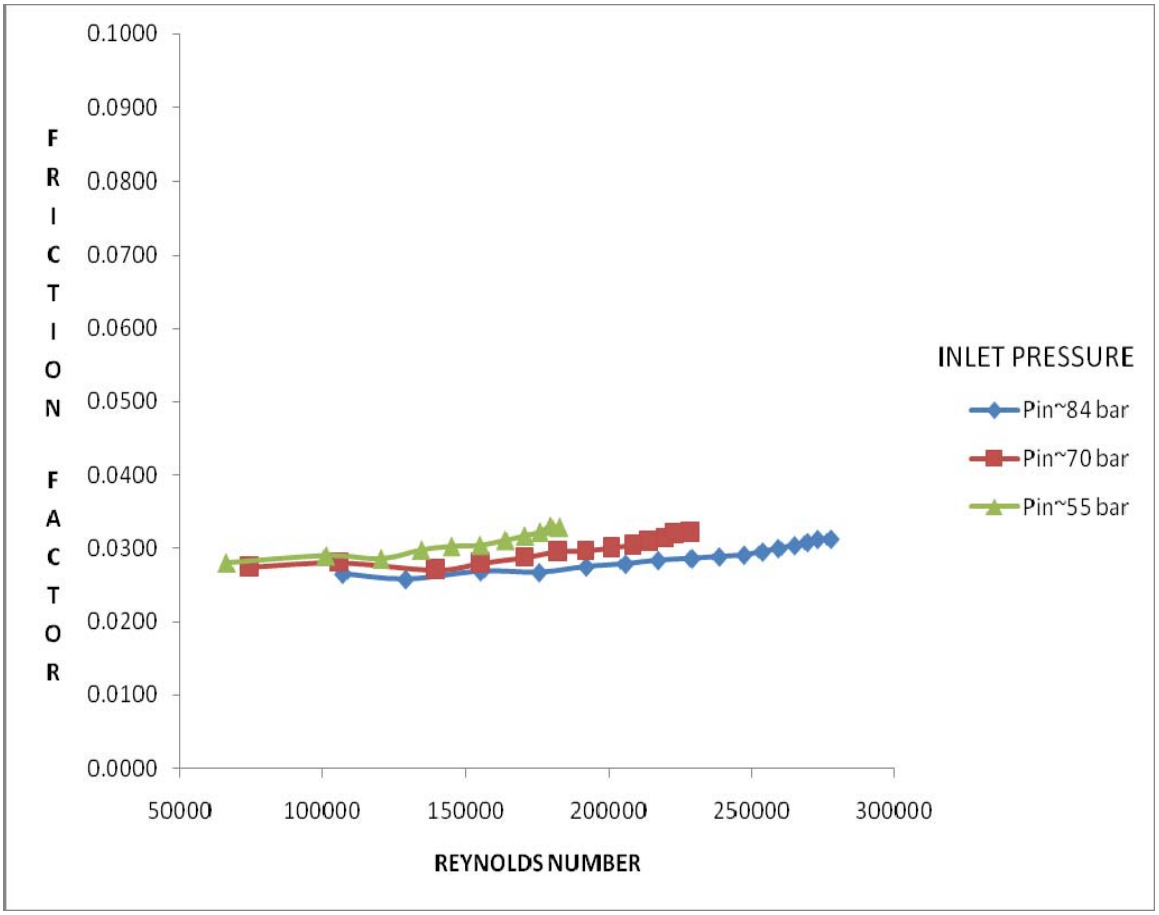

Figure 52. Effect of inlet pressure for smooth-on-hole configuration (Ø=3.175 mm, d=2.6 mm, C_p=0.254 mm).

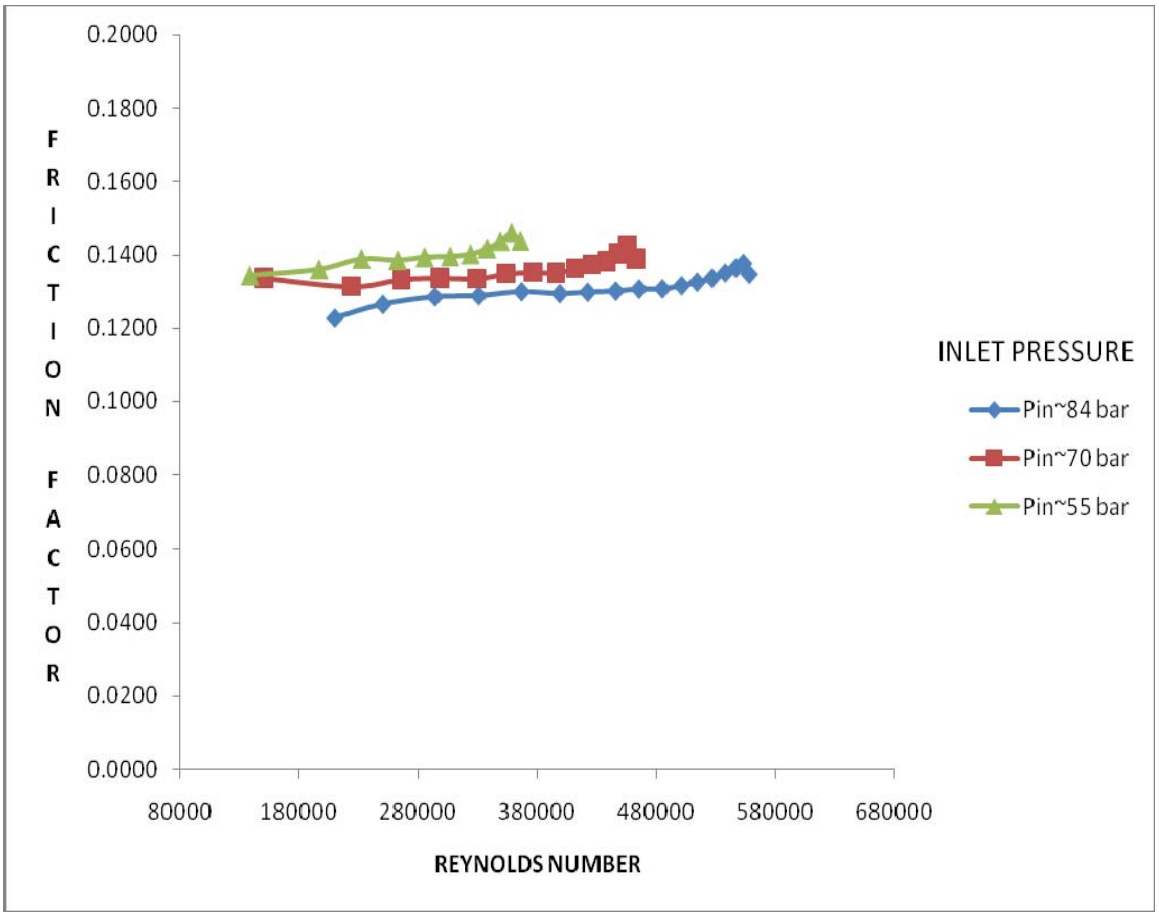

Figure 53. Effect of inlet pressure for smooth-on-hole configuration (Ø=3.175 mm, d=1.9 mm, C_p=0.635 mm).

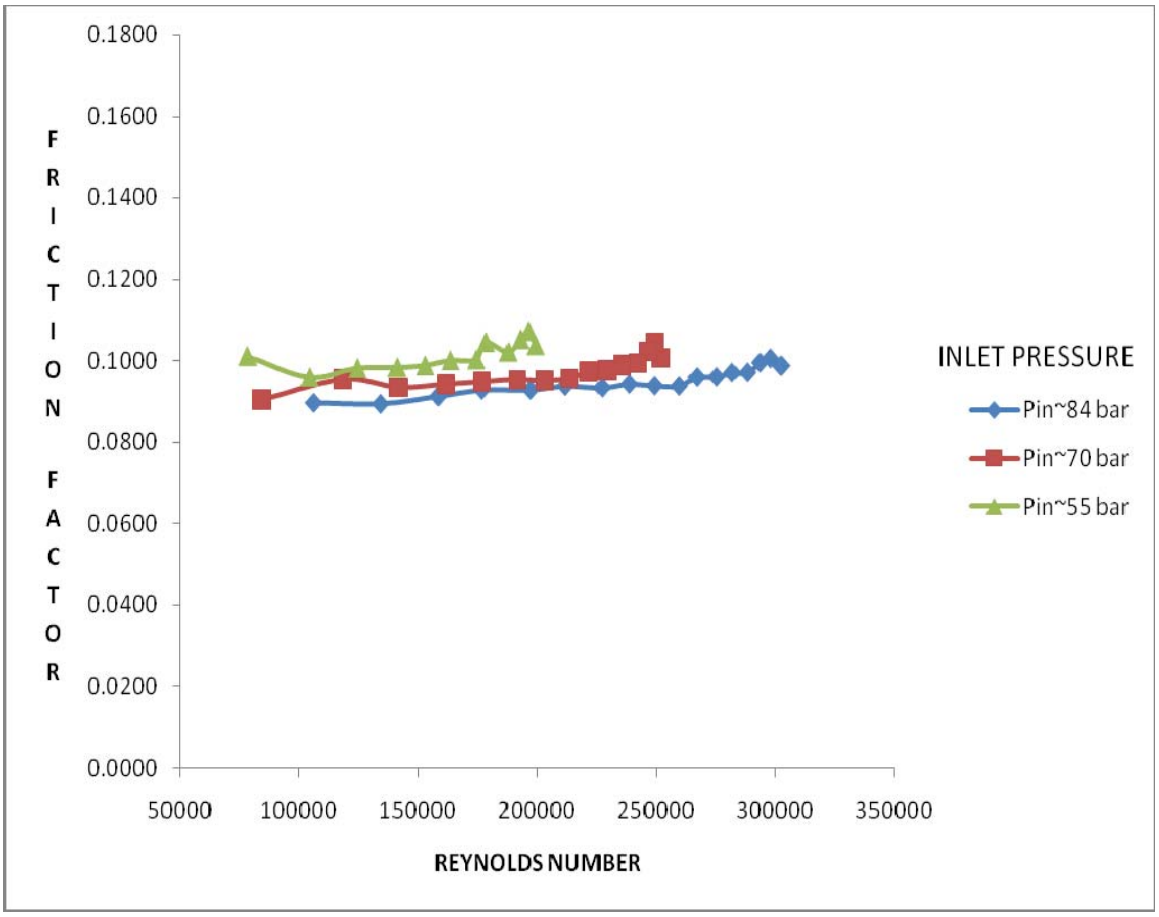

Figure 54. Effect of inlet pressure for smooth-on-hole configuration (Ø=3.175 mm, d=1.9 mm, C_p=0.381 mm).

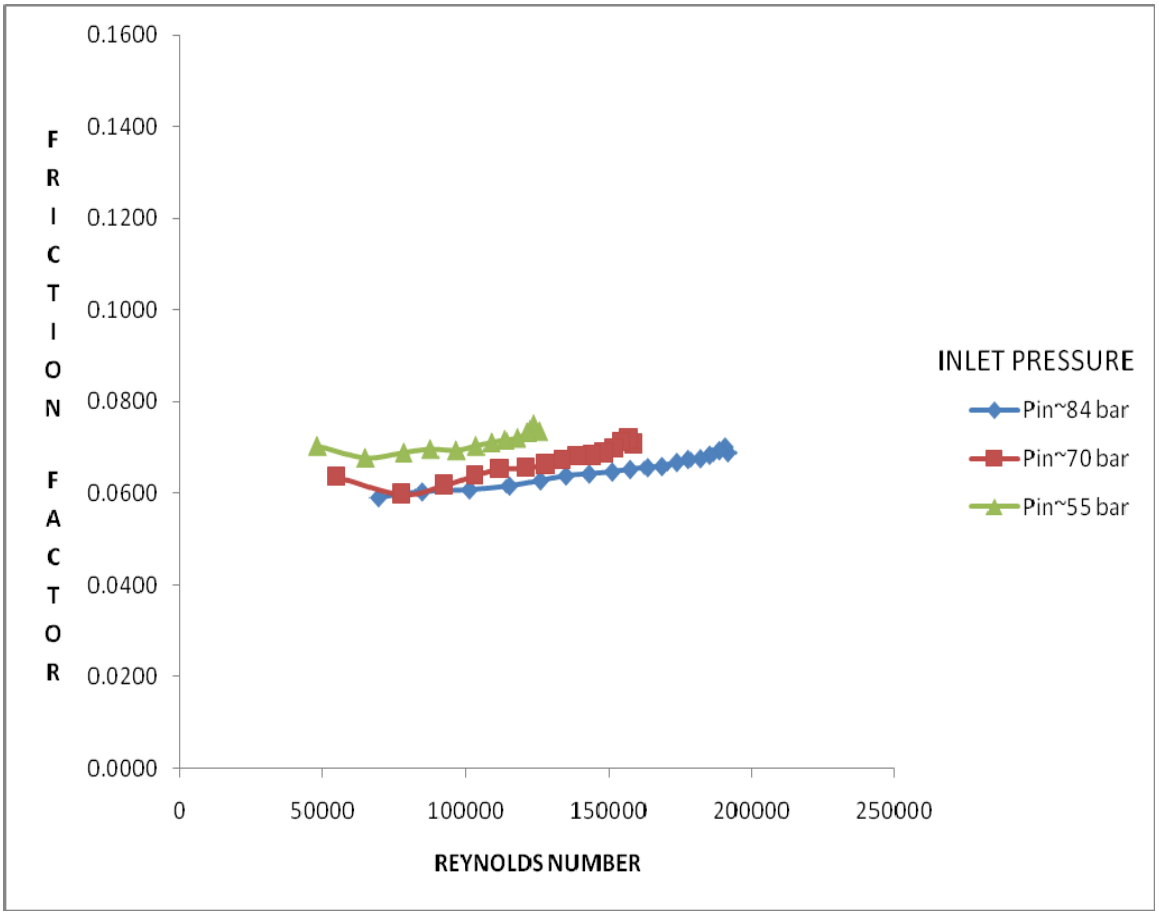

Figure 55. Effect of inlet pressure for smooth-on-hole configuration (Ø=3.175 mm, d=1.9 mm, C_p=0.254 mm).

APPENDIX B

FRICTION FACTOR VS. REYNOLDS NUMBER FOR SMOOTH-ON-HOLE CONFIGURATIONS WITH THREE CLEARANCES

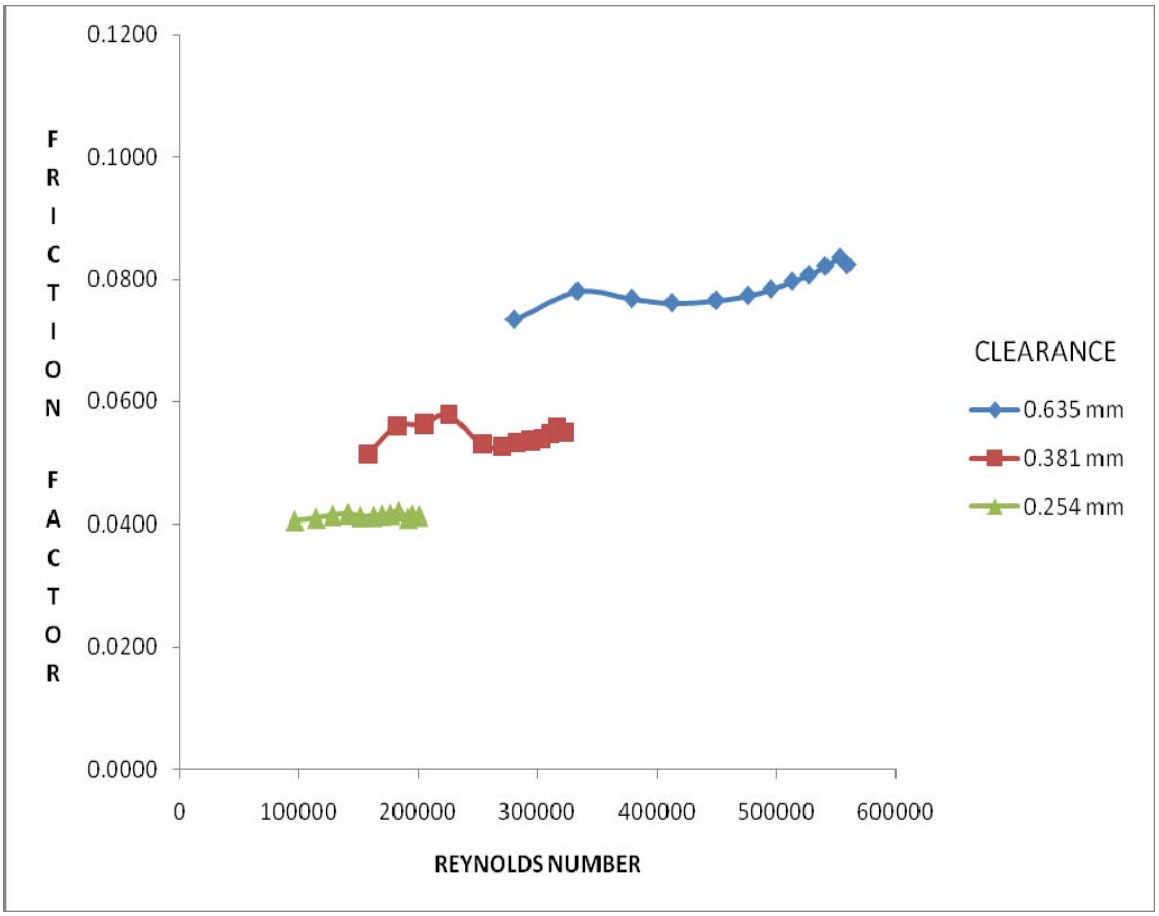

Figure 56. Effect of clearance for smooth-on-hole configuration (P_{in}~70 bar, Ø=3.175 mm, d=3.302 mm).

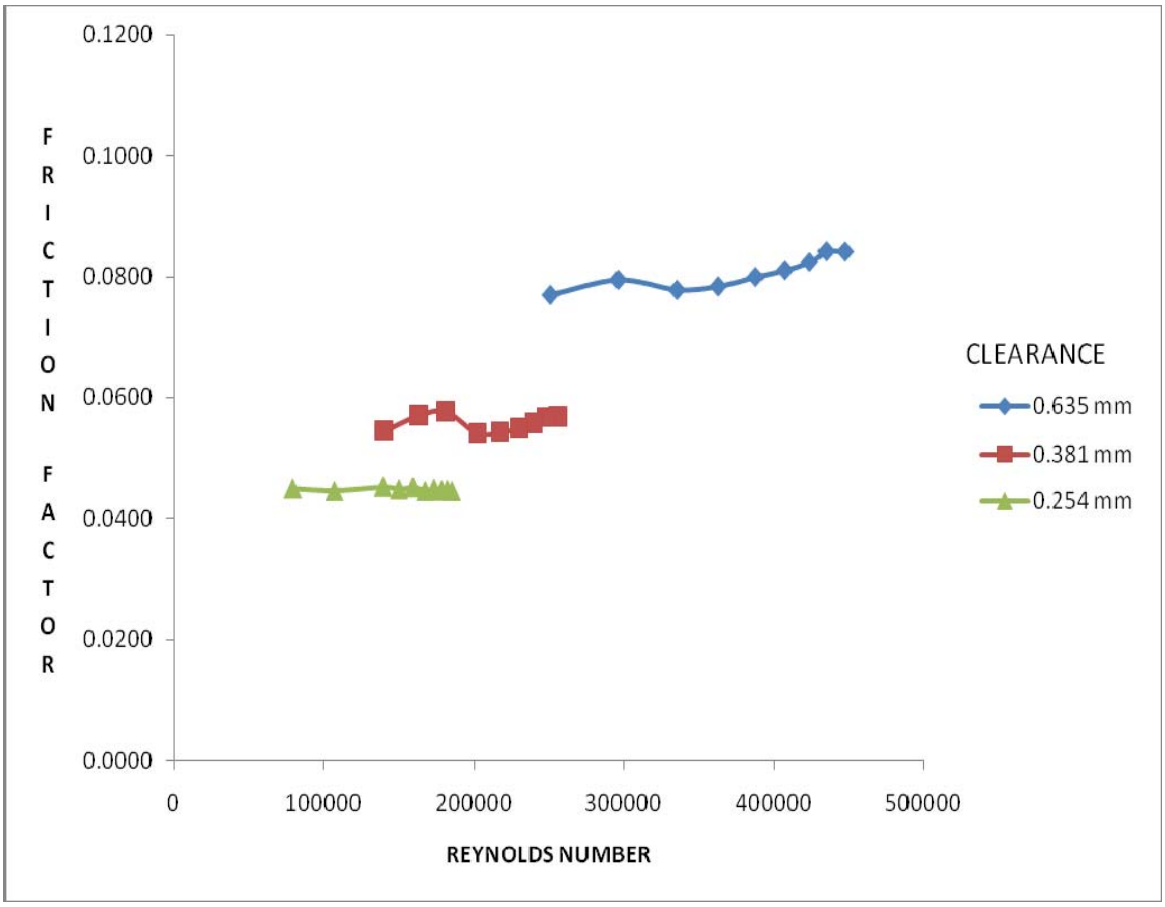

Figure 57. Effect of clearance for smooth-on-hole configuration (P_{in}~55 bar, Ø=3.175 mm, d=3.302 mm).

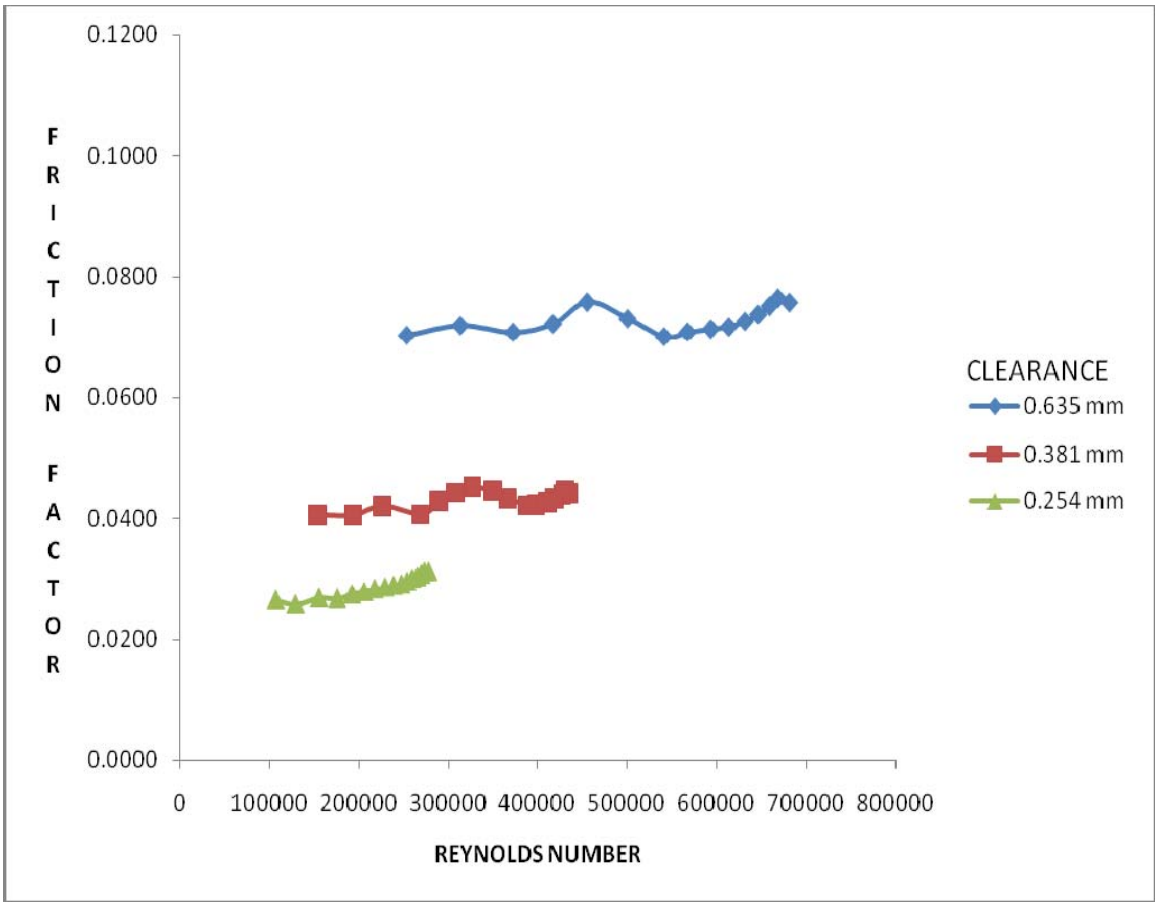

Figure 58. Effect of clearance for smooth-on-hole configuration (P_{in}~84 bar, Ø=3.175 mm, d=2.6 mm).

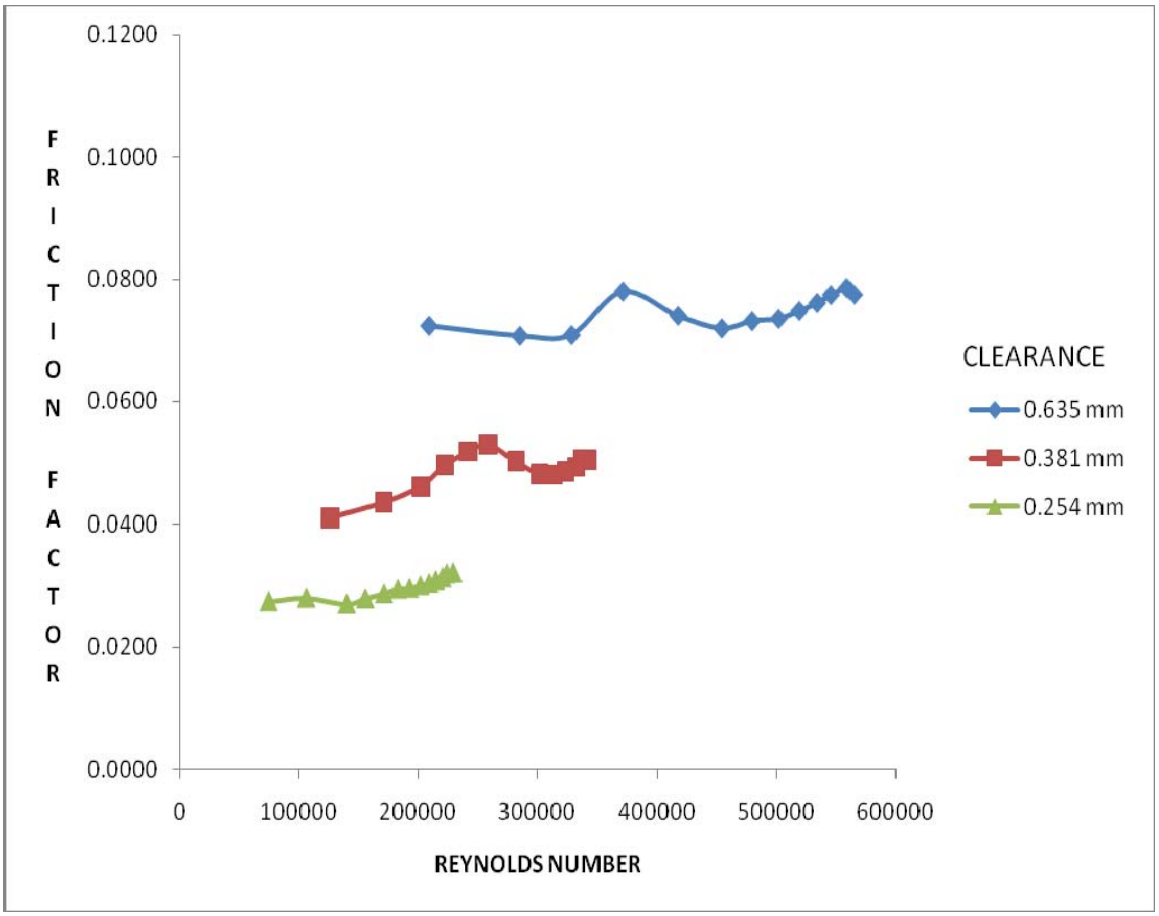

Figure 59. Effect of clearance for smooth-on-hole configuration (P_{in}~70 bar, Ø=3.175 mm, d=2.6 mm).

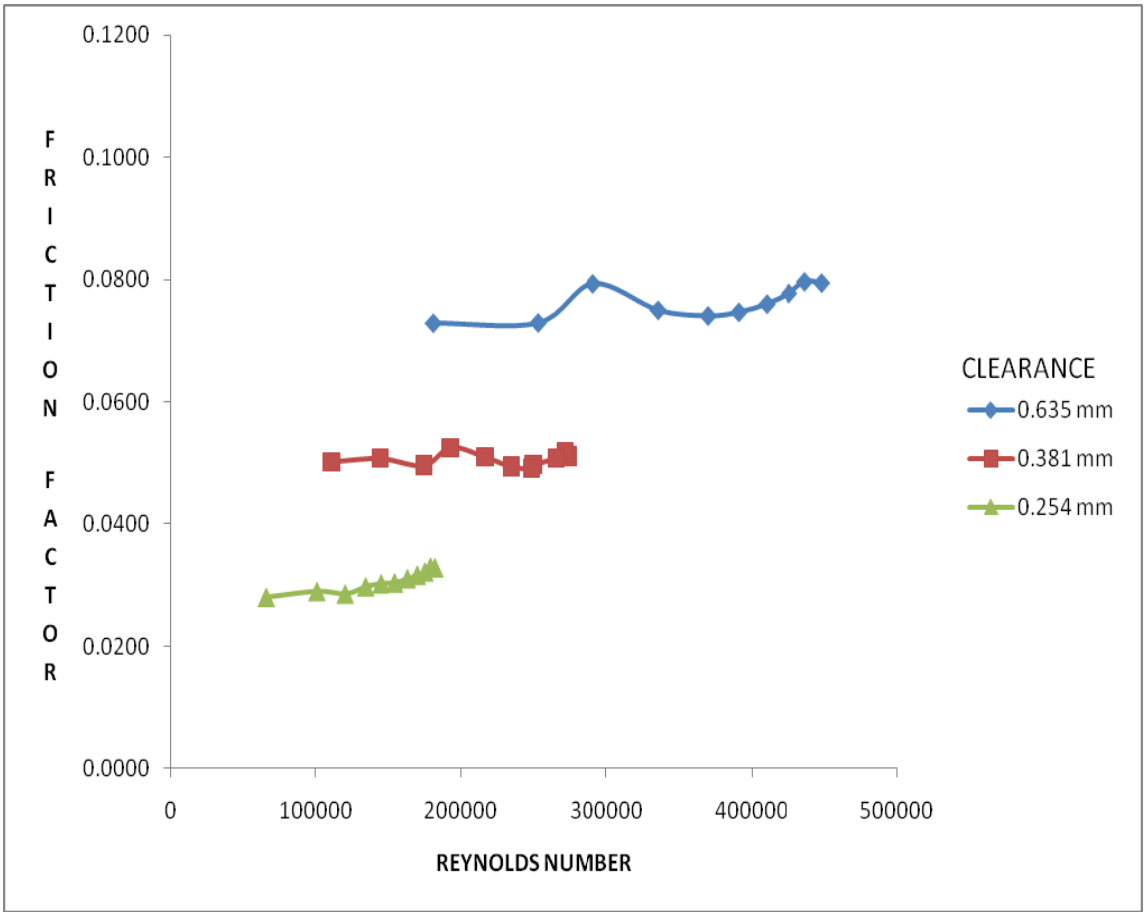

Figure 60. Effect of clearance for smooth-on-hole configuration (P_{in}~55 bar, Ø=3.175 mm, d=2.6 mm).

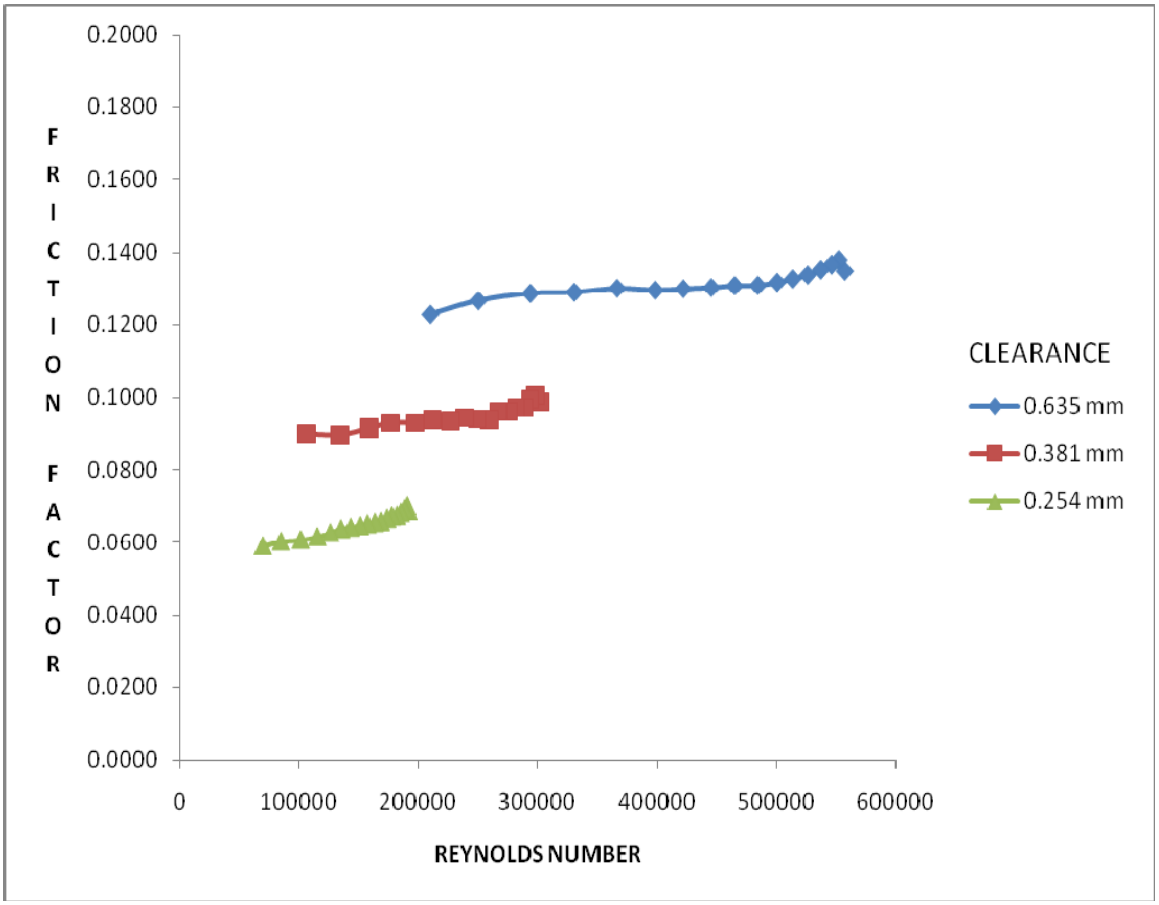

Figure 61. Effect of clearance for smooth-on-hole configuration (P_{in}~ 84 bar, Ø=3.175 mm, d=1.9 mm).

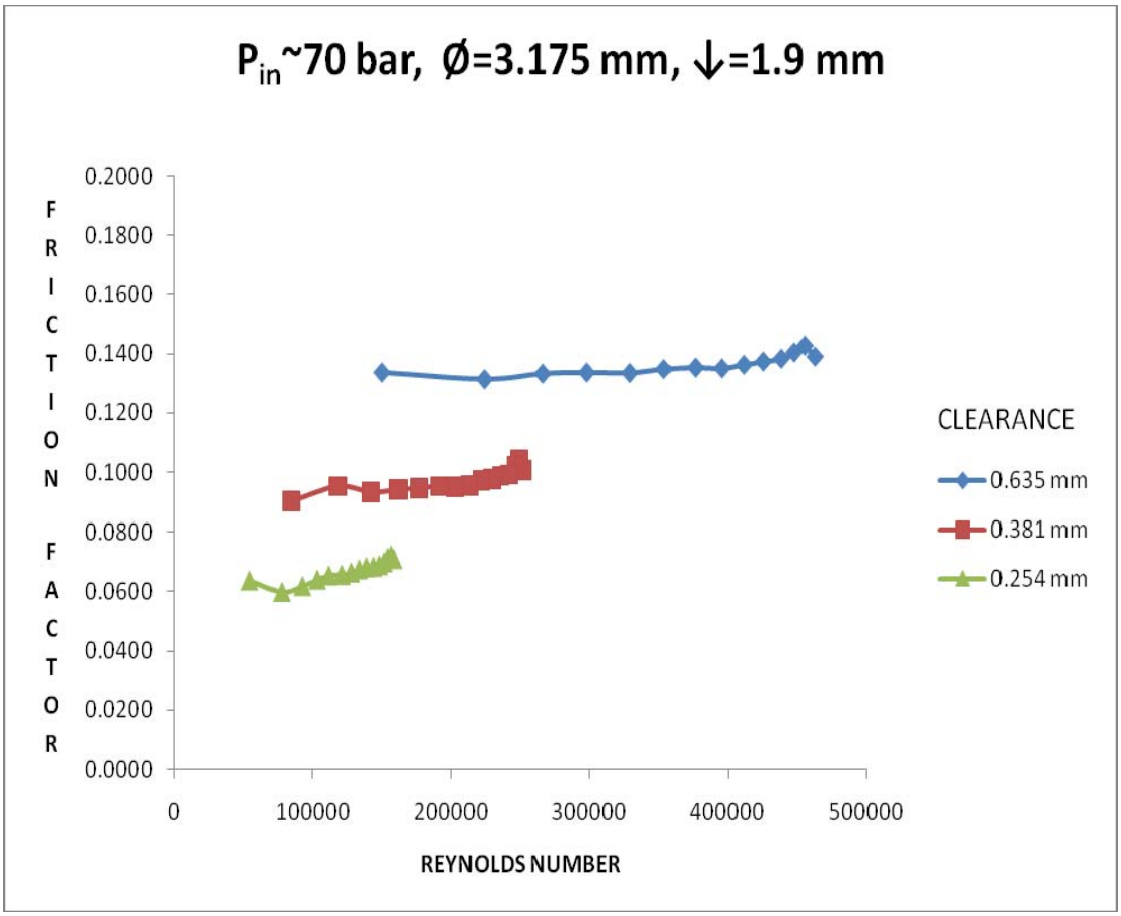

Figure 62. Effect of clearance for smooth-on-hole configuration (P_{in}~70 bar, Ø=3.175 mm, d=1.9 mm).

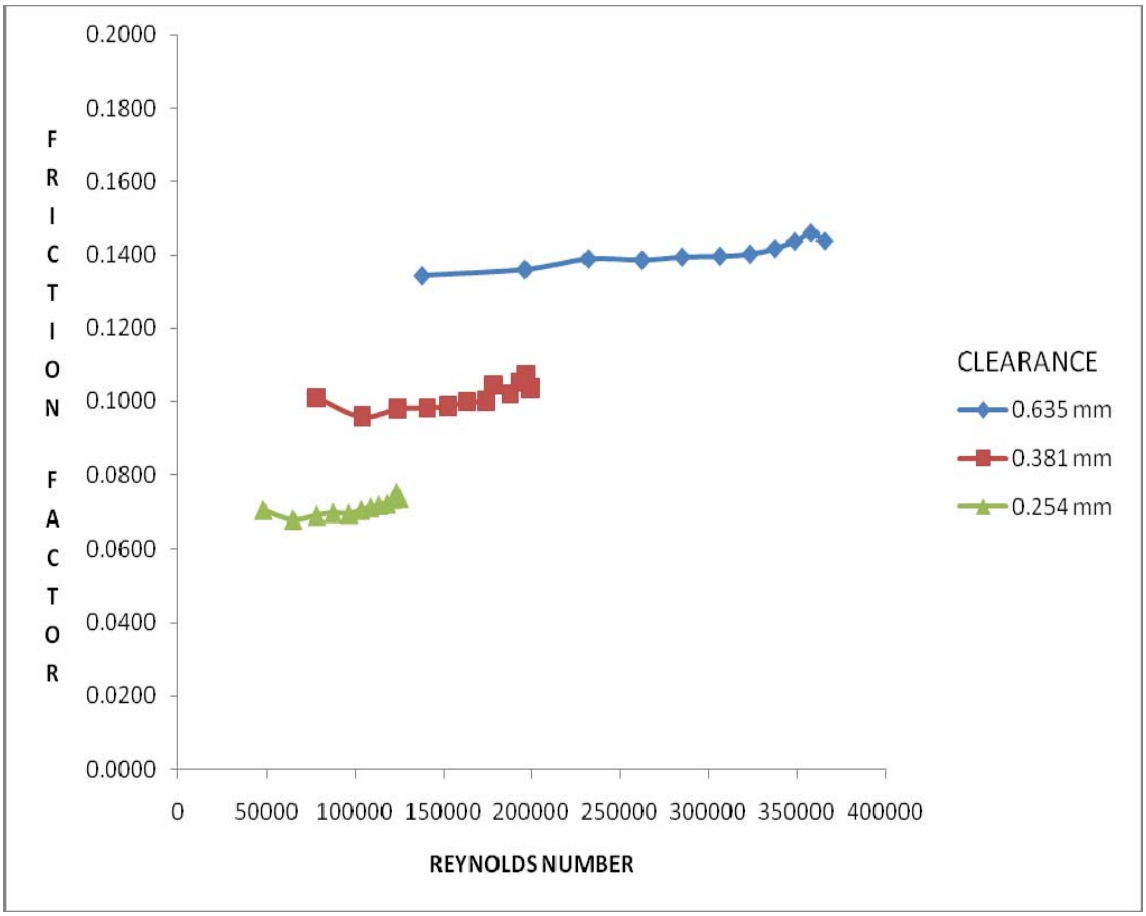

Figure 63. Effect of clearance for smooth-on-hole configuration (P_{in}~55 bar, Ø=3.175 mm, d=1.9 mm).

APPENDIX C

FRICTION FACTOR VS. REYNOLDS NUMBER FOR SMOOTH-ON-HOLE SURFACES WITH THREE HOLE DEPTHS

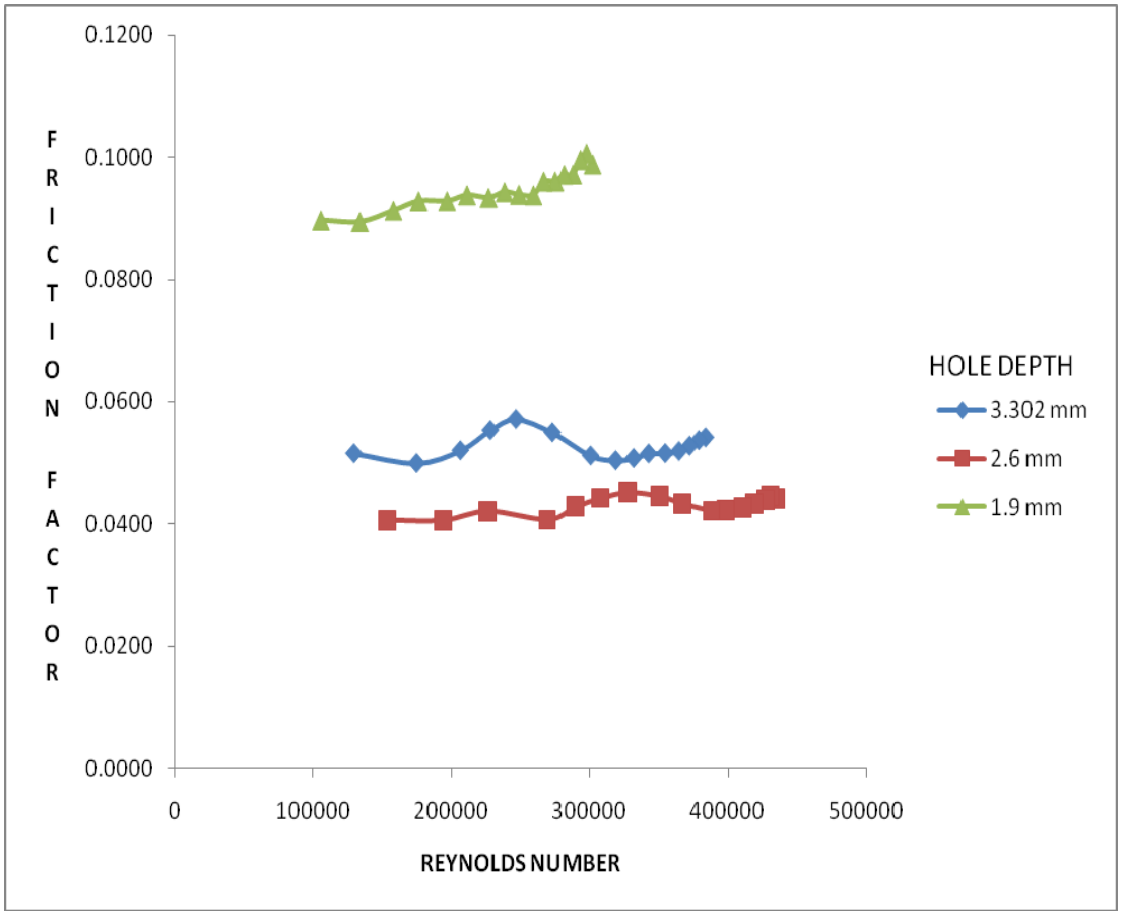

Figure 64. Effect of hole depth for smooth-on-hole configuration (P_{in}~84 bar, Ø=3.175 mm, C_p=0.381 mm).

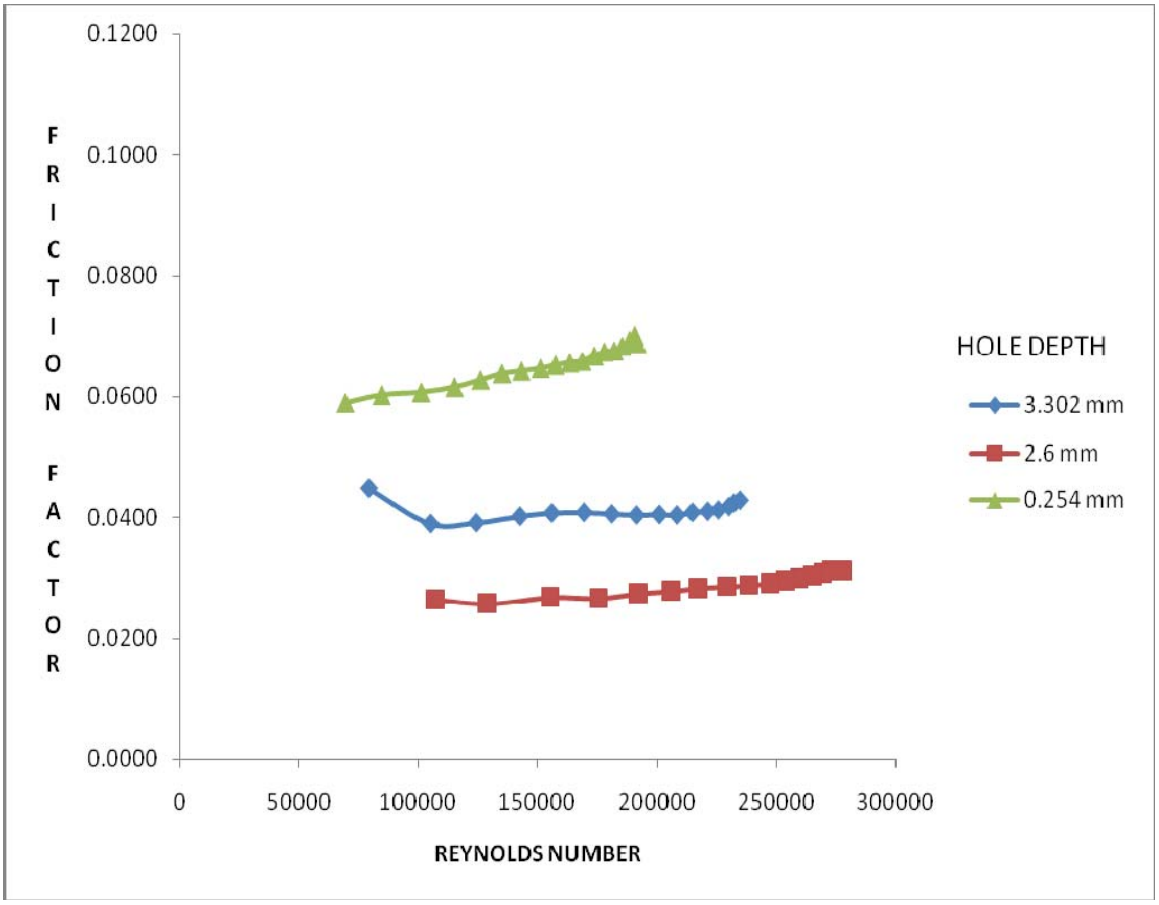

Figure 65. Effect of hole depth for smooth-on-hole configuration (P_{in}~84 bar, Ø=3.175 mm, C_p=0.381 mm).

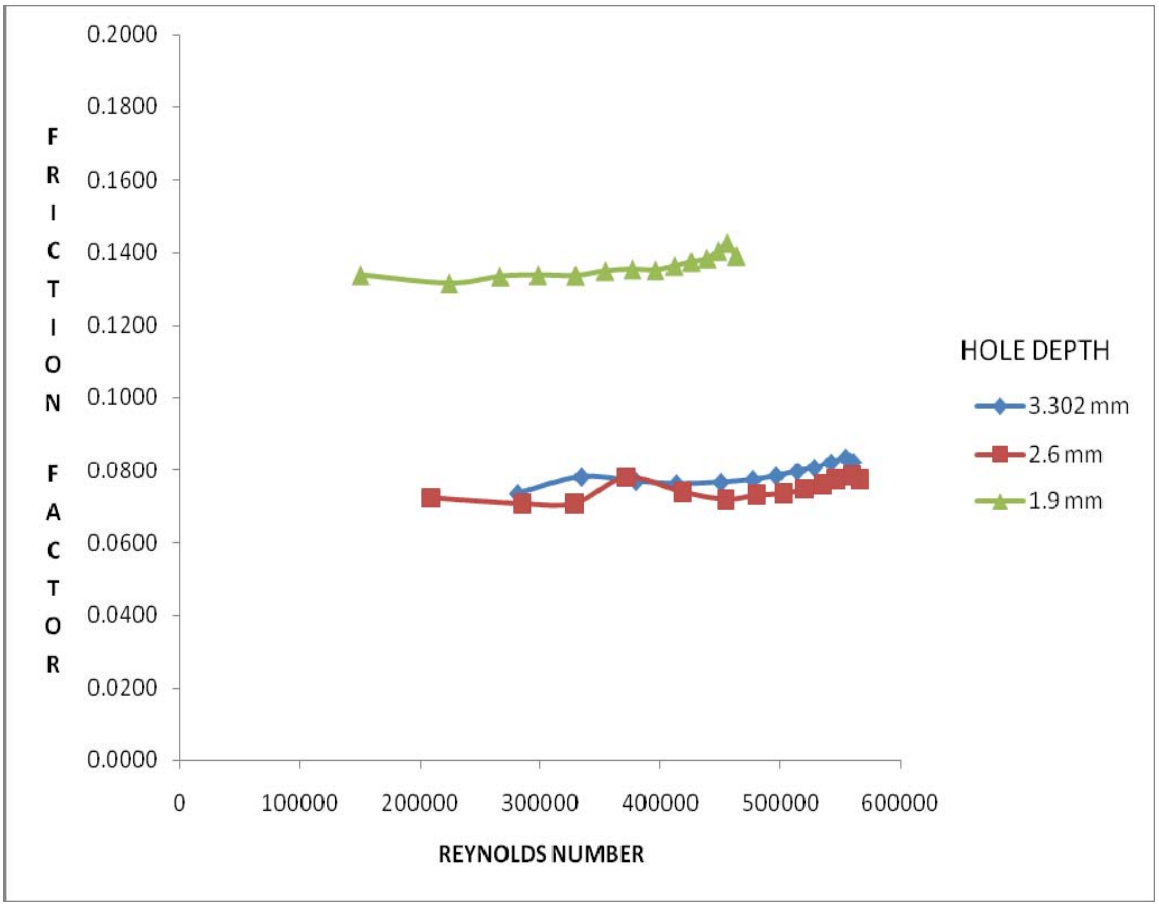

Figure 66. Effect of hole depth for smooth-on-hole configuration (P_{in}~70 bar, Ø=3.175 mm, C_p=0.635 mm).

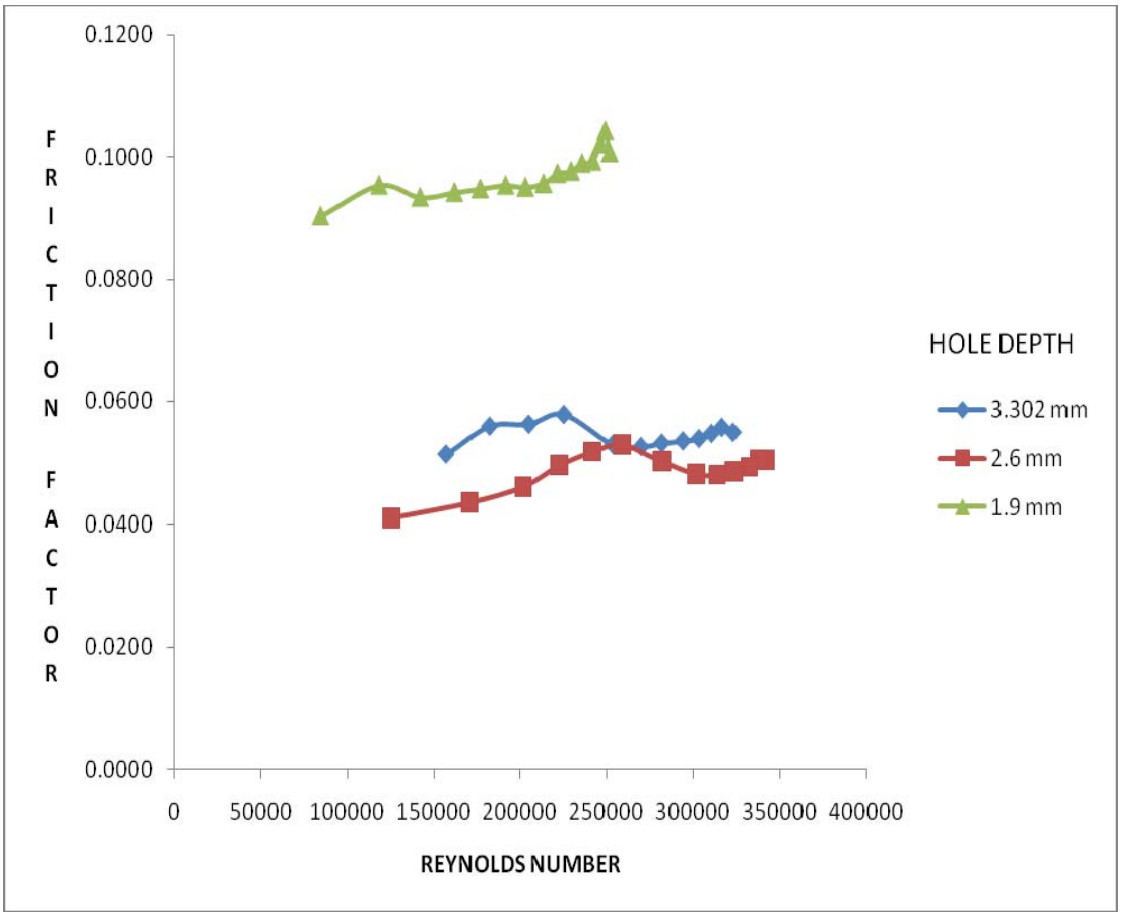

Figure 67. Effect of hole depth for smooth-on-hole configuration (P_{in}~70 bar, Ø=3.175 mm, C_p=0.381 mm).

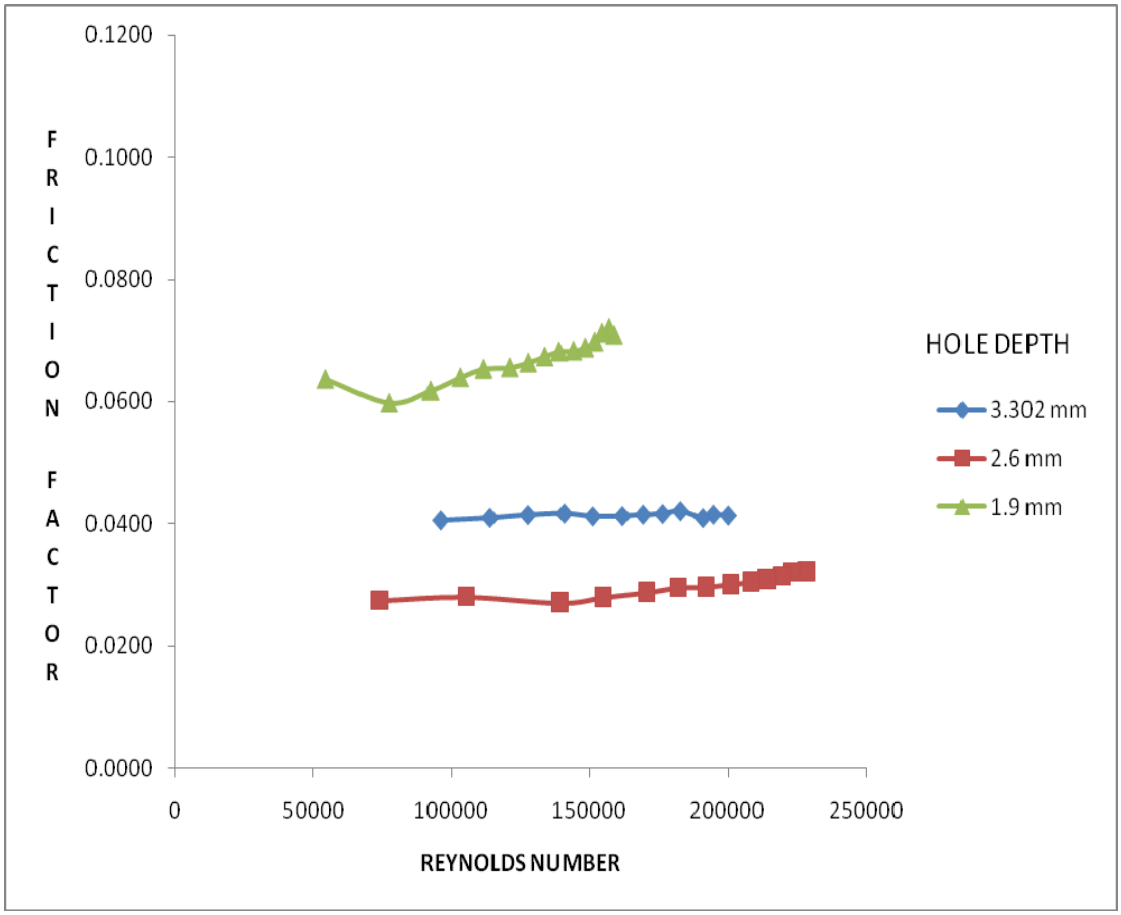

Figure 68. Effect of hole depth for smooth-on-hole configuration (P_{in}~70 bar, Ø=3.175 mm, C_p=0.254 mm).

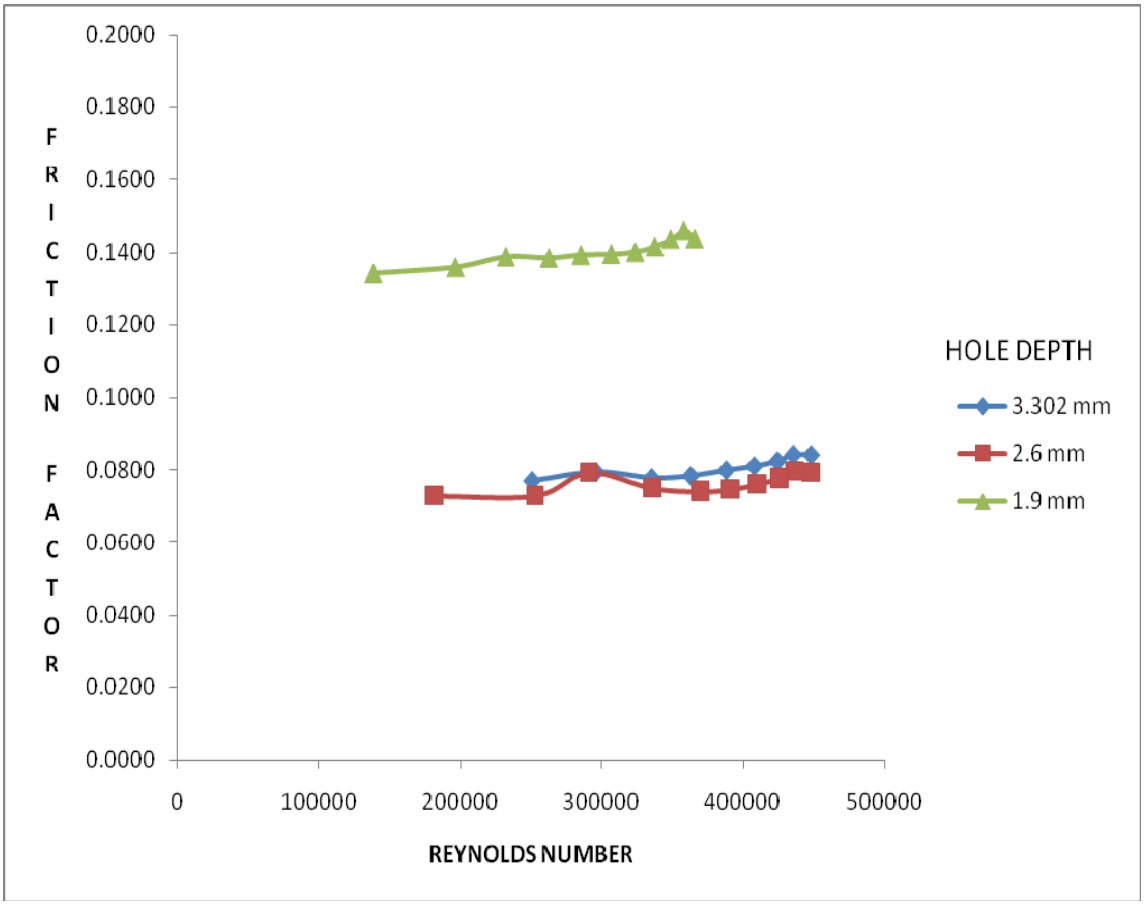

Figure 69. Effect of hole depth for smooth-on-hole configuration (P_{in}~55 bar, Ø=3.175 mm, C_p=0.635 mm).

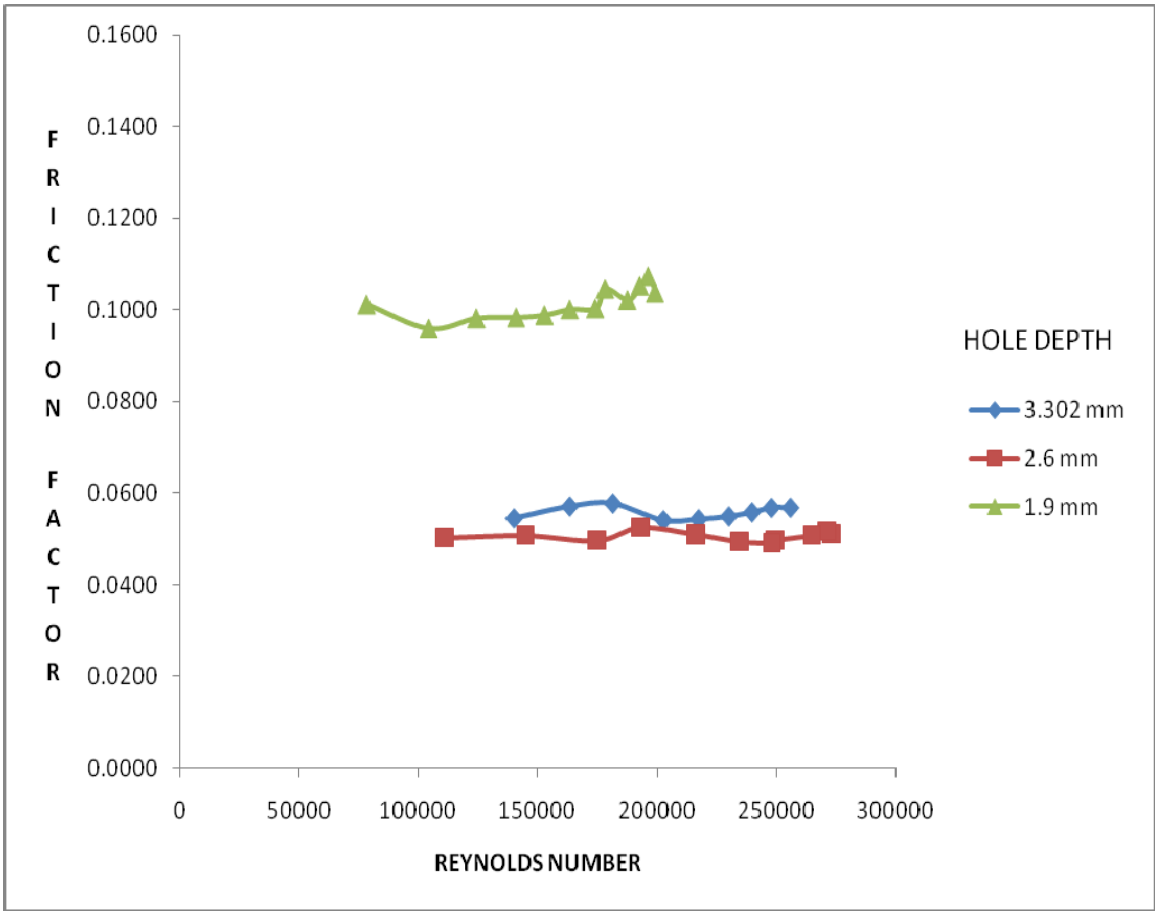

Figure 70. Effect of hole depth for smooth-on-hole configuration (P_{in}~55 bar, Ø=3.175 mm, C_p=0.381 mm).

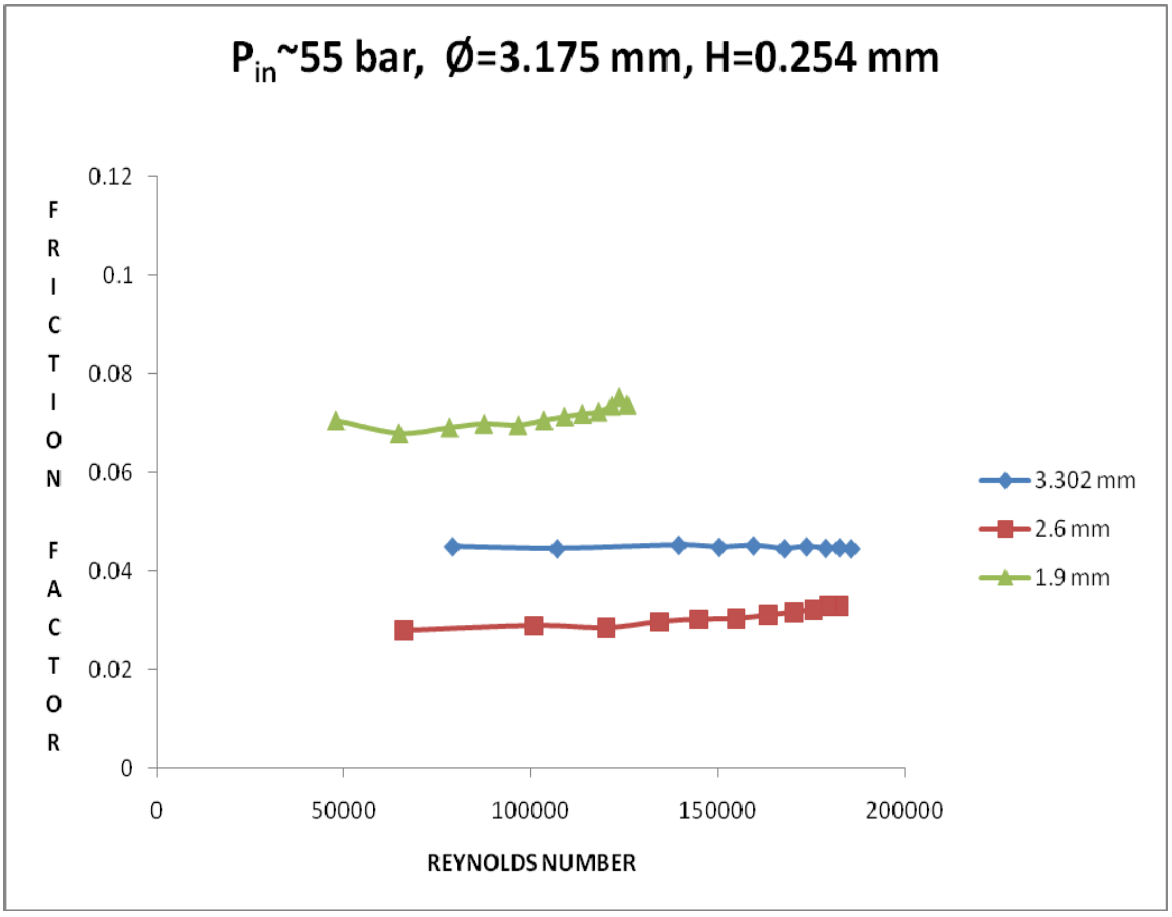

Figure 71. Effect of hole depth for smooth-on-hole configuration (P_{in}~55 bar, Ø=3.175 mm, C_p=0.254 mm).

VITA

Bassem Ali Kheireddin was born in Rayak, Lebanon. He is the eldest of two brothers and one sister. Bassem attended the University of Texas-Pan American and graduated in 2005 with high honors. He holds a B.S. degree in mechanical engineering and mathematics. After graduation, he was recruited by Texas A&M University to pursue his graduate studies and received his M.S. degree in mechanical engineering in 2009.